Superconductivity Program for Electric Systems
Annual Progress Report for Fiscal Year 2004

Superconductivity Technology Center

Los Alamos National Laboratory

Dean E. Peterson, Center Director and Program Manager
Jeffrey O. Willis, Principal Team Leader and Editor

Contributors:

P.N. Arendt	P. Hou[SP]	J. Reeves[SP]
S.P. Ashworth	T.A. Jankowski	C. Rey[DP]
J.G. Bernard[DP]	M. Jaime	V. Selvamanickam[SP]
R.N. Bhattacharya[NREL]	Q.X. Jia	A. Serquis
L. Civale	M. Johnson[NMSU]	C.J. Sheehan
J.Y. Coulter	J.A. Kennison	X. Song[UW]
D.K. Christen[ORNL]	S. Kreiskott	P. Spagnol[NREL]
G. Croes	D.C. Larbalestier[UW]	L. Stan
R.F. DePaula	Y. Li	J.A. Stewart
P.C. Dowden	Y. Lin	J. Storer
R. Feenstra[ORNL]	J.MacManus-Driscoll[UC]	J. Sullard
D.M. Feldmann[UW]	B. Maiorov	I. Usov
A.T. Findikoglu	M.P. Maley	H. Wang
S.R. Foltyn	V. Matias	J.A. Waynert
J. Gallegos	F.M. Mueller	J.O. Willis
B.J. Gibbons	D.E. Peterson	R.M. Wingo
J.R. Groves	F.C. Prenger	L.A. Worl
A. Gurevich[UW]	Y. Qiao[SP]	T.Y. Ying
T.G. Holesinger	A. Razani[UNM]	X. Xiong[SP]

Key to non-LANL Affiliations
DP = DuPont
ORNL = Oak Ridge National Laboratory
NMSU = New Mexico State University

NREL = National Renewable Energy Laboratory
SP = SuperPower
UNM = University of New Mexico
UW = University of Wisconsin-Madison

Los Alamos
NATIONAL LABORATORY
— EST.1943 —

Table of Contents

Table of Figures

Glossary of Acronyms

ANL	Argonne National Laboratory
AMSC	American Superconductor Corporation
BEI	Backscatter Electron Imaging
Bi-2212	$Bi_2Sr_2CaCu_2O_8$
Bi-2223	$(Bi,Pb)_2Sr_2Ca_2Cu_3O_8$
BSCCO	Bi-2212 or Bi-2223
CRADA	Cooperative Research and Development Agreement
EBSD	Electron Back-Scattered Diffraction
EDS	Energy Dispersive Spectroscopy
FCC	Fault Current Controller
FCL	Fault Current Limiter
HGMS	High-Gradient Magnetic Separator
HTS	High-Temperature Superconductivity
IBAD	Ion Beam-Assisted Deposition
IMP	Isothermal Melt Processing
I_c	Critical current of a superconductor, A
J_c	Critical current density of a superconductor, A/cm^2
LANL	Los Alamos National Laboratory
LARP	Los Alamos Research Park
MgO	Magnesium Oxide
MRI	Magnetic Resonance Imaging
NHMFL	National High-Magnetic Field Laboratory
ORNL	Oak Ridge National Laboratory
OSTI	Oxford Superconductivity Technology, Inc.
PLD	Pulsed-Laser Deposition
RBS	Rutherford Backscattering Spectroscopy
RHEED	Reflection High-Energy Electron Diffraction
SAD	Selected Area Diffraction
SEM	Scanning Electron Microscopy
Sm-123	$SmBa_2Cu_3O_{7-\delta}$
SPI	Superconductivity Partnerships with Industry
STC	Superconductivity Technology Center (Los Alamos)
T_c	Critical temperature for superconductivity, K
TEM	Transmission Electron Microscopy
TOFISARS	Time of Flight Ion Scattering and Recoil Spectroscopy
XRD	X-Ray Diffraction
YBCO	$YBa_2Cu_3O_{7-\delta}$
YSZ	Yttria-Stabilized Zirconia

Introduction

The rate of progress towards practical applications of high temperature superconductors (HTS) continues to be very rapid. BSCCO tapes are now commercially available for use in the Superconductivity Partnership Initiative (SPI) projects and other prototype power demonstrations. Second-generation coated conductors continue to display very high critical currents in long lengths when cooled with liquid nitrogen indicative of the future potential for wide spread use in power applications. The SPI projects including the three transmission cable initiatives, fault current limiter, generator, flywheel, motor, MRI, magnetic separator, and transformer are all exciting. The national laboratories are proud to have played important roles in advancing these technical successes.

LANL continued to be a CRADA partner with American Superconductor in the Wire Development Group focused on advancing further improvement of properties of BSCCO tapes. All current SPI projects rely on production of Bi2223 tapes with superconducting properties appropriate for the application. Our contributions in tape processing combined with both microscopic and superconducting characterizations have been critical to continued technical advancements in this area.

LANL continued to demonstrate leadership in coated conductor development by achieving world records for the highest critical currents achieved at liquid nitrogen temperature. New, unique tape processing and characterization capabilities have been developed at the Research Park that are now available to other national labs, universities, and industrial collaborators.

LANL continued strong partnerships with Superpower and American Superconductor in second-generation wire development focusing on the IBAD MgO technology. These collaborations have been extremely beneficial in accelerating their progress towards commercialization of coated conductors. Our expertise in evaluating vortex pinning in superconductor tapes as a function of magnetic field and angle was shown to be very valuable. LANL contributions towards characterizing and minimizing ac losses in coated conductors have been substantial.

LANL continued in a strong partnership with General Electric focused on a 100 MVA HTS SPI generator. Another SPI partnership with DuPont involving a HTS magnetic separator demonstrated efficient separation and scale-up potential. A SPI collaboration with Oxford directed towards a HTS MRI system demonstrated substantial technical progress.

Research and development activities at LANL related to the HTS program for FY04 are collected in this report. Technical highlights are listed in Section 1 and individual project summaries appear in Section 2. Section 3 lists the 30 journal articles and the 30 other publications and conference abstracts for the year. Section 4 summarizes the total patent and license activity, and Section 5 lists the various agreements completed or underway.

Dean E. Peterson, Leader
Superconductivity Technology Center

1. Highlights of Fiscal Year 2004

• *Reasons for alumina's effectiveness as a cation diffusion barrier layer beneath the IBAD-MgO template layer were found to be its high density and amorphous/nanocrystalline structure. Techniques to quantitatively determine the impurity concentrations in YBCO films and measure the effect of substrate element diffusion were established.*

• *Damage anisotropy experiments confirm the IBAD MgO texturing mechanism. We determined that the damage induced by Ar ion irradiation of MgO exhibited an anisotropy that conformed to $\chi_{max}^{(110)} < \chi_{max}^{(100)} < \chi_{max}^{(111)}$, where χ is the ratio of Rutherford backscatter yield for a particular orientation to that for a randomly oriented film.*

• *IBAD MgO deposition at lower temperatures revealed that the processing window for achieving an in-plane FWHM $\Delta\phi \leq 8°$ expanded by 40% when going to 25°C from 100°C.*

• *Examination of the thickness dependence of the J_c for YBCO suggested that extra interfaces inside the YBCO would be beneficial.*

• *Using CeO_2/YBCO multilayer films, previous best result (self field, 75 K) of 720 A/cm @ 4.5 µm for a single layer film was improved to 660 A/cm @ 1.65 µm and 1000-1400 A/cm for 3.1 to 3.6 µm films.*

• *We have expanded our analysis of vortex pinning in YBCO coated conductors, using J_c vs. angle data at various magnetic field strengths, adding the temperature variable. The previous selection of the value 5 for the anisotropy parameter γ based on the electronic mass anisotropy was determined experimentally from irreversibility line measurements to have this same value.*

• *Measurements and analysis of $J_c(H,\Theta,T)$ has led to the generation of a phase diagram of the various pinning regimes (ab plane and c-axis correlated pinning and random uncorrelated pinning) in Θ and T with H as a parameter.*

• *Measurements of Jc to very high magnetic fields has demonstrated that J_c can be scaled with the irreversibility field H_{irr}, and that J_c has an H^α field dependence at low fields rolling off to 0 above a critical field H_{cr}.*

• *We have successfully employed various scalable techniques to increase pinning in YBCO coating conductors. These include changing the RE ion size variance (random point defects), changing the average RE ion size (random point and correlated defects), introduce buffer layer surface roughness (low angle grain boundaries || c), and introducing heteroepitaxial second phases ($BaZrO_3$) (increases c-axis dislocation density). The last two were particularly effective in improving the in-field pinning as determined by a decrease in α.*

• *Differences in pinning between PLD and MOD YBCO films were found to correlate with their different microstructures.*

• *RE123 film growth rate by PLD is found to correlate with the RE ion size.*

• *A study of ex situ BaF_2 YBCO films shows that typical films have a bimodal microstructure, meandering grain boundaries, and second phase layers*

that cause misalignments and reduce J_c. A "fast-modified" process results in uniform through thickness properties and higher J_c.

- *Tapes of 100 m length, 3 cm wide tapes, and RABiTS tapes have been successfully polished in the electropolishing system.*
- *MgO IBAD template layer deposition speed has been raised to 100 m/h, and parameters to achieve optimal texture have been investigated.*
- *A new 9-zone lamp heater has been installed in the reel to reel PLD chamber and temperature profiles and control have been improved resulting in greater uniformity in J_c along the length of a 1 m conductor.*
- *A new system has been developed to measure (magnetic) ac losses as a function of position along a coated conductor.*
- *LANL has provided GE with required data on outgassing and gettering of materials required for long-term vacuum maintenance of the 100 MVA HTS generator. LANL has also supplied a heat pipe concept for cooling the HTS rotor.*
- *High gradient magnetic separation has proven effective in laboratory scale experiments for cleaning heavy metals from mine drainage. Capacity, reaction time, and other important parameters to designing a pilot system have been determined.*
- *Bi-2212 conductors for a HTS MRI system magnet have been characterized microstructurally and electrically under design conditions. MgO doping to the Bi-2212 has been found to increase the in-field pinning and J_c.*
- *Thirty-two journal articles were published, nearly 30 journal articles were submitted for publication, and more than 30 conference abstracts were submitted during the year.*
- *Eight patent disclosures or filings were made and three patents were issued during the year.*
- *Two CRADA agreements were renewed, and two funds-in agreements were executed during the year.*

2. Technical Activities

2.1 Wire Technology

<u>2.1.1 MgO template development for coated conductors using ion beam assisted deposition</u>

P.N. Arendt, S.R. Foltyn, R. DePaula, T.G. Holesinger, Q.X. Jia, S. Kreiskott, V. Matias, L. Stan, I. Usov, and H. Wang, SuperPower: V. Selvamanickam, P. Hou, Y. Qiao, J. Reeves, X. Xiong

In 2003, a 70 nm thick "buffer" architecture of $SrRuO_3$/IBAD MgO/Y_2O_3 was found to be incapable of inhibiting diffusion of substrate elements into the final YBCO film (Fig. 1a). Diffusion of substrate elements is thought to be mitigated for IBAD YSZ with its thicker template/buffer architecture and for RABiTs with its thicker multilayer buffer stack. For IBAD MgO a comparable solution would be to employ thicker epitaxial layers between the template and the YBCO. Another (more cost effective) solution could employ a barrier layer film below the IBAD MgO deposited near room temperature. Recently, we have found that Al_2O_3 films are capable of inhibiting diffusion of substrate elements (Fig. 1b).
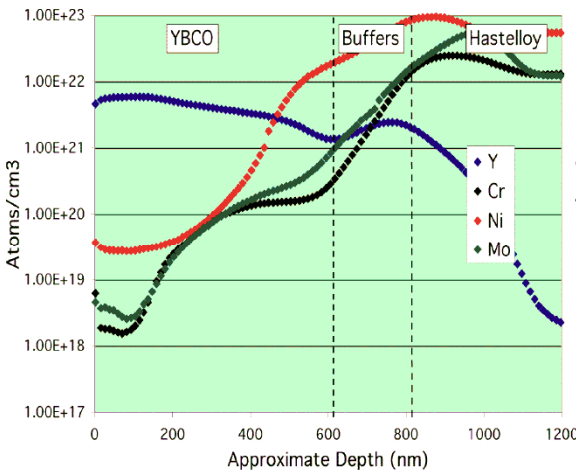
Fig. 1. Secondary Ion Mass Spectroscopy (SIMS) revealed intermixing of the substrate and YBCO occurs (0.5mm YBCO/50nm SRO/12 nm MgO/7nm Y_2O_3/Hastelloy C-276).
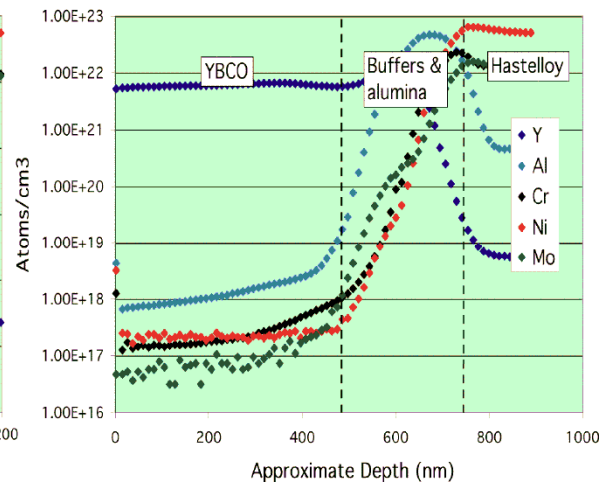
Fig. 1b. Inserting an 80 nm thick Al_2O_3 film at the base of the buffer stack inhibited the intermixing. (0.5mm YBCO/50nm SRO/12nm MgO/7nm Y_2O_3/ 80nm Al_2O_3/Hastelloy C-276)

A more detailed study was initiated to determine why this barrier worked by I. Usov et al., J. Mater. Res. 19, 1175 (2004) Al_2O_3 films deposited on Hastelloy C-276 were annealed at fixed temperatures from 500 to 1000°C. Concentration profiles of the C-276 elements (C, Si, Mn, Co, W, Fe, Cr, Mo, and Ni) were then obtained in the Al_2O_3 using SIMS. Of the C-276 elements, only Mn, Ni and Cr were observed to diffuse into the alumina.
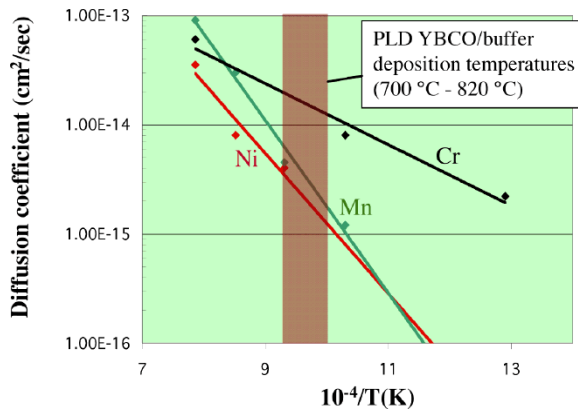
Fig. 2. Arrhenius plot of diffusion of substrate elements through the barrier layer.

Based on the Arrhenius plot (Fig. 2), after 10 min @ 850°C, 6 x 10^{15} Cr atoms/cm^2 will be on the surface of a 50 nm thick Al_2O_3 film ($\simeq$ 8 ppm Cr in a 1 μm thick YBCO film). Some considerations must be taken into account to use of the diffusion coefficient data. Diffusion is a function of the source (element concentrations at the substrate film interface), film microstructure, temperature, etc. Fig. 3a shows the typical stacking sequence for a SuperPower substrate with LANL buffers and YBCO. Fig. 3b shows that Cr is blocked by the Al_2O_3 film. For a stainless steel substrate, Fe may also play a role as one of the diffusing elements.
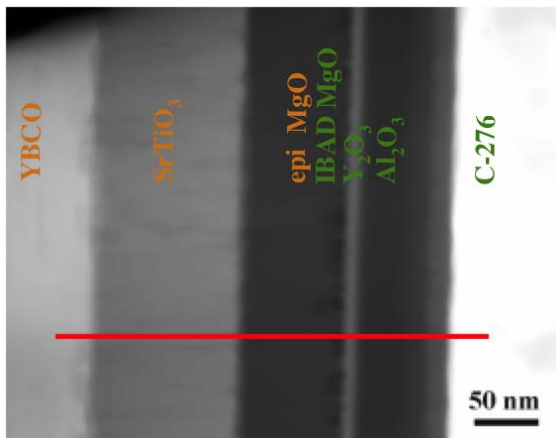
Fig. 3a. Dark field TEM cross section of SuperPower template (green) and LANL YBCO/buffers (orange).
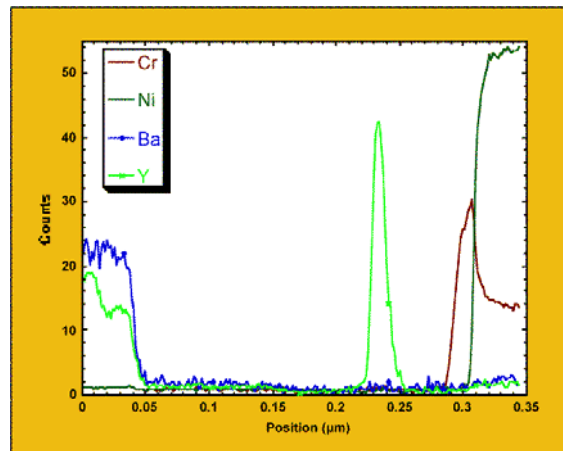
Fig. 3b. EDS line scan (Fig. 3a) of Y, Ba, Cr, and Ni. Cr is concentrated at the substrate/Al_2O_3 interface.

An advantage of this microstructure (Fig. 4) is that the surface of the film is very smooth (< 1 nm rms). Rutherford backscattering/Dektak analyses show the films are 83% as dense as SXAL Al_2O_3. The diffusion coefficients in a polycrystalline film are expected to be higher than in a single crystal film.
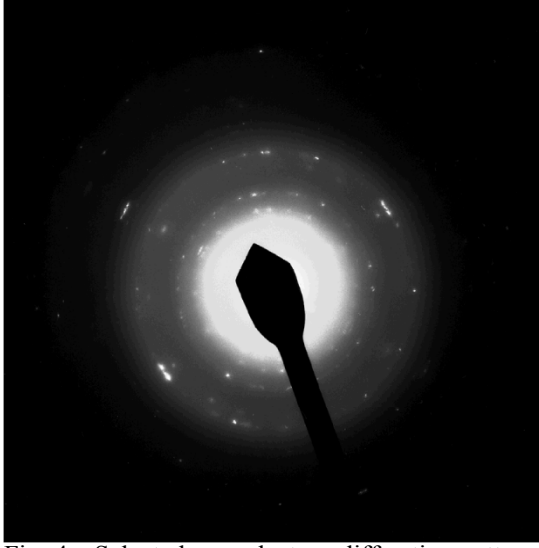
Fig. 4a. Selected area electron diffraction pattern of Al_2O_3 film indicates it is amorphous and nanocrystalline.
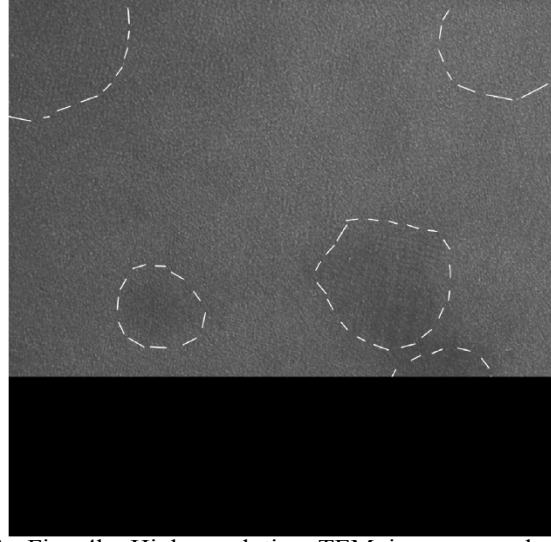
Fig. 4b. High resolution TEM image reveals the nanocrystallites are surrounded by amorphous material.

Most impurities degrade superconductivity in YBCO, thus quantitative tolerance of YBCO for some of the diffusing transition metals has been investigated. 200 nm PLD YBCO films were deposited on SXTAL $SrTiO_3$ substrates. The depositions were performed with and without a Ni foil strip mounted on the YBCO target. T_c and J_c measurements were performed, and the Ni concentration was measured using Particle Induced X-ray Emission (PIXE); see Fig. 5.
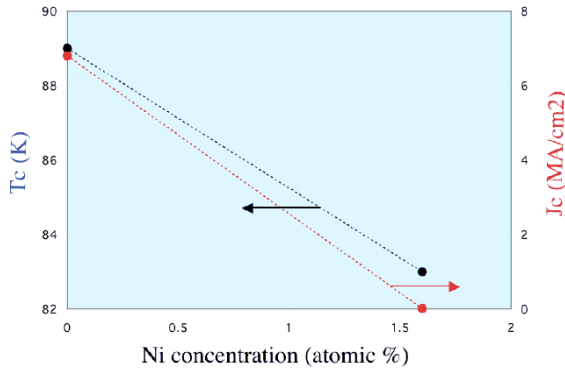
Fig. 5. Superconducting critical temperature T_c and critical current density J_c as a function of Ni concentration in a YBCO film.

In our next task, the damage anisotropy of Ar^+ irradiated MgO was investigated to elucidate an IBAD texturing mechanism. (For reference, Fig. 6a shows RBS of random and aligned (110) MgO.) MgO single crystals of (100), (110) and (111) orientations were irradiated with 100 keV Ar^+ ions at varying doses and implantation temperatures. Rutherford backscattering spectrometry (RBS) (Fig. 6b) combined with ion channeling was then used to quantify radiation damage as a function of crystallographic orientation, ion dose, and temperature. The damage was estimated using $\chi_{max}^{(110)}$ (%) = Y_{IA}/Y_R, where Y_R is the random yield, and Y_{IA} is the yield (see Fig. 6a) for the aligned case.

Samples were irradiated at 25°C and at an Ar^+ dose of $1 \times 10^{15}/cm^2$. The measured damage exhibited by the different crystallographic orientations generally conformed to: $\chi_{max}^{(110)} < \chi_{max}^{(100)} < \chi_{max}^{(111)}$, as seen in Fig. 6b.
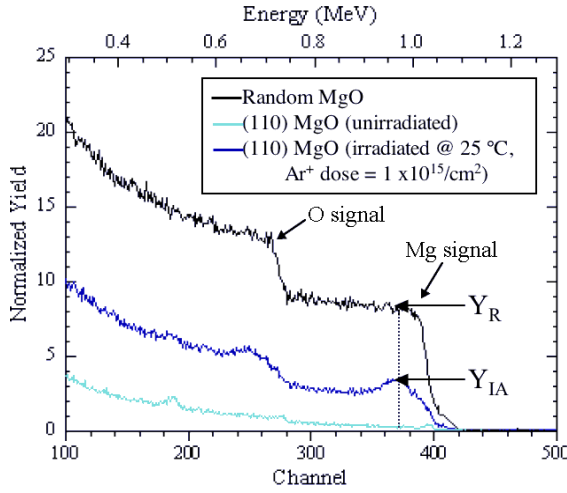
Fig. 6a. RBS spectra of random and aligned (110) MgO samples.
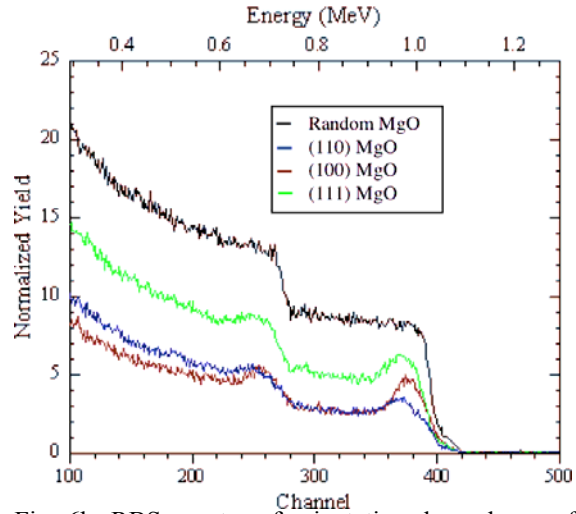
Fig. 6b. RBS spectra of orientation dependence of the normalized yield for crystalline MgO.

The difference in damage accumulation was relatively constant (Fig. 7a) above an Ar^+ dose of about $1 \times 10^{15}/cm^2$. Thus in the dose range used by most institutions, this is the case. It was also found (Fig. 7b) that the size of the anisotropy in the damage accumulation was largest at temperatures below ~200 K.
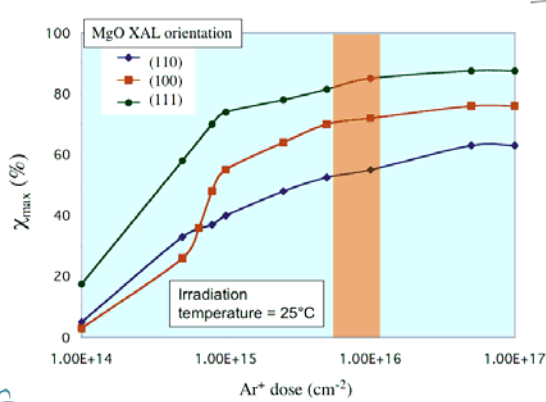
Fig. 7a. Orientation dependence of Ar^+ damage accumulation in crystalline MgO for dose ranges used by various institutions (brown band).
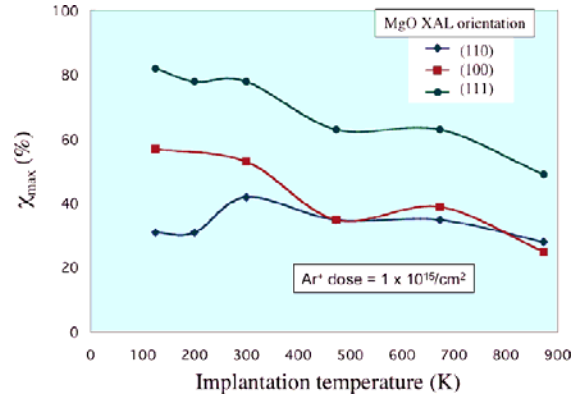
Fig. 7b. Temperature dependence of the damage accumulation in crystalline MgO.

We have also determined that the IBAD MgO processing window is expanded at lower film growth temperatures. Stationary substrates were held at fixed temperatures by silver pasting the substrate to a copper block during deposition. Many IBAD samples (Fig. 8a) were made at three temperatures (100°C, 25°C and -150°C) and at differing ion assist currents. The result was that the processing window for obtaining an in-plane FWHM $\Delta\phi \leq 8°$ expanded by 40% when going to 25°C from 100°C.

This means that care must be taken during IBAD deposition to insure good thermal contact with a heat sink to prevent the sample temperature from rising. Fig. 8b shows that a poorly heat-sinked 50 μm thick Hastelloy C-276 substrate can heat up much more than one well heat sinked. For these samples, well-textured MgO is achieved in 100 s of deposition. The substrate temperature can be further reduced by pulsing the ion assist gun to allow for some cooling during the deposition.

20
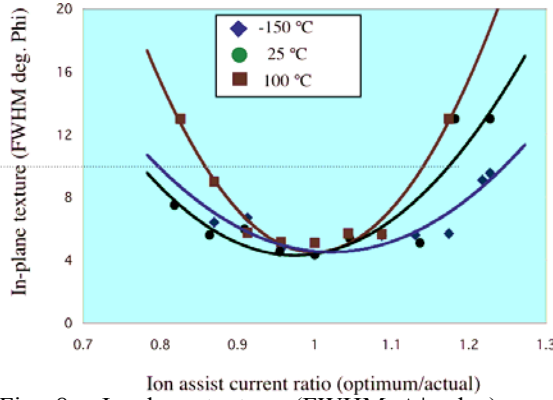
Fig. 8a. In-plane texture (FWHM $\Delta\phi$, deg) as a function of ion assist current ratio for several deposition temperatures.
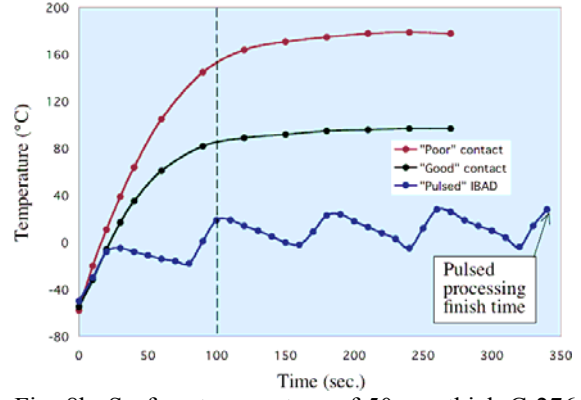
Fig. 8b. Surface temperature of 50 μm thick C-276 tape heated by ion-assist gun conditions resulting in well textured IBAD MgO film in 100 sec.

Up until the present (Fig. 9), all template layers had been made at temperatures >100°C. Therefore, we expect to be able to improve the texture and performance further by processing at lower temperatures.
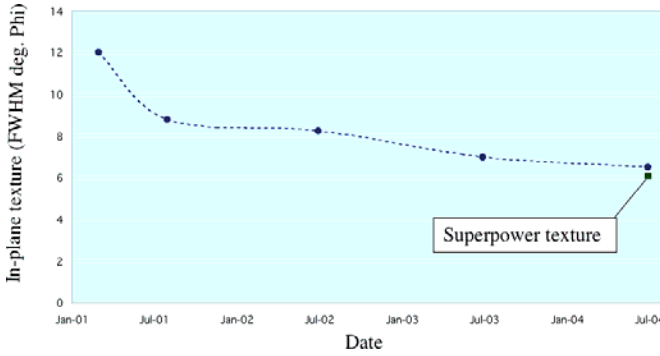
Fig. 9. Recent progress on in-plane texture of IBAD MgO templates.

Summarizing our progress on IBAD MgO templates, our damage anisotropy experiments provided the first confirmation of IBAD MgO texturing mechanism. We determined that the damage induced by Ar ion irradiation of MgO exhibited an anisotropy that conformed to $\chi_{max}^{(110)} < \chi_{max}^{(100)} < \chi_{max}^{(111)}$.

We also established a methodology to quantitatively determine impurity concentrations in YBCO films and measure the effect of substrate elements on superconducting properties. To do this, we measured the diffusion coefficients of transition metal elements in alumina films, as used in our IBAD MgO architecture.

The temperature dependent damage accumulation data we collected implied that IBAD texturing would improve at low temperatures. Although we subsequently determined that the optimum texturing was unchanged at low temperatures, the processing window was expanded.

2.1.2 High current coated conductors based on IBAD MgO and PLD YBCO

S. R. Foltyn, P.N. Arendt, H. Wang, Q.X. Jia, R. DePaula, L. Stan, L. Civale, B. Maiorov, Y. Li, and P. Dowden

One of our major goals for 2004 was to identify and attempt to overcome limitations to achieving high critical current densities in thick film J_c. Our approach has been to consider the drop in J_c with thickness as though it were a materials-processing issue, and not intrinsic. Then, at a particular thickness, the approach is to maximize J_c through a comprehensive process optimization. The ultimate goal then is the reproducible achievement of I_cs over 400 A/cm-width at a film thickness of ≤ 1.5 μm.

This goal was met by optimizing the buffer layer deposition process. We also developed a simple model for the dependence of J_c on thickness, and tested one prediction of model, significantly increasing I_c beyond our target goal.

The process optimization focused on the laser-deposited $SrTiO_3$ buffer layer used for the ion beam assisted deposited (IBAD) MgO template layer. We changed the buffer from the $SrRuO_3$ used previously to $SrTiO_3$. The first step was to use the "standard" deposition condition to determine the effect of buffer layer thickness on J_c (similar to the earlier work on the effect of buffer layer thickness of CeO_2 on IBAD YSZ).

The result (Fig. 10) was that at 20 nm, the texture is OK; however, the J_c is low, possibly because of diffusion of substrate elements. At 360 nm, the $SrTiO_3$ is quite rough, resulting in poor YBCO texture. The optimum $SrTiO_3$ thickness is in the range of 40 to 120 nm. However, even for small $SrTiO_3$ thicknesses (Fig. 11), ion milling revealed no diffusion problems, even for very thin $SrTiO_3$ (20 nm in this case).
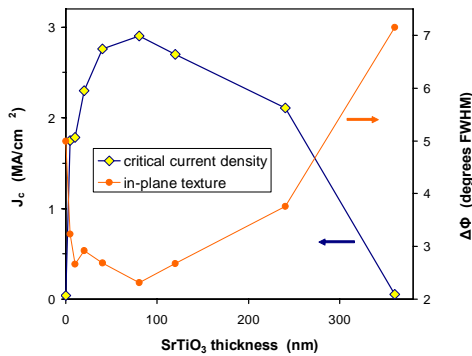
Fig. 10. Critical current density J_c (75 K, sf) and in-plane texture $\Delta\phi$ for 1.7 μm thick YBCO films on IBAD MgO.
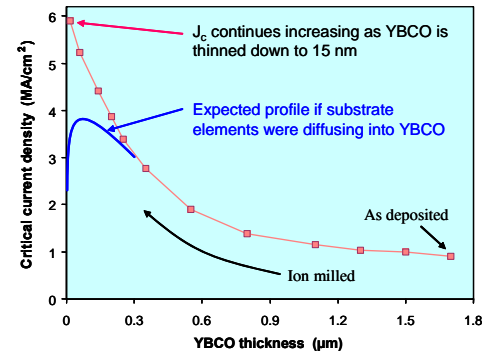
Fig. 11. Critical current density J_c (75 K, sf) for an ion milled YBCO films on IBAD MgO.

We have also found that the optimum $SrTiO_3$ deposition temperature can vary for different IBAD MgO runs (Fig. 12), even though the peak J_c values are similar. In a study of $SrTiO_3$ deposition on early IBAD MgO, the optimum temperature was near 820°C, whereas in a more recent study, the optimum temperature was determined to be ~700°C. The YBCO texture is 2.4 − 3.6° FWHM in-plane and is unaffected by the $SrTiO_3$ deposition temperature. The YBCO deposition temperature was 760°C for all samples.
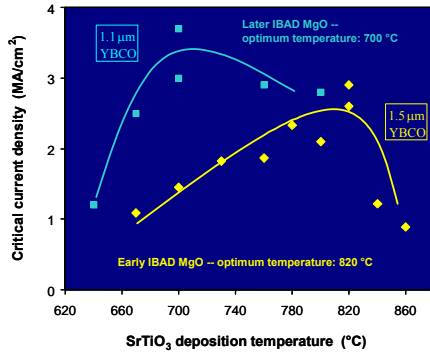
Fig. 12. Critical current density as a function of SrTiO$_3$ deposition temperature for two series of MgO IBAD.

TEM analysis revealed thickness differences in the oxide layer stack but not why the optimum SrTiO$_3$ temperature is different. Fig. 13 shows cross sectional TEM images of the different layers optimized for the two sets of IBAD samples. There structures in both cases are very similar.
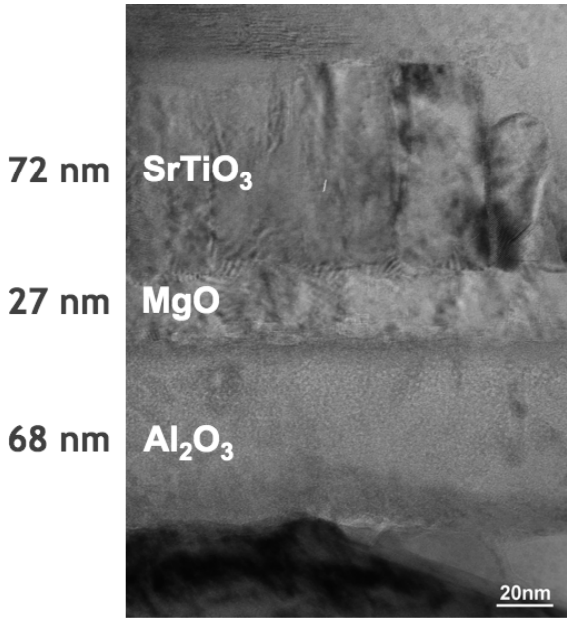
Fig. 13a. Cross sectional TEM image of coated conductor buffers on early IBAD with an optimum SrTiO$_3$ deposition temperature of 820°C.
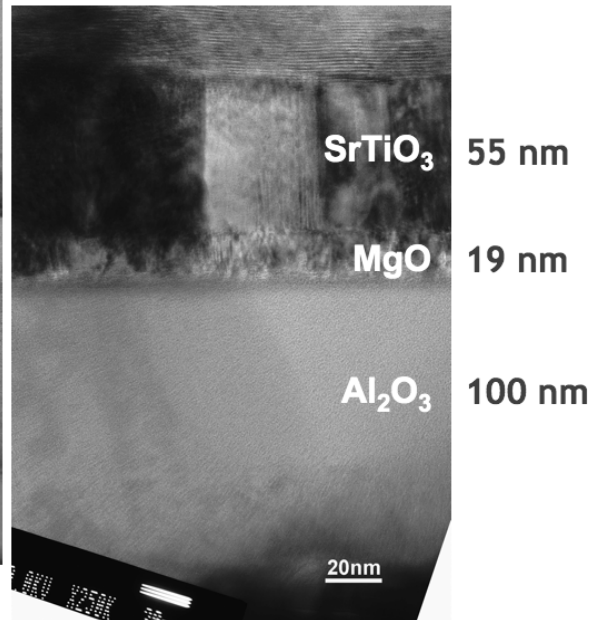
Fig. 13b. Cross sectional TEM image of coated conductor buffers on later IBAD with an optimum SrTiO$_3$ deposition temperature of 700°C.

In all cases, however, the highest J$_c$ results from the SrTiO$_3$ deposition temperature that yields the smoothest surface. SEM images (Fig. 14), H. Wang, et al., J. Mater. Res. 19, 1869 (2004), show fewer SrTiO$_3$ outgrowths on the buffer layer surface at the optimum deposition temperature.
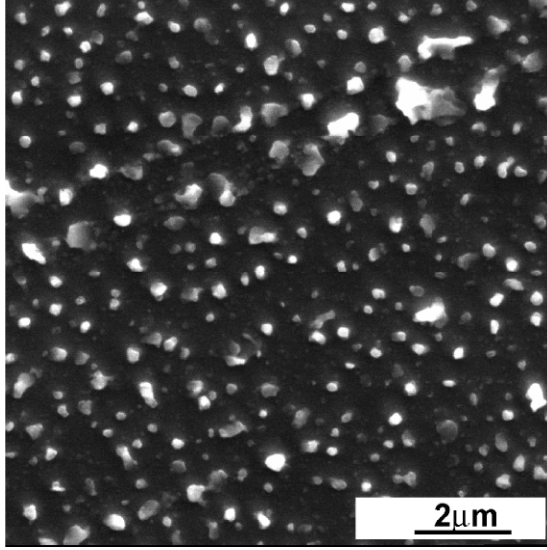
Fig. 14a. SEM image of a rough SrTiO$_3$ surface. T$_{dep}$ = 670°C and J$_c$ = 1.1 MA/cm^2.
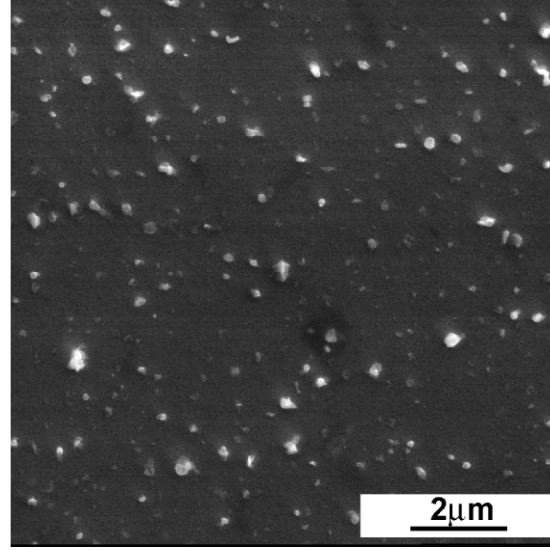
Fig. 14b. SEM image of smooth SrTiO$_3$ surface. T$_{dep}$ = 820°C and J$_c$ = 3.0 MA/cm^2.

Optimization of the SrTiO$_3$ buffer layer through this procedure has allowed us to reach the goal of 400 A/cm-width @ 1.5 μm on an IBAD MgO template layer (Fig. 15a). However, to reach still higher current levels, a different approach is needed. Fig. 15b indicates the three possible paths to achieving higher critical currents. It is not likely that J$_c$ can be increased significantly above current levels, which are near 10% of the depairing limit, the maximum physically possible J$_c$ value. This is comparable to the ratio achievable for high performance Ni-Ti and Nb$_3$Sn superconductors. It is not practical to just increase the thickness of YBCO films: mechanical problems, such as delamination become more and more important as the thickness increases, and thicker films mean more material and longer times to fabricate, which is not economically practical. Thus, the best option is to try to increase both the J$_c$ and the thickness simultaneously, as indicated in Fig. 7.
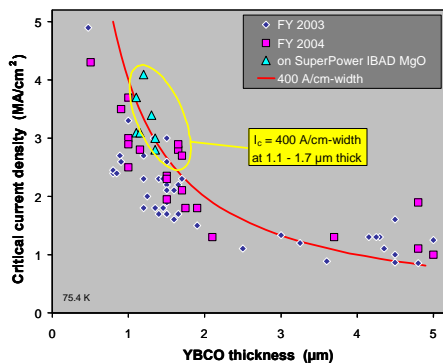
Fig. 15a. Critical current density of YBCO films as a function of film thickness.
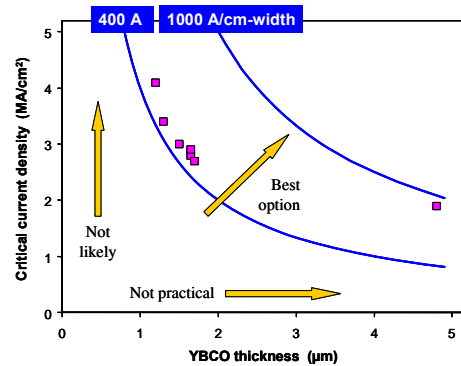
Fig. 15b. Paths to achieve 1000 A/cm-width performance levels.

Our effort to reach higher currents started with consideration of the *incremental* critical current density. The incremental critical current density j$_c$ is the critical current density for a slice of YBCO that has been hypothetically isolated from the rest of the coating (Fig. 16) and measured. For PLD YBCO, the incremental j$_c$ is established during film

growth and is independent of the total film thickness. This can be seen in the results shown in Fig. 17, which illustrates that for samples as deposited and ion milled, the dependence of J_c on thickness is identical.
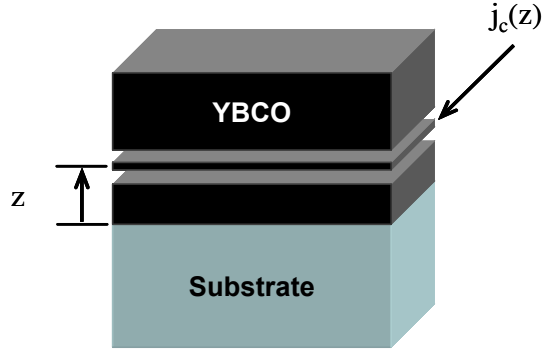
Fig. 16. Schematic of YBCO film to indicate the concept of the incremental critical current value j_c.
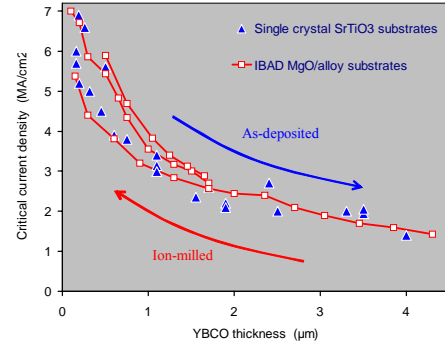
Fig. 17. Critical current density J_c of YBCO films as a function of film thickness for as deposited and ion milled samples.

Results for YBCO films on single crystal SrTiO$_3$ and on IBAD MgO are equivalent.

There are two characteristic j_c values for YBCO films that can be estimated from plots of $J_c(t)$, where t is thickness. The inset of Fig. 18a shows the typical dependence of J_c on film thickness for YBCO films. There are two limiting values of j_c that can be extracted from this dependence. For very thin films, the limiting values for J_c at the interface (j_{ci}) is about 7 MA/cm^2. For thick films, J_c tends toward an asymptote of about 1.5 MA/cm^2 for bulk YBCO (j_{cb}). The exact behavior of j_c in the intermediate region is unknown as indicated by the question marks in Fig. 18a. The simplest possible model for $j_c(z)$ is shown in Fig. 18b. The incremental j_c is highest at the interface where the superconductor and the substrate (or buffer layer) meet. This high j_c decreases linearly with distance from the interface over a certain range, from 0 to z_r. Beyond this range the interfacial influence ends and the critical current density assumes a constant value, j_{cb}. Using this very simple model, we have been able to achieve a good fit to the experimental J_c data, as shown in Fig. 18c.
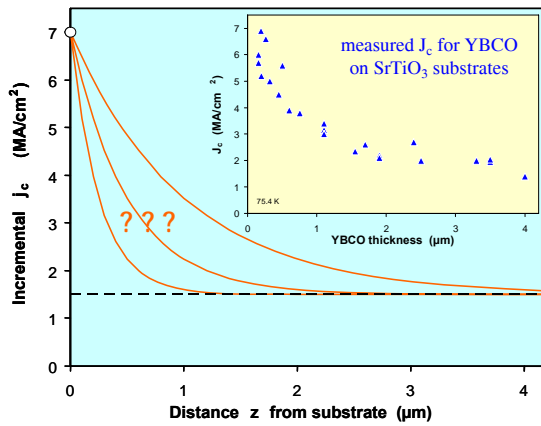
Fig. 18a. Limiting values of the incremental critical current density j_c for YBCO.
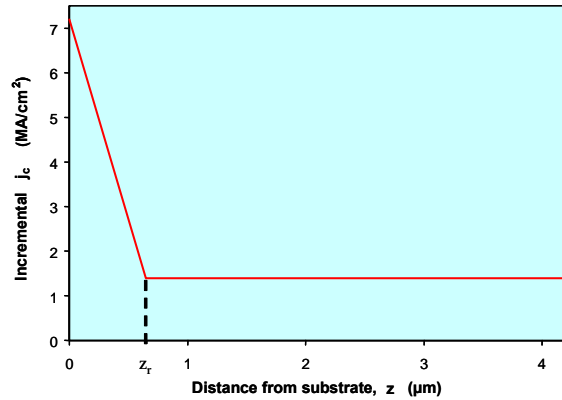
Fig. 18b. Simple model for $j_c(z)$ for a YBCO coated conductor

25
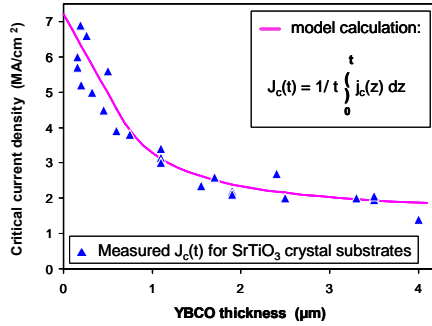
Fig. 18c. Fit of model calculation to experimental values of the critical current density as a function of thickness for YBCO.

A possible explanation for the inherent or "bulk" j_c for YBCO comes rom recent work by B. Dam *et al.*, (Phys. Rev. B 65, 064528 (2002)) in which a high density of dislocations between 2D growth islands in PLD films was observed. The dislocations are parallel to the c axis and extend from near the substrate to the film surface. The density of dislocations is also independent of YBCO thickness. This same work may provide a clue as to the source of high interfacial j_c

The process that produces threading dislocations also produces misfit dislocations, and these dislocations only populate the region near the interface. Although the misfit dislocations lie mainly in the YBCO a-b plane, they create a cross-hatch pattern that may be effective at pinning flux perpendicular to the plane. This was the conclusion of work at Los Alamos by H. Safar, *et al.*, Appl. Phys. Lett. **68**, 1853 (1996).

Misfit dislocations are a common feature in heteroepitaxial film growth, as seen in Fig. 19a, for example. From TEM cross-section images of our films (Fig. 19b), we find strong evidence for a high interfacial defect density. However, regardless of the source of high interfacial j_c the model predicts that extra interfaces will increase the average J_c of the YBCO film.
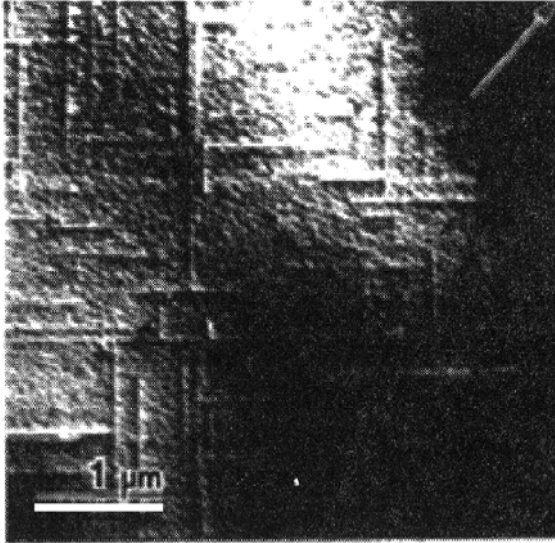
Fig. 19a. TEM plan view of misfit dislocation in a thin GeSi film on an (001) Si substrate. (J. Washburn, *et al.*, J. Electronic Mat. **20**, 155 (1991)
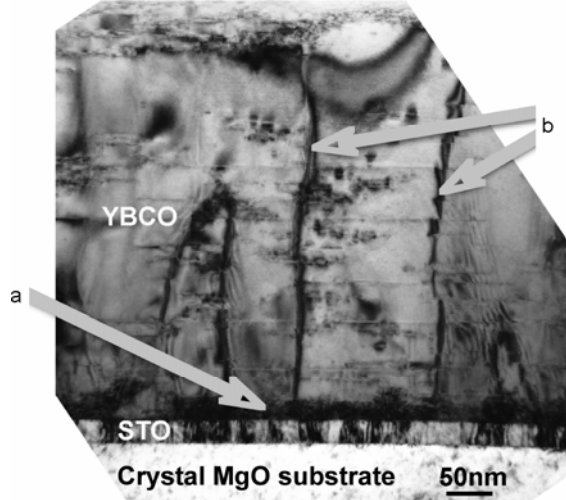
Fig. 19b. a) A 20 nm thick region at the YBCO-SrTiO$_3$ interface with a high density of defects; b) threading dislocations between columns.

To test this hypothesis, we can introduce extra heteroepitaxial interfaces using a YBCO (CeO$_2$/YBCO)n multilayer design, as illustrated in Fig. 20a. The present work differs from our earlier multilayer work in both design and purpose. The earlier work (Q.X. Jia, *et al.*, Appl. Phys. Lett 80, 1601 (2002)) used multilayers to solve a porosity problem in films more than 1.5 μm thick. In that work, CeO$_2$ interlayers were used initially, but were quickly replaced with layers of SmBCO. The porosity problem was ultimately solved by using smoother substrates. In the present work the CeO$_2$ interlayers are thinner than before, allowing for electrical contact between YBCO layers. In addition, each YBCO layer is thinner and therefore has a higher J$_c$. The purpose of the new multilayer film is to raise J$_c$ by imparting the high interfacial performance to a greater volume of the film, as can be seen in the model incremental j$_c$ plot in Fig. 20b. The multilayer philosophy is designed to create multiple regions of high interfacial J$_c$ throughout the coating.
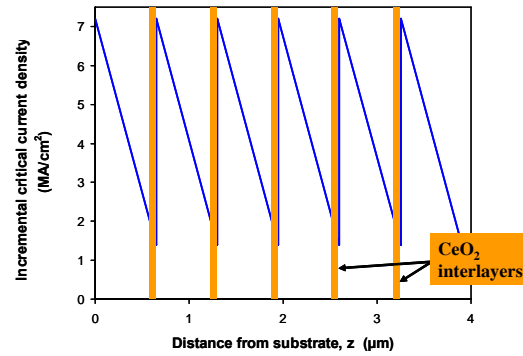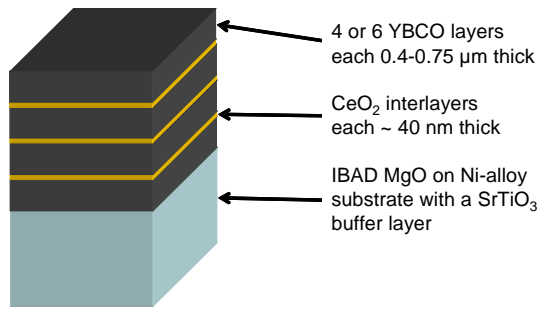
Fig. 20a. Schematic stacking sequence of films in (CeO$_2$/YBCO)n multilayer design.

Fig. 20b. Thickness dependence of the incremental j$_c$ for a multilayer sample.

The YBCO/CeO$_2$ multilayer approach significantly increases the thick-film J$_c$ and enables achievement of I$_c$ levels above 1000 A/cm-width. Comparing the expected with measured J$_c$ values, the J$_c$ for a 0.58 μm single layer is 4.6 MA/cm^2, and is very close to the measured value for a 3.5 μm multilayer (six 0.58 μm YBCO layers) of 4.0 MA/cm^2. As a result of this increase in the average J$_c$ value, very significant increases in I$_c$ have been achieved, as shown in Fig. 21.
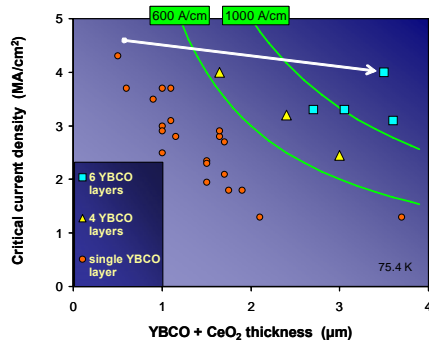
Fig. 21. Critical current density of YBCO/CeO$_2$ multilayer films as a function of total film thickness.

To summarize, we took a fresh look at the J$_c$ drop with YBCO thickness and concluded that extra interfaces inside the YBCO would be beneficial. We significantly improved upon the single layer film performance by using YBCO-CeO$_2$ multilayers. Previously,

the highest current in a 4.5 μm thick single layer YBCO film on IBAD MgO was 720 A/cm-width. Now, with the new multilayer technology, the highest achievable critical currents are 660 A/cm-width in a 1.65 μm film, and 1000-1400 A/cm-width for 3.1 to 3.6 μm thick films.

Our approach was to treat the drop in J_c with thickness as though it is a materials-processing issue, and not intrinsic. Thus at a particular thickness, the plan has been to maximize J_c through a comprehensive process optimization with a goal of reproducibly achieving I_cs over 400 A/cm-width at a film thickness of ≤ 1.5 μm. We continue to refine multilayers to exploit very high J_cs for thinner YBCO with the goals of producing reproducible 1000 A/cm-width tapes in 2.5 μm thicknesses and assisting industrial partners in implementing multilayer designs appropriate to their deposition technologies.
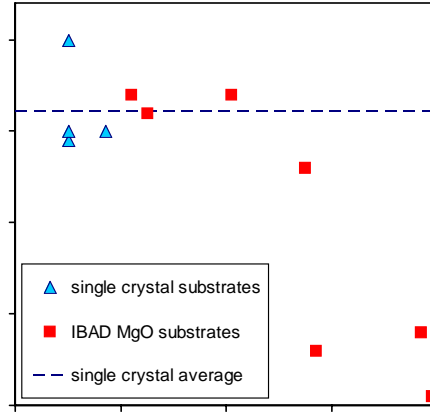
Fig. 22. n value of YBCO films on single crystal substrates and on IBAD MgO as a function of in plane texture.

We used extended I-V curves for IBAD MgO to evaluate the validity of the presence of a low angle plateau in performance, similar to that seen for YBCO on bicrystal substrates. The extended I-V curves proved to be less sensitive for IBAD than for bicrystals because of the large number of grain boundaries in the current path for the former. However, the n-value (as in $V = I^n$) is also a good indicator of the transition to weak-link behavior at 4-5° FWHM. The data in Fig. 22 imply that for an angle of less than 4-5°, a plateau has been reached. This means that achieving even better in plane orientation is unlikely to result in higher J_c values: presently obtainable texture is sufficiently good, thereby relaxing an important manufacturing constraint.

2.1.3 Understanding and Improving Pinning in Coated Conductors

L. Civale, J.L. MacManus-Driscoll (Also at Cambridge Univ., UK), B. Maiorov, H. Wang, A. Serquis (Present address: Centro Atomico Bariloche, Argentina), T.G. Holesinger, S.R. Foltyn, P.N. Arendt, Q.X. Jia, M. Jaime, P.C. Dowden, Y. Li, J.O. Willis, and J.Y. Coulter

We use the magnetic field, angular and temperature dependences of J_c to identify pinning mechanisms and regimes in YBCO coated conductors (CC). Previously we explored the behavior of PLD films on single crystal STO substrates and on IBAD MgO templates, at ~75 K. Now, due to improved texture, our PLD films on IBAD MgO already show J_cs equivalent to those on single crystal substrates, so J_c was determined by the bulk vortex pinning, and we could use transport measurements to explore it. In this work, we extend transport measurements and analysis of flux pinning to lower temperatures, study films thinner than 1 μm, explore the angular dependence of J_c in CC with different architectures, and grow and study HTS films with rare earth substitutions.

We begin the pinning analysis by determining the temperature, field and angular dependence of J_c (limited by vortex pinning) in PLD films at T=75 K. A typical set of critical current density data is shown in Fig. 23. We previously (L. Civale et al., Appl. Phys. Lett. 84, 2121 (2004).) developed a scaling method based on YBCO anisotropy to separate random and correlated pinning contributions to J_c. In this analysis we first transform the magnetic field $\tilde{H} = H\varepsilon(\Theta)$, where $\varepsilon(\Theta) = [\cos^2(\Theta)+\gamma^{-2}\sin^2(\Theta)]^{1/2}$, and the anisotropy parameter γ is 5 to 7 for YBCO, according to the anisotropic scaling model for random pinning defects first proposed by Blatter in 1992. If pinning is only due to random point defects, then $J_c(H, \Theta)$ depends on a single variable: $J_c=J_c[\tilde{H} = H\varepsilon(\Theta)]$.
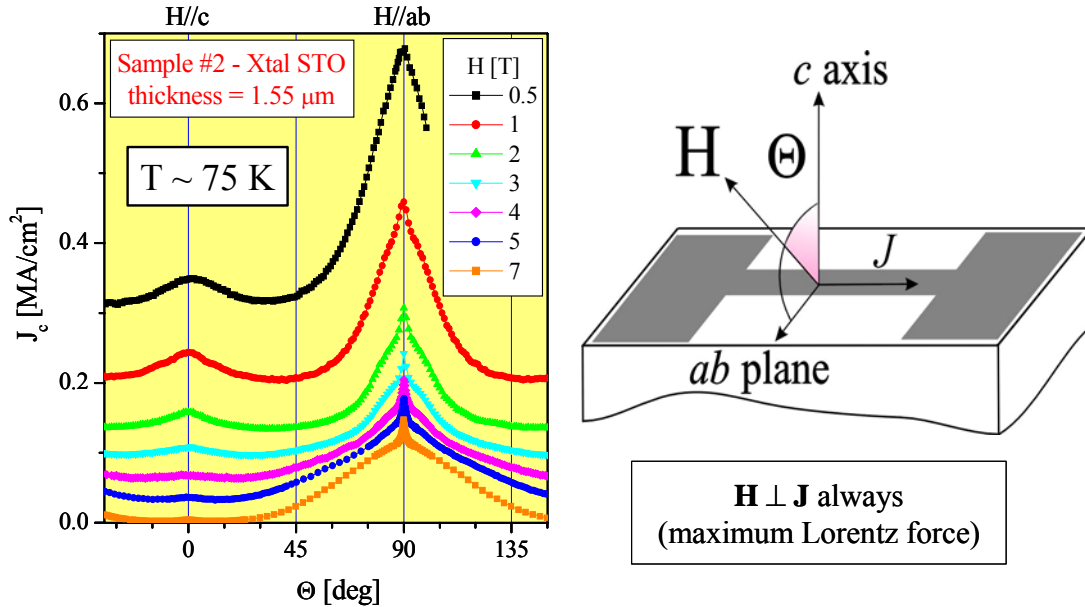
Fig. 23. Angular dependence of J_c with magnetic field as a parameter for YBCO at 75 K. The right hand side of the figure shows the definition of the angle Θ.

The angular dependence of J_c arises from a combination of factors and exhibits various regimes. Fig. 24 shows the transformation of the original data (Fig. 24a) into the scaled coordinate system (Fig. 24b).
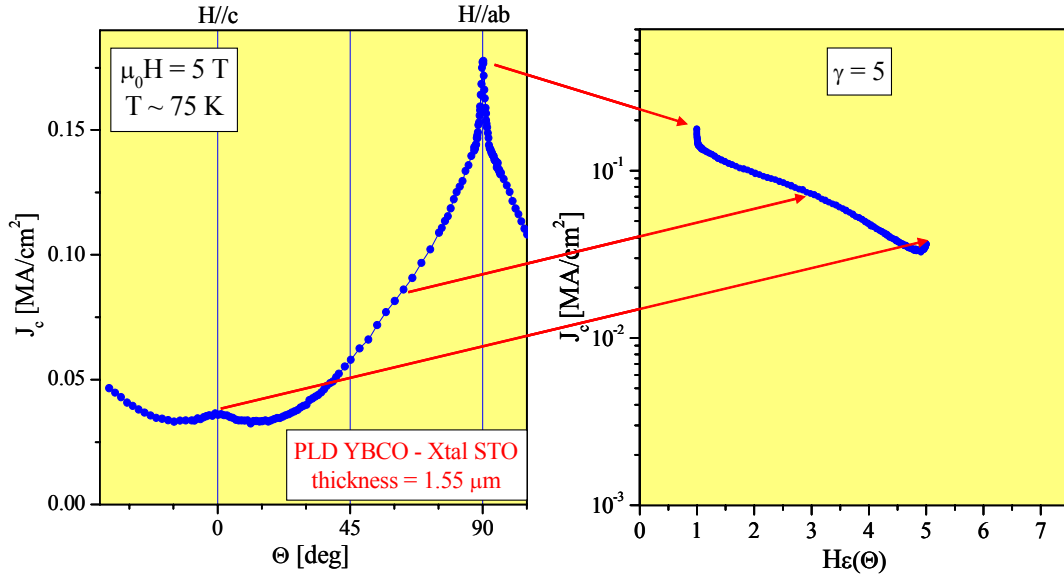
Fig. 24a. Critical current density as a function of applied field direction for YBCO at 5 T and 75 K.

Fig. 24b. Data of Fig. 24a transformed into scaled coordinates.

If the J_c vs. angle data for a number of field magnitudes for the sample of Fig. 24a are transformed into scaled coordinates and plotted together, Fig. 25a is the result. The data all fall on (scale to) a single smooth curve (with the exception of the data for the regions near $\Theta = 0°$ and $90°$). This indicates that the pinning is dominated by random defects. If this smooth curve is transformed back into the original coordinates, then at 5 T the plot shown in Fig. 25b results. Because the two curves overlap for most of the angular range, we identify the pinning over this range as dominated by random defects. Near $0°$ (along the c axis) and $90°$ (in the ab planes), we have previously determined that extended defects cause the excess pinning. What had not been demonstrated previously was to produce an independent determination of the anisotropy γ, to demonstrate that the analysis also applies at other temperatures and for other conductor architectures, and to show if and how the pinning properties could be improved.
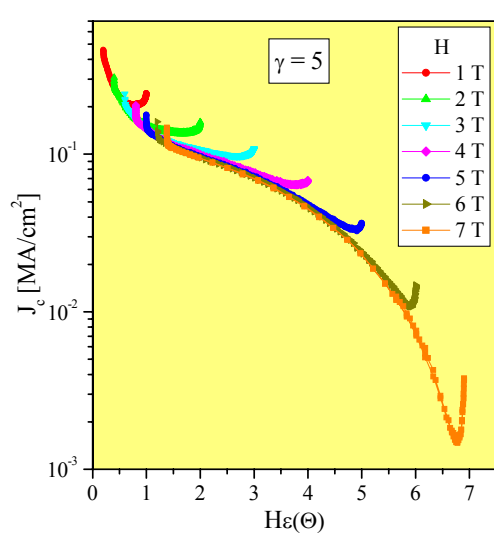
Fig. 25a. Critical current density as a function of scaled coordinates for YBCO at many fields and 75 K.
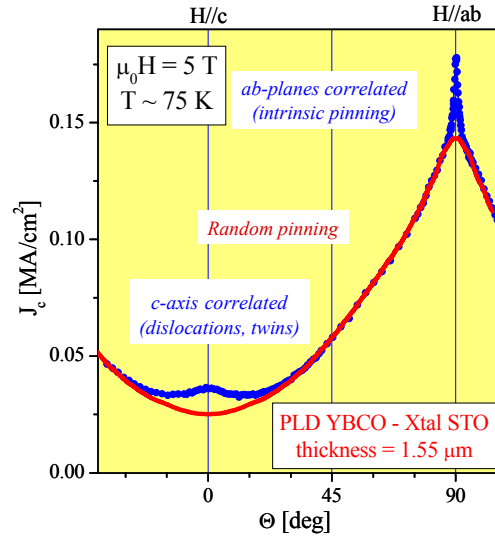
Fig. 25b. Data of Fig. 24a (blue) and smooth curve (red) determined from dated plotted against scaled coordinates from Fig. 25a transformed back into angle space.

Measurements of the angular dependence (at 30, 60, and 89°) of the irreversibility line (Fig. 26), the magnetic field line at which J_c becomes zero as a function of temperature, and scaling these yields a best fit with a γ value of 5, thus validating the previous analysis, which had selected the value of γ based on the electronic mass anisotropy.
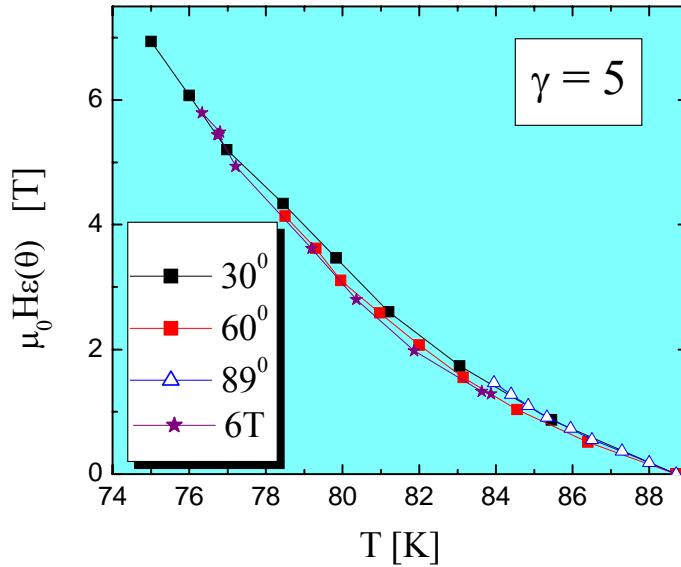
Fig. 26. Irreversibility line for a YBCO thin film for various applied field angles.

The anisotropic scaling method also works at 79 K and with a temperature independent γ = 5. Figs 27a and b show the scaling for a YBCO film on single-crystal STO. Scaling similar to that observed at 75 K is also seen at this elevated temperature.

Fig. 27a. Critical current density as a function of angle for a YBCO film at 79 K.

Fig. 27b. Critical current density as a function of scaled angle for a YBCO film at 79 K.

By examining the relative strengths of the random (uncorrelated) and correlated order as a function of temperature, it has become clear that correlated order becomes increasingly important as the temperature decreases. This is illustrated in Fig. 28 for J_c data at 79 K and 70 K for the same YBCO film. At 6 T, there is no c-axis correlated order present at 79 K, but a large peak is seen at 70 K. At 1 T, the spatial extent of the c-axis correlated pinning is larger at 70 K than at 79 K.

Using the data of Fig. 28 and data presented earlier for 75 K, it is possible to construct a schematic phase diagram (Fig. 29) of the various pinning regimes for YBCO films. A common feature that is found for all fields is that both the c-axis correlated pinning regime and the ab-plane correlated pinning regime get wider in angle as the temperature is decreased. At very high fields and high temperatures and more dramatically away from the ab plane, (upper part of 6 T diagram), the irreversibility line appears and $J_c = 0$ above that line. At 1 T, the irreversibility line is above 85 K at all angles.

Fig. 28a. Critical current density as a function of angle for 1 and 6 T at for a YBCO film at 79 K.
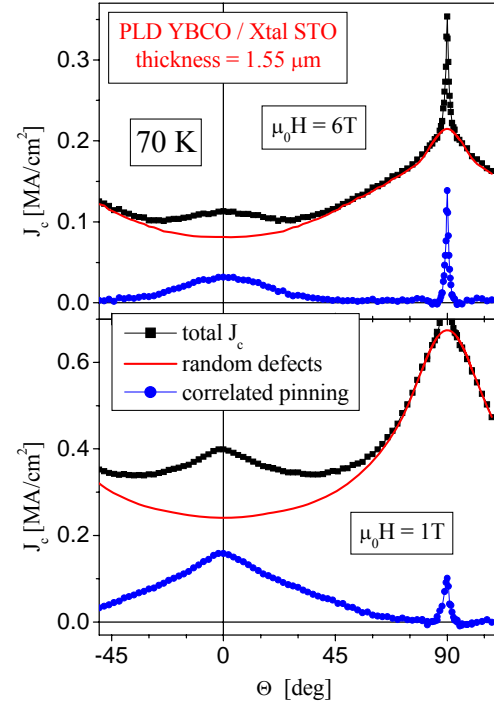
Fig. 28b. Critical current density as a function of angle for 1 and 6 T at for a YBCO film at 70 K.
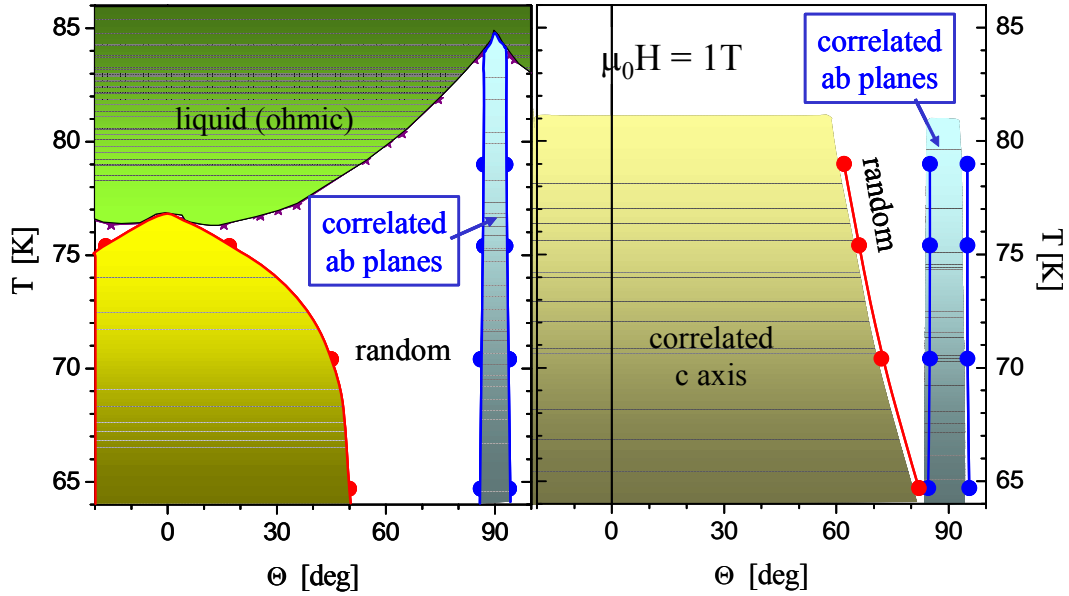
Fig. 29. Pinning regime phase diagram for YBCO thin films as a function of angle and temperature with magnetic field as a parameter.

Directional pinning is caused by correlated disorder. This disorder is the result of extended parallel defects, which can be of several types. Dislocations and columnar defects form linear extended defects, and twin boundaries form planar defects. J_c is proportional to the length of vortex that is pinned, such that an aligned vortex (Fig. 30a) has the highest J_c. As the field angle is directed away from the defect direction, the vortex distorts into a staircase vortex (Fig. 30b). As the field angle is increased further, the length of vortex that is pinned decreases (along with J_c) until it eventually becomes unpinned at the "trapping angle" (Fig. 30c, d). Both the height and width of the correlated disorder peaks are proportional to the pinning energy, so they both increase with decreasing temperature and increasing density and/or strength of correlated defects. For H//c: H_{irr}, the irreversibility field, and J_c at high H grow strongly with decreasing T.
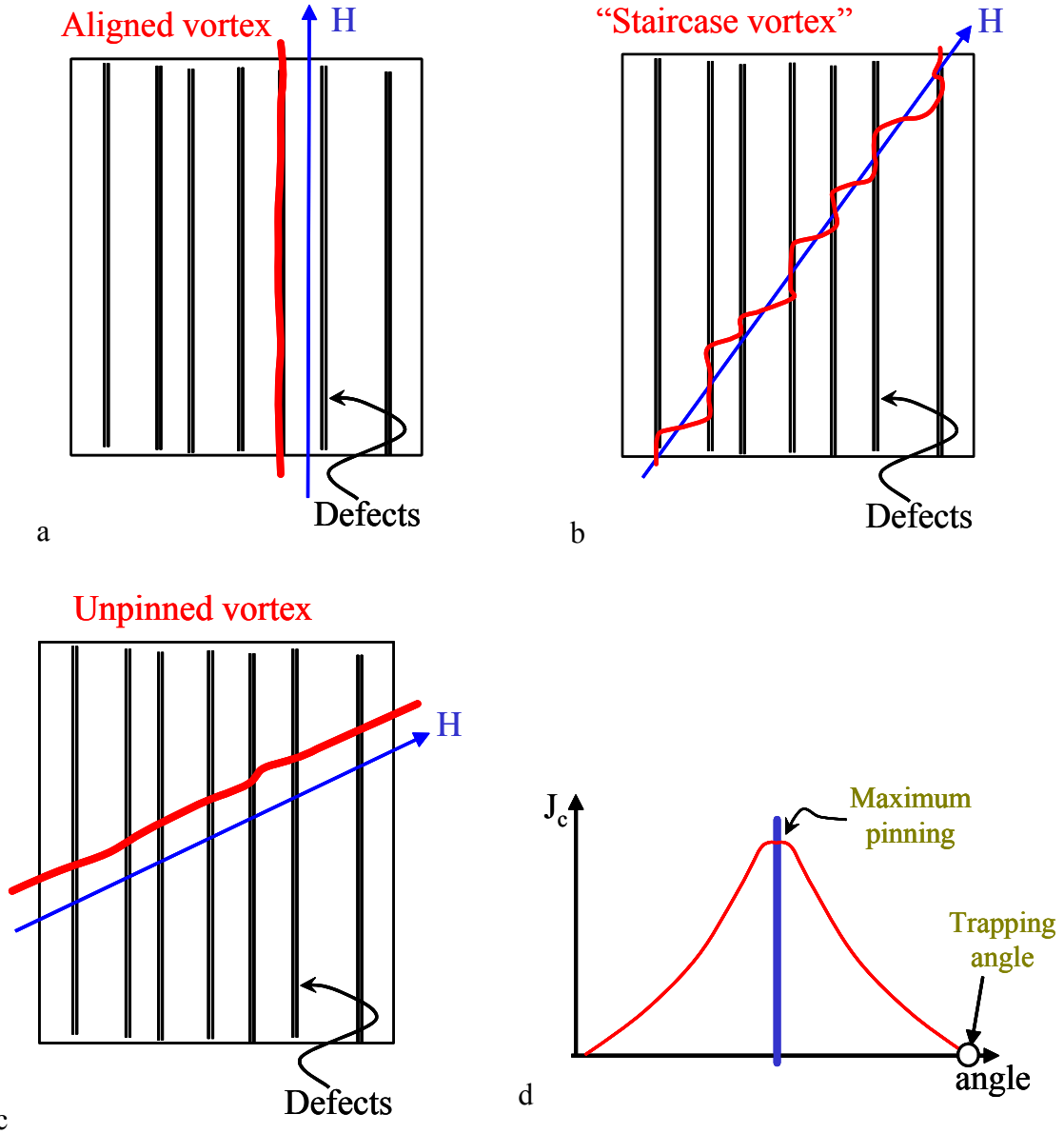
Fig. 30. Schematic illustrations of correlated defects and vortex pinning lines of different angular orientation (Fig. 30a-30c). Fig. 30d shows the relation between this angle and the pinning force.
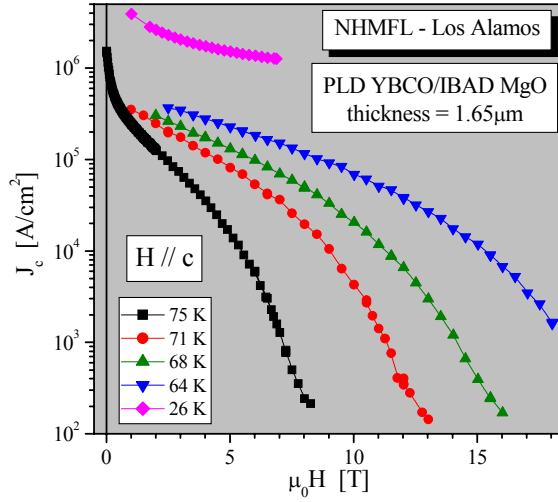
Fig. 31. Critical current density as a function of magnetic field to 18 T for a YBCO coated conductor film.

With the availability of $J_c(H//c, T)$ data to very high magnetic fields (Fig. 31), the irreversibility field H_{irr} can be determined to lower temperatures, and the data can be scaled so that it is possible to predict J_c values at given H and T. Fig. 32a shows the scaling of the J_c data as a function of magnetic field for the data shown in Fig. 31. The data are even more revealing when plotted as log-log, Fig. 32b. Now it is seen that there are two different pinning mechanisms at low and high fields separated by a field value $H_{cr}(T) \sim 0.15*H_{irr}(T)$. At low fields, the technologically important regime, $J_c \propto H^{-\alpha}$. The parameter α is architecture independent, repeatable, and temperature independent for YBCO. It is thus a useful characterization tool (smaller α is better) for YBCO. At higher fields above H_{cr}, J_c drops off more rapidly as H approaches H_{irr}.
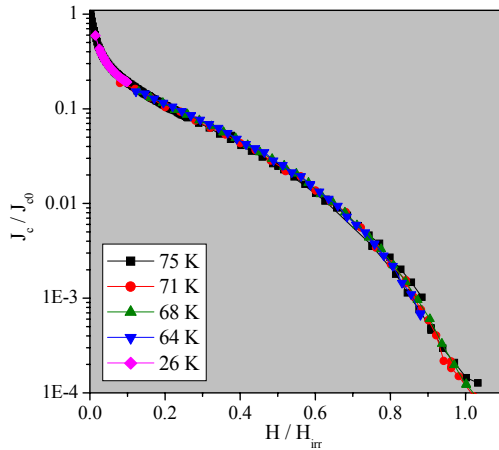
Fig. 32a. Data of Fig. 31 scaled to J_c at self field and to the irreversibility field.
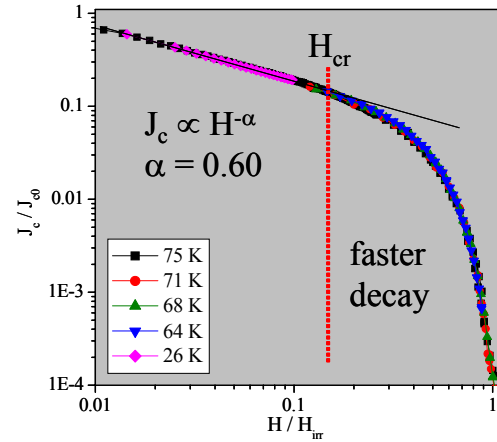
Fig. 32b. Data of Fig. 32a plotted on a log-log scale showing the different J_c regimes.

Extrapolation of H_{irr} and H_{cr} to lower temperatures using the data of Fig. 32, the magnetic phase diagram of Fig. 33 can be drawn. This shows the three field curves $H_{c2}(T)$, $H_{irr}(T)$, and $H_{cr}(T)$, which act as boundary lines. Above H_{c2}, the material is no longer superconducting, between H_{irr} and H_{c2} it is superconductive but $J_c = 0$, between H_{cr} and H_{irr} $J_c \sim e^{-H}$, and below H_{cr} $J_c \sim H^{-\alpha}$. Below about 40 K it is only the regime below H_{cr} that is practically relevant.
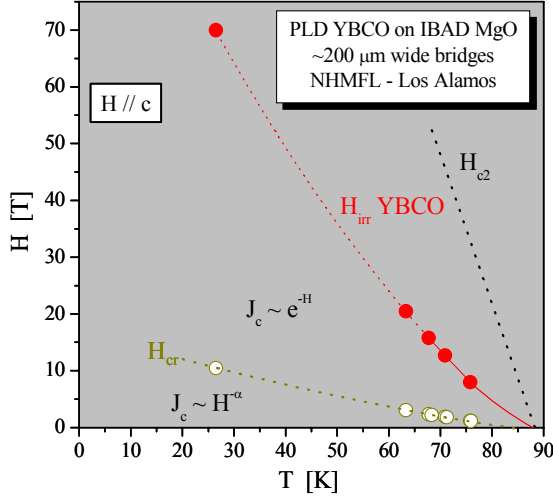
Fig. 33. Magnetic phase diagram for YBCO coated conductor for H//c.

Part II: Improving Pinning

There are three possible practical ways to enhance pinning. Adding more line defects can be accomplished using miscut substrates, lower growth temperatures (smaller island sizes), or addition of heteroepitaxial nanoparticles. Adding more point defects (and associated strain) can be achieved using cation or anion vacancies or RE-Ba cross substitution. Adding volume defects (and associated strain) can be accomplished using second phase particles, interlayers of non-superconducting material, or by substrate surface roughening. Many of these have been investigates with the exception of adding point defects.

Here, we have investigated and demonstrated four different routes to enhance pinning in YBCO. In Method 1, we change the RE ion size variance, which introduces random point defects. In Method 2, we change the average RE ion size, which introduces random point defects and correlated defects. In Method 3, we introduce buffer layer surface roughness, which results in more low angle grain boundaries ∥ c. In Method 4, we introduce heteroepitaxial second phases, which increases the c-axis dislocation density.

Substrates used were single crystal $SrTiO_3$, $SrTiO_3$-buffered single crystal MgO and $SrTiO_3$-buffered IBAD MgO. All of the films were around 1-1.5 μm thick and were grown by pulsed laser deposition (PLD) using standard YBCO conditions for all samples.

In Method 1, the ion size variance is changed keeping the mean ionic radius constant. The variance is defined as $\sigma^2 = \Sigma y_i <r_i>^2 - <r_A>^2$ where σ^2 is the variance of the mixture of RE ions I, y_i is the mole fraction of ion I, r_i is the ionic radius of ion I, r_A is the mean ionic radius $r_A = 1.019$Å, i.e., the ionic radius was kept constant at the size of Y^{3+}. The aim is to produce random variations in the oxygen ion displacements. Fig. 34 indicates the crystal structures for small and large variance. Changing the RE ion size does not

change the Cu(2)-O(2) plane buckling but increases the Cu(2)-O(1) distance by ~2.5% across the RE series.
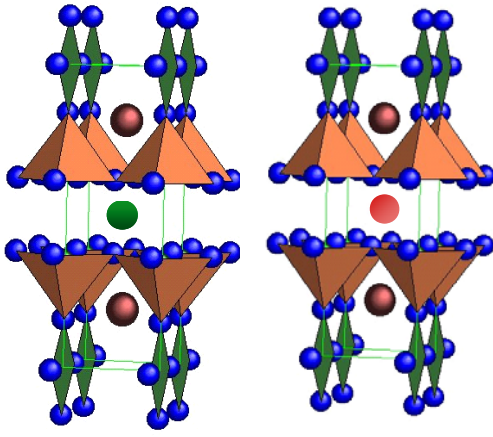
Fig. 34a. YBCO is on the left and a substituted REBCO with small variance in size on the right. The RE ion is in the midplane between the Cu-O tetrahedral.
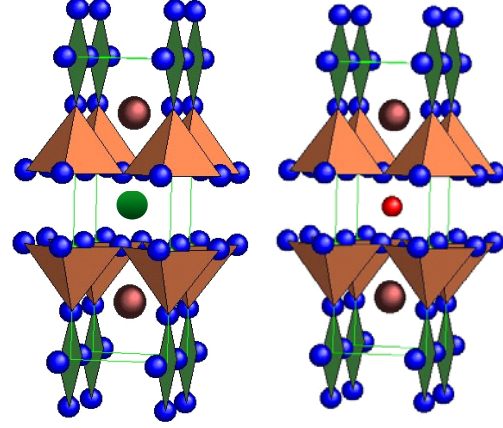
Fig. 34b. YBCO is on the left and a substituted REBCO with large variance in size on the right.

Fig. 35a indicates that there is a systematic, reproducible, and improved pinning dependence on RE ion size variance. The maximum enhancement in J_c in a 0.2 T H//c magnetic field is attained for small values of the variance. The variance effect is intrinsic and therefore should work for any processing route. Field angular measurements (Fig. 35b) indicate that random, point-like defects are responsible for the increased J_c. Note that J_c is improved for all angles. The normalized plot shows that there is only an increase in non-correlated, random point-like defects due to the variance.
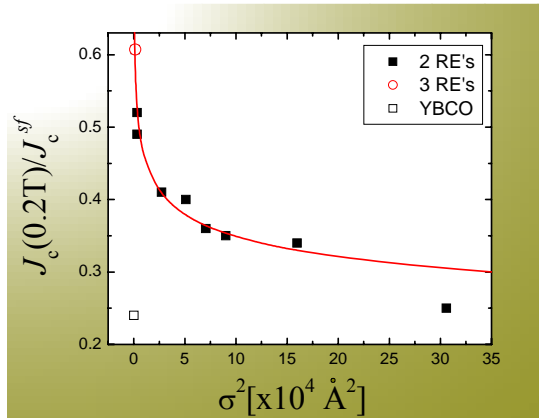
Fig. 35a. Normalized critical current density as a function of size variance. From J.L. MacManus-Driscoll et al. APL 84 (2004) 5329.
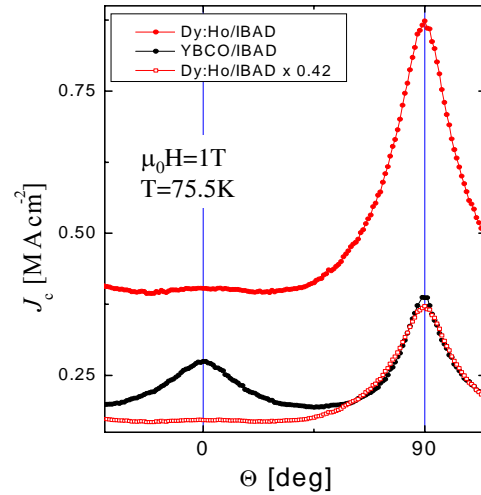
Fig. 35b. Jc as a function of angle for a YBCO and a $Dy_{1/3}Ho_{2/3}BCO$ sample (the highest J_c for a 2 RE sample shown in Fig. 35a).

Fig. 36 shows that J_c versus field improved by up to a factor of 2 for the lowest variance sample and that the enhancement was present at up to 4 T at 75.5 K and up to 6 T at 65 K.
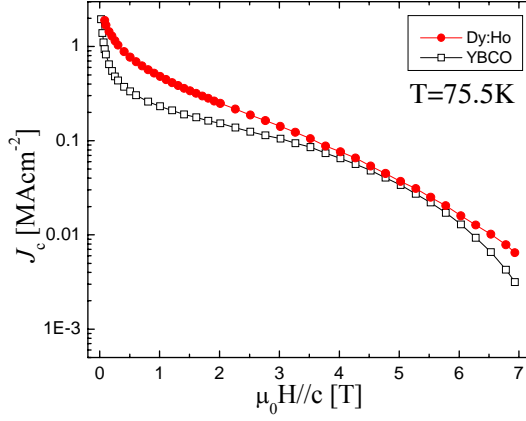
Fig. 36a. Critical current density as a function of magnetic field at 75.5 K for a small ion size variance sample.
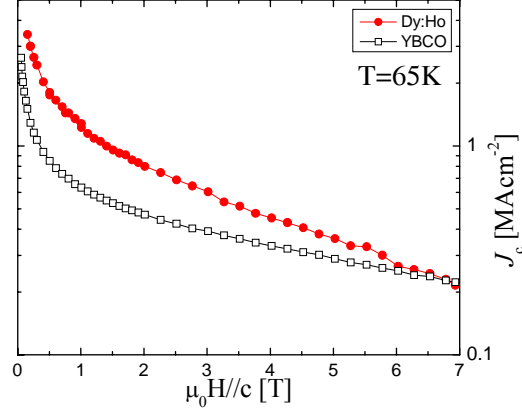
Fig. 36b. Critical current density as a function of magnetic field at 65 K for a small ion size variance sample.

In Method 2, a change in the average RE ion size with fixed variance introduces random points defects and correlated defects. We found no systematic dependence of pinning on RE ion size. This is not surprising since the amount of Y-Ba cross substitution (Fig. 37a) is strongly dependent on kinetics, which are not easily controlled. However, we did observe large enhancements of J_c for a sample of $Y_{1/3}Sm_{2/3}BCO$ ($<r_A>=1.039$Å) relative to YBCO ($<r_A>=1.019$Å); $\sigma^2 = 6\text{-}8 \times 10^{-4}$ Å^2 for this sample. On STO this composition resulted in self-field J_c values up to 5 MA/cm^2 in 1 μm thick films. On IBAD the $J_c(H)$ improved by a factor of 2-10 relative to YBCO depending on the magnitude of H, Fig. 37b. The RE ion size effect is intrinsic and hence should also work for any processing route. (J.L. MacManus-Driscoll et al., App. Phys. Lett **86** (2005) 32505)
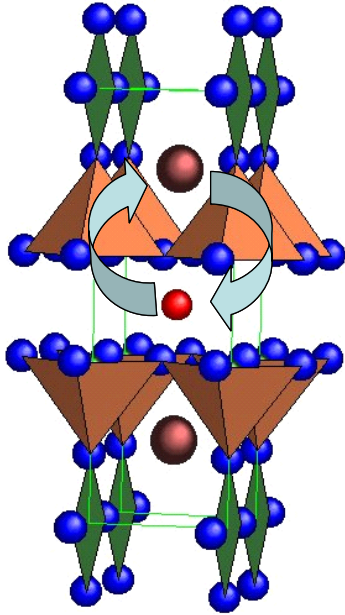
Fig. 37a. REBCO structure changing the average size of the RE ion.
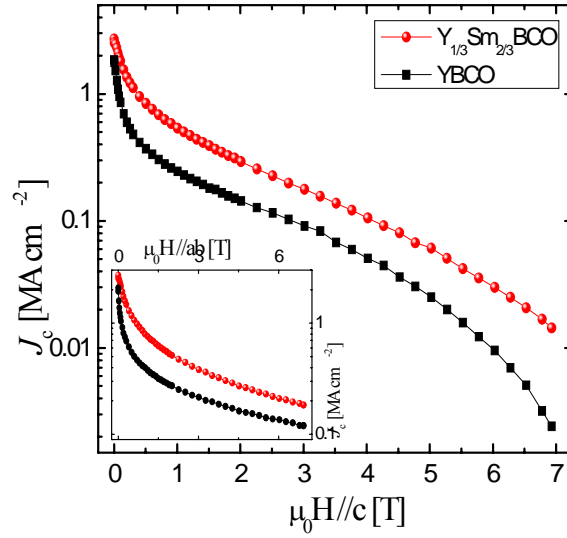
Fig. 37b. Critical current density at 75 K as a function of magnetic field for 1.2 µm thick YBCO and REBCO samples on IBAD with optimized RE ion size.

In Method 3, we introduce buffer surface roughness resulting in more low angle grain boundaries ∥ c, Fig. 38. Low temperature growth of the STO buffer layer is used to increase the surface roughness. The YBCO films are deposited at 760°C in all cases.
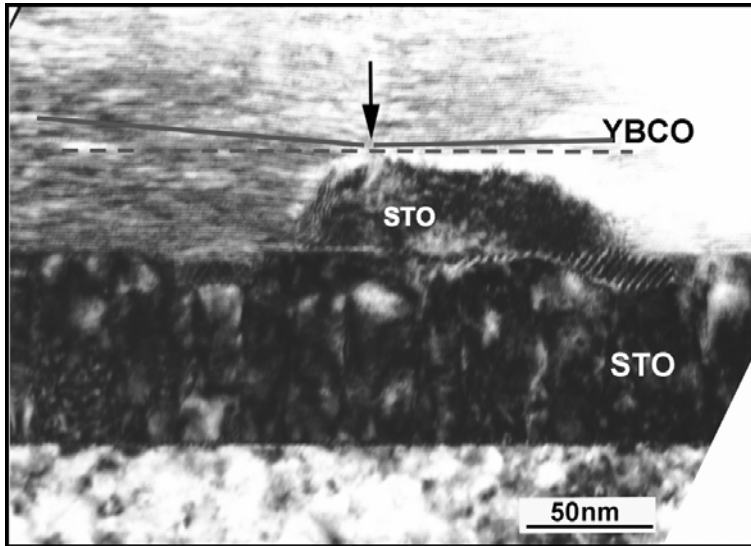
Fig. 38. Low angle grain boundary in YBCO initiated by particle on STC buffer surface. H. Wang et al., J. Mat. Res. 19 (2004) 1869.

The in-field dependence of J_c (Fig. 39) is improved in 5µm thick films on IBAD-MgO. The sample with STO buffer deposited at 700°C has a lower self field, but a higher in

field J_c compared to the buffer deposited at 820°C. Investigating the angular dependence of J_c, it is clear that this enhancement of J_c is due to a larger c-axis peak.
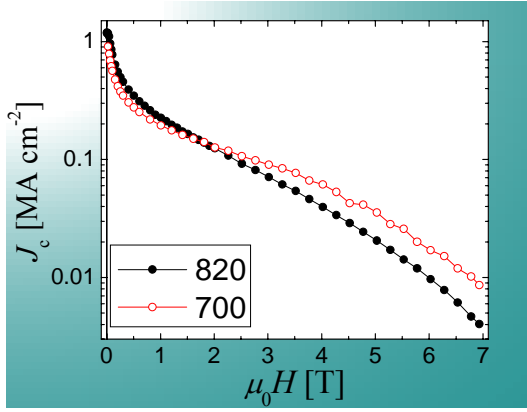
Fig. 39a. Critical current density as a function of magnetic field for YBCO on STO buffers grown at 700°C and 820°C. B. Maiorov et al., Ceramic Transactions 160 (2005) 3.
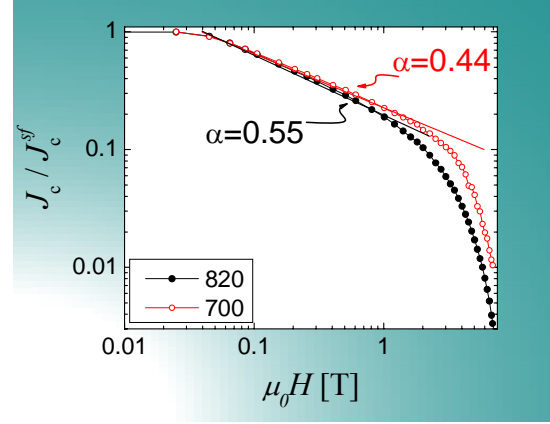
Fig. 39b. Normalized J_c as a function of magnetic field showing the α parameters for the samples of Fig. 39a.

The angular dependence of J_c (Fig. 40) shows a larger c-axis peak for YBCO film on the STO buffer grown at 700°C, and is consistent with the presence of low angle grain boundaries //c introduced by tilted a-b planes induced by buffer surface roughness.
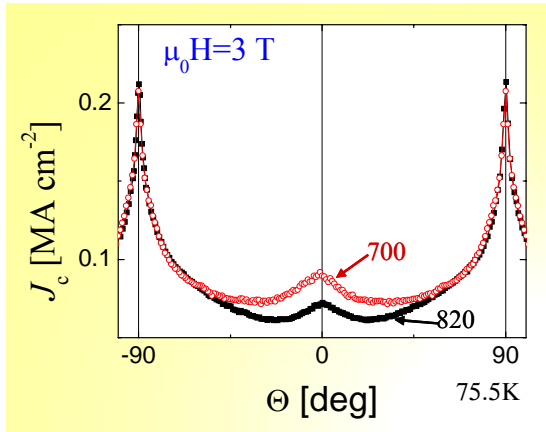
Fig. 40. Critical current density as a function of angle for two YBCO films with STO buffers grown at different temperatures.

In Method 4 [J.L. MacManus-Driscoll et al., Nature Materials **3** (2004) 439], we introduce heteroepitaxial second phases to increase the c-axis dislocation density. Materials need to be carefully selected for the second phase: the ability to grow heteroepitaxially with YBCO; the size of the lattice mismatch producing strain leading to misfit dislocations; a high melting temperature phase, yielding slow growth kinetics and hence small particles; and chemical compatibility with YBCO. We also used a simple method of second-phase incorporation: a ceramic target of YBCO+ 5 mol% $BaZrO_3$ that was fabricated and ablated to form the film samples.

The SEM images in Fig. 41 show the presence of 10-100 nm sized $BaZrO_3$ nanoparticles on the film surface of a YBCO + $BaZrO_3$ film surface in comparison to that of a YBCO

film. The TEM images in Fig. 42 show the presence of edge dislocations in the YBCO and nearly a 5-fold increase in density of c-axis oriented dislocations ($\sim 400/\mu m^2$ vs. $80/\mu m^2$).
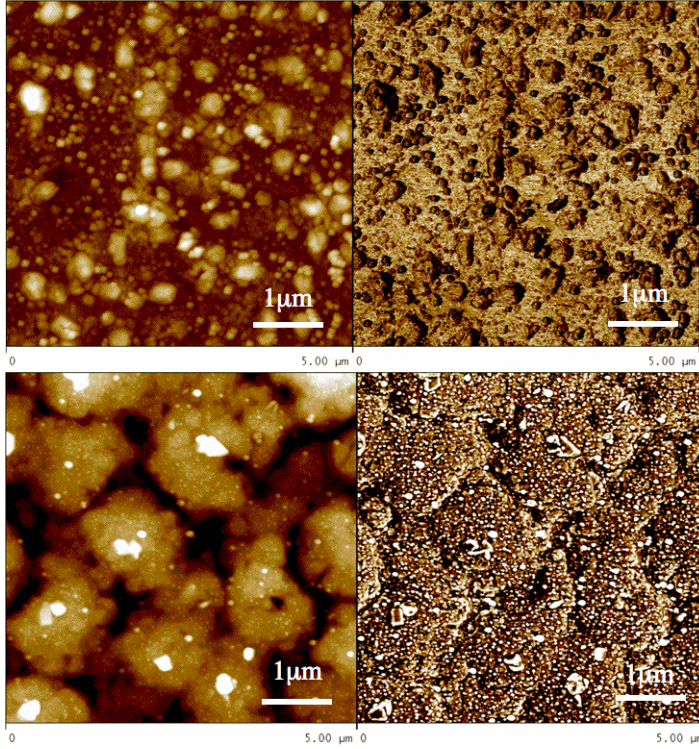
Fig. 41. Micrographs of surface of YBCO film (top) and YBCO + $BaZrO_3$ (bottom), the latter showing the presence of 10-100 nm surface particles.
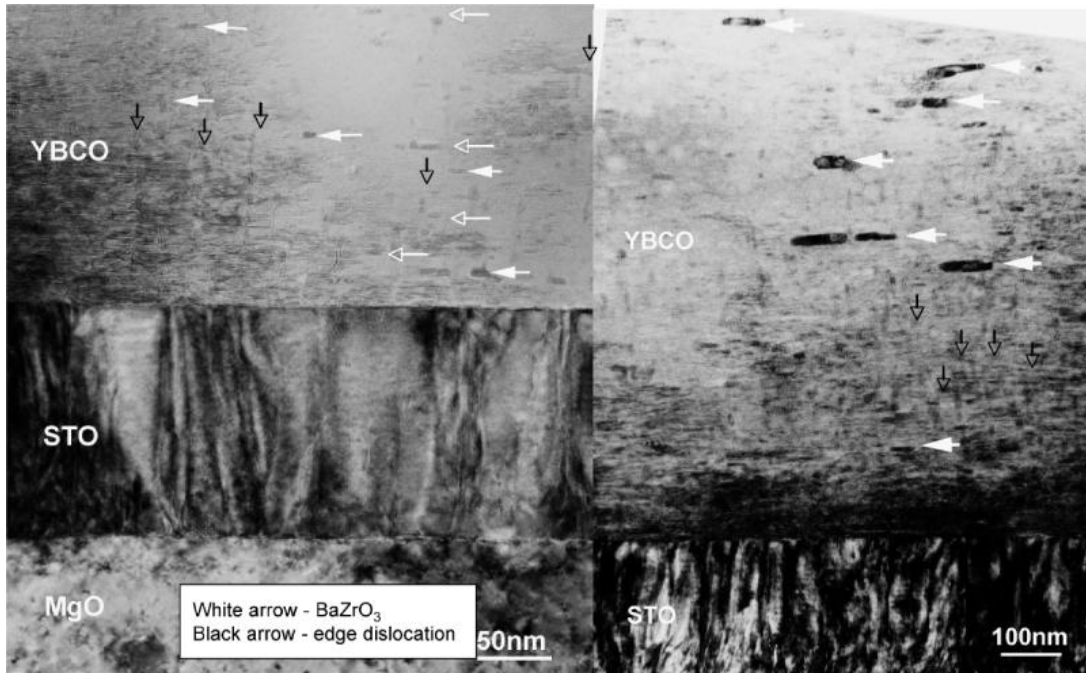
Fig. 42. TEM images of $BaZrO_3$-doped YBCO showing the $BaZrO_3$ nanoparticles and a high density of edge dislocations.

Additionally, high resolution TEM (HRTEM) (Fig. 43) and EDX show the presence of $BaZrO_3$ nanoparticles embedded within the film. Image analysis of the micrographs yields a modal particle size for $BaZrO_3$ of 10 nm with < 10% of the particles 30 nm or larger.
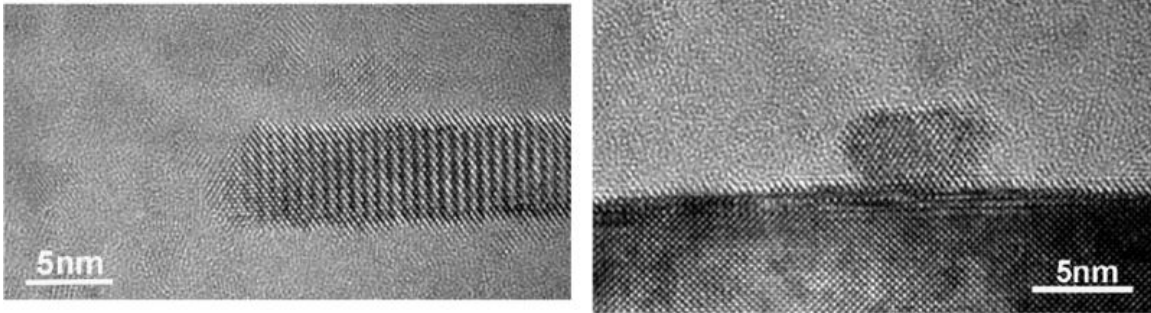
Fig. 43. HRTEM images of $BaZrO_3$ nanoparticles embedded in the YBCO film matrix.

The enhancement of J_c as a function of magnetic field for YBCO+$BaZrO_3$ and YBCO samples (Fig. 44) shows a 1.5-5x increase in J_c for the doped samples. In addition, the 'α' value is much lower (0.33 vs. 0.55) for YBCO+$BaZrO_3$. The angle dependent J_c data (Fig. 45) show a huge enhancement in the c-axis peak, which is consistent with the additional c-axis dislocations.
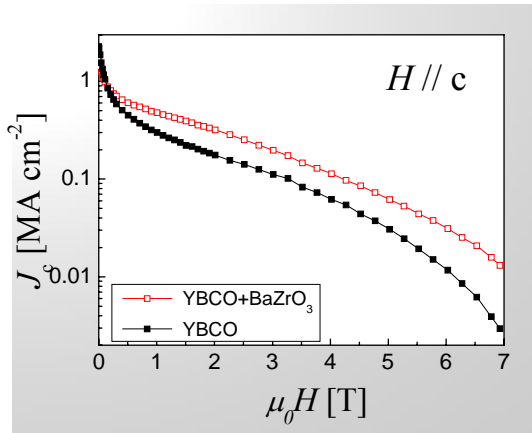
Fig. 44a. Critical current density as a function of magnetic field for doped and undoped YBCO.
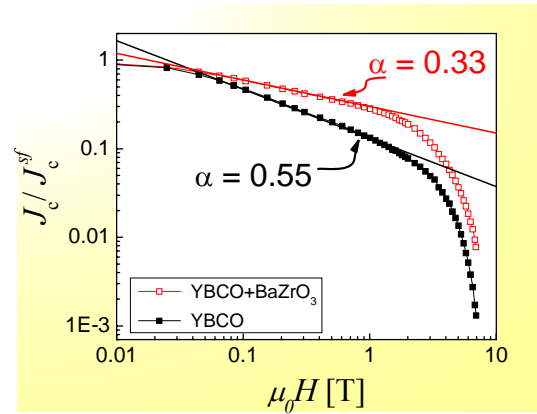
Fig. 44b. Scaled critical current density as a function of magnetic field for doped and undoped YBCO and the α analysis.
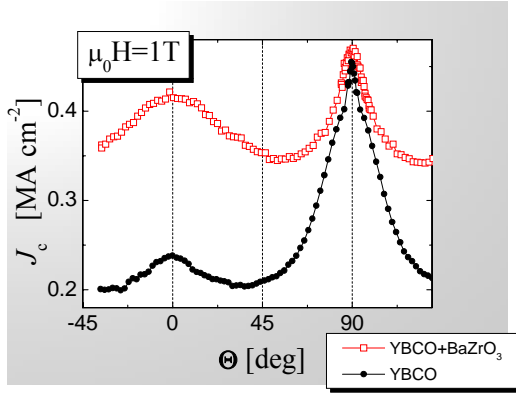
Fig. 45. Critical current density as a function of angle showing the large enhancement in the c-axis pinning for YBCO + BaZrO$_3$.

Part III. Angular dependence of J$_c$ in CC with different architectures.

Previously, our emphasis has been on determining the pinning properties and mechanisms in YBCO films produced by PLD on buffered single-crystal substrates or MgO IBAD. It is also of great interest to examine YBCO films deposited by other techniques on these same templates or on those produced by other techniques, such as roll-assisted biaxially textures substrates (RABiTS). The goal of this research is to determine how the relative importance of the pinning mechanisms identified in PLD/IBAD MgO changes depending on the film microstructure.

We use as our first model system YBCO deposited by the metal oxide chemical vapor deposition (MOCVD) process prepared by SuperPower, Inc. J$_c$(Θ) in "standard" YBCO MOCVD films on IBAD shows both a c-axis peak and a correlated ab-plane peak. The results of the analysis of such a film are shown in Fig. 46. The film characteristics are qualitatively similar to those of YBCO produced by PLD.
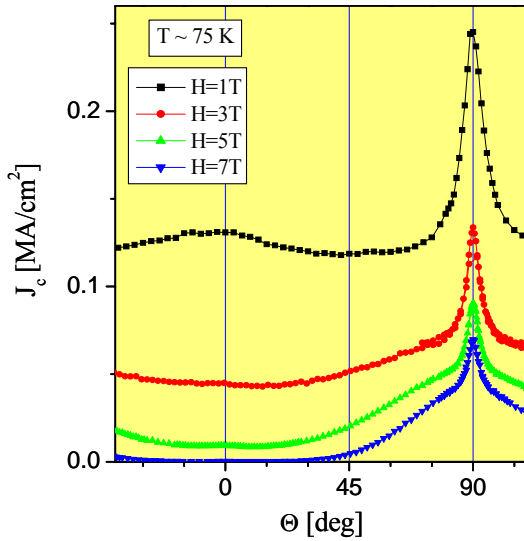
Fig. 46a. Critical current density at 75 K as a function of angle for a YBCO film produced by
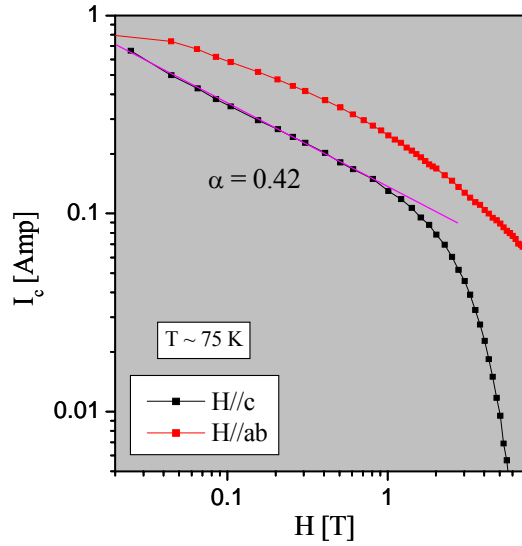
Fig. 46b. Critical current as a function of magnetic field for a YBCO film showing the α analysis.

43

MOCVD.

Large J_c improvements have been obtained by Sm doping of the YBCO ($Y_{0.9}Sm_{0.1}BCO$). Fig. 47a shows that there is a very large c-axis peak with Sm doping, but that the α value (Fig. 47b) is the same as in pure YBCO (~0.42).
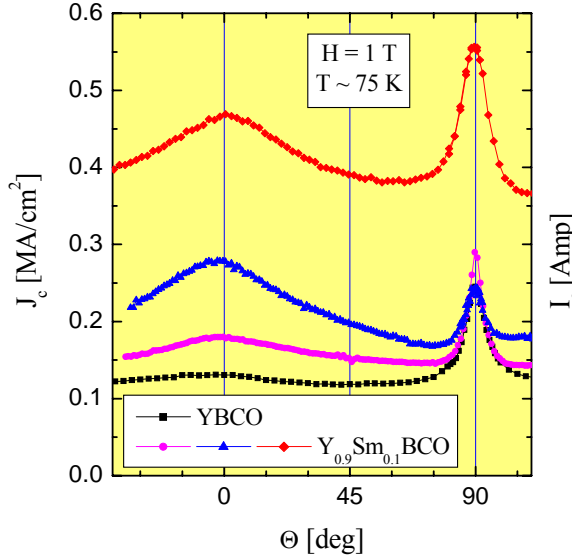
Fig. 47a. Critical current density at 75 K as a function of angle for a Sm doped YBCO film.
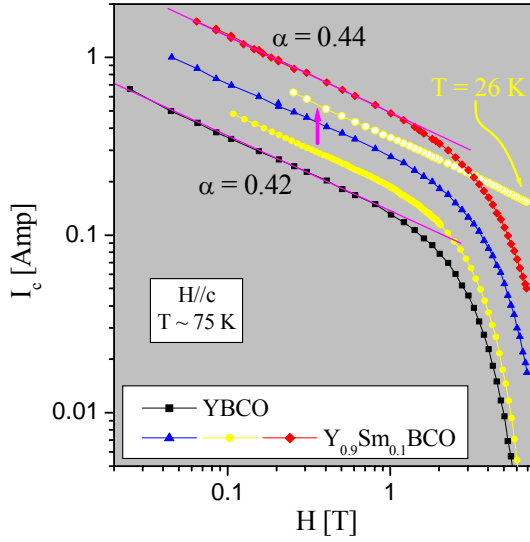
Fig. 47b. Critical current as a function of magnetic field for a Sm doped YBCO film showing the α analysis.

A further check of consistency of sample microstructures and of the analytical technique is to compare data for YBCO films produced at LANL by PLD on SuperPower IBAD MgO and on LANL IBAD MgO. Fig. 48 shows an analysis of the J_c data comparing these two samples, and it is seen that they have essentially identical J_c performance. This is reflective of the robustness and maturity of the IBAD technology.
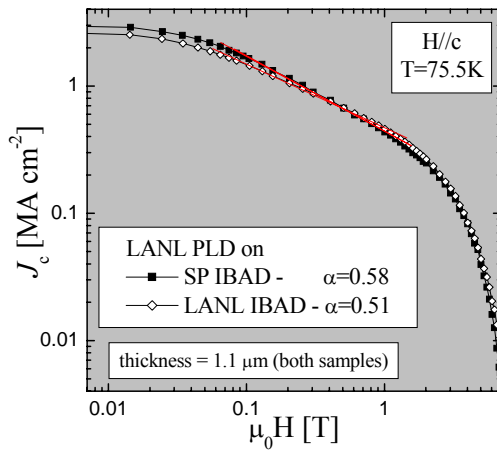
Fig. 48. Critical current density as a function of magnetic field for YBCO films prepared by PLD on LANL IBAD and on SuperPower IBAD.

In our investigation of the $J_c(\Theta)$ dependence for YBCO films produced by metal oxide deposition (MOD), we examined films prepared by American Superconductor Corporation (AMSC). MOD films have a very different microstructure, layered rather than columar for the PLD films. We have found that J_c is reproducible and very similar for MOD films on single crystal substrates and on RABiTs, as shown in Fig. 49.
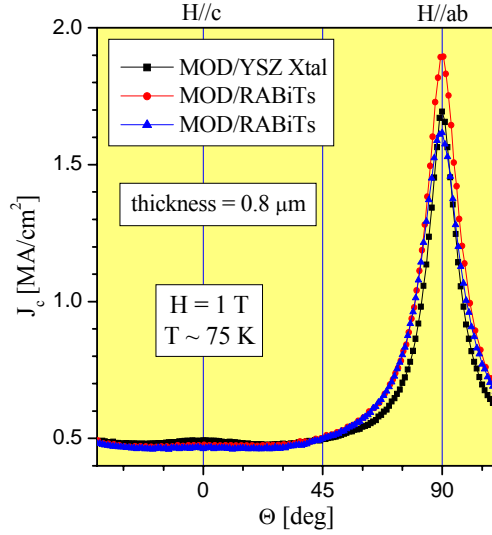
Fig. 49. Comparison of critical current density as a function of angle for MOD YBCO deposited on a single crystal and on RABiTS. $J_c(sf)$ values for these films (top to bottom in the legend) are 3.6, 3.3, and 3.1 MA/cm^2. The RABiTS samples are from two long tapes.

Comparing the angular dependence of J_c for MOD and PLD films we see that there are two very different behaviors. The MOD film (Fig. 50a) has a small c-axis peak and a large ab-plane peak, whereas the PLD film (Fig. 50b) has a large c-axis peak and a relatively smaller ab-plane peak.
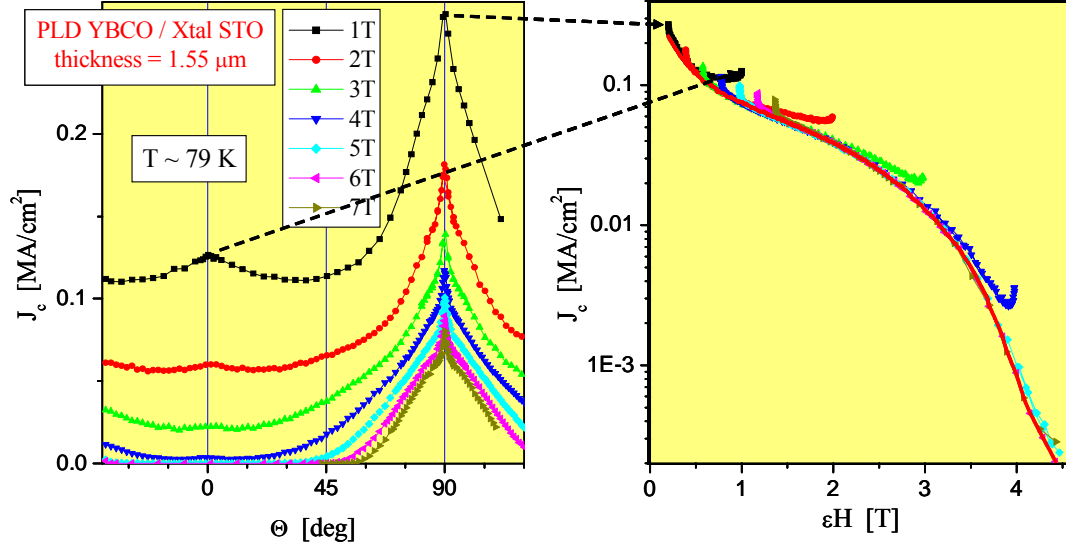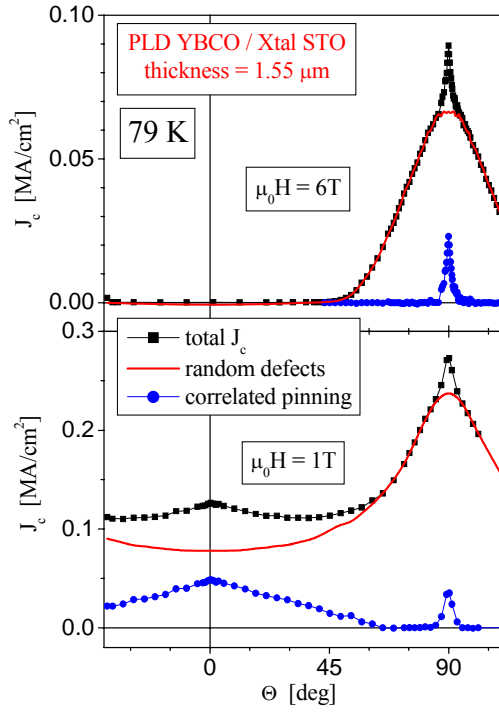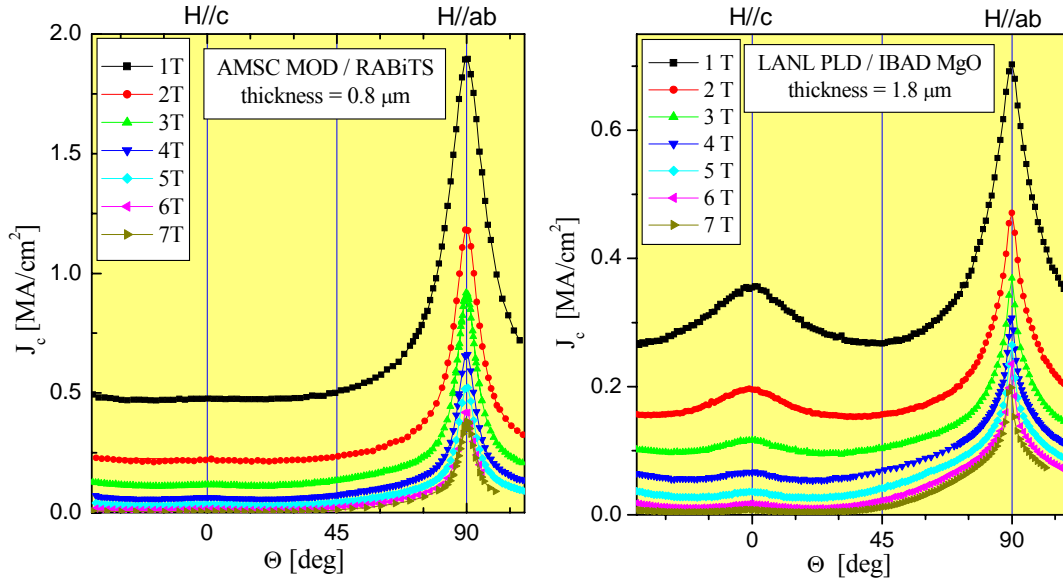
Fig. 50a. Critical current density as a function of angle for a MOD YBCO film on RABiTS.

Fig. 50b. Critical current density as a function of angle for a PLD YBCO film on IBAD MgO.

The pinning differences between the MOD and PLD films clearly correlate with their structural differences. The MOD YBCO films (Fig. 51a) show a laminar growth morphology. They have many ab-plane correlated defects: stacking faults. These result in enhanced ab-plane pinning. In contrast, PLD YBCO films (Fig. 51b) exhibit a columnar growth morphology. These films have many c-axis correlated defects: dislocations. As a result, these films show enhanced c-axis pinning.
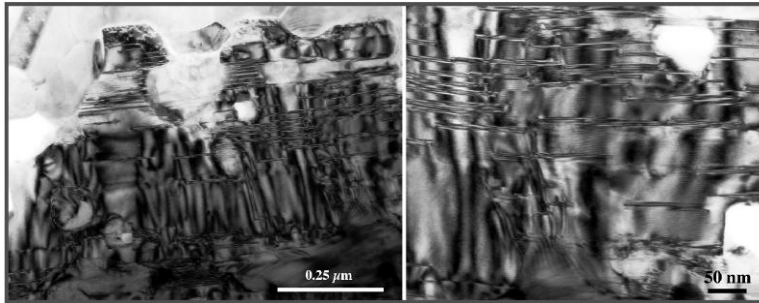
Fig. 51a. TEM cross sectional micrographs of an AMSC MOD YBCO film on RABiTS.
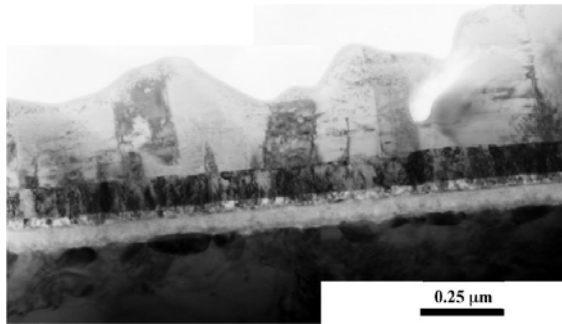
Fig. 51b. TEM cross sectional micrograph of a PLD YBCO film on IBAD MgO.

Because of the larger density of correlated defects along the ab-planes in MOD films, the field dependence of J_c for H//ab is better in these films (Fig. 52) than in those made by PLD. In contrast, the field decay of Jc for H//c is faster in MOD films because of their smaller c-axis peak (α ~0.7). Nanoparticle doping in MOD films is able to improve α to ~0.6.
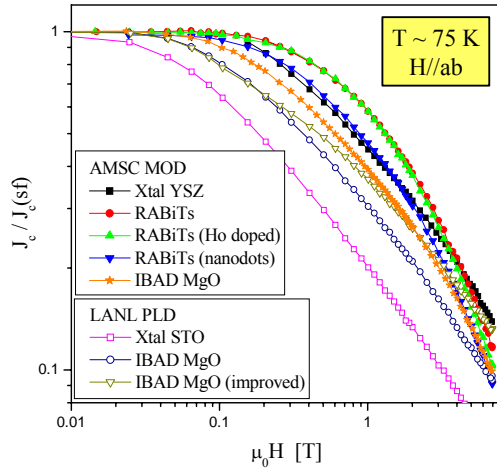
Fig. 52. Critical current density as a function of magnetic field parallel to the ab plane for YBCO films at 75 K.

Correlated defects along the ab planes can be distributed periodically in a technique employed by T. Haugan & P. Barnes of the Air Force Research Laboratory. In their technique, Y-123 and (very thin) Y-211 multilayers are deposited. The Y211 layers agglomerate into nanoparticles as shown in Fig. 53a. The effect of the high areal density of nanoparticles is to produce an enhancement in J_c (Fig. 53b) at a "matching field," equal to 2.5 T for the sample of Fig. 53a.
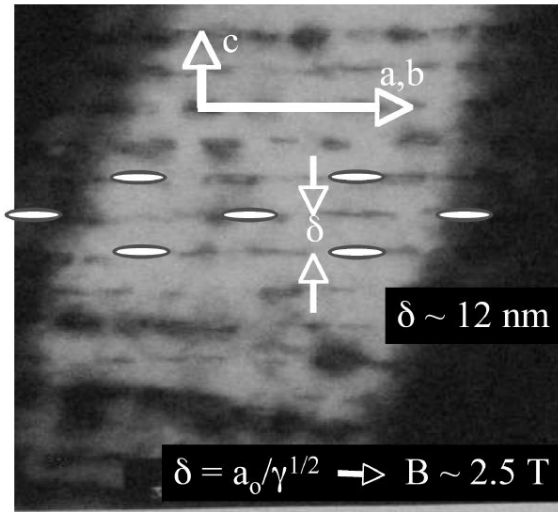
Fig. 53a. Micrograph of the Y123/Y211 multilayer sample showing Y211 nanoparticle inclusions.
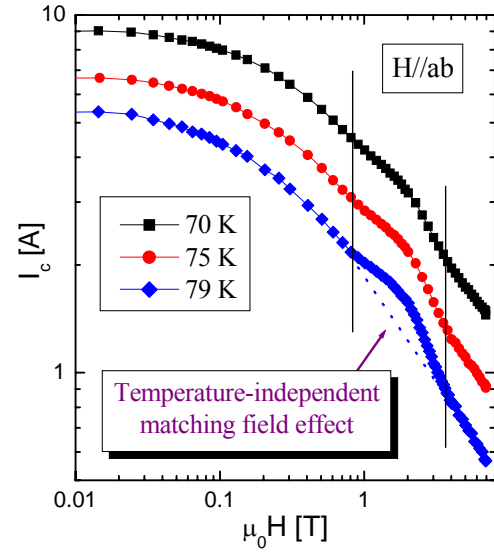
Fig. 53b. Critical current as a function of applied field (// ab) for a Y123/Y211 multilayer sample.

In addition to improving J_c in field by enhancing the pinning (decreasing α), it is also possible to increase the in-field J_c by increasing the self field J_c with no change in α. The use of YBCO/CeO$_2$ multilayers, as described earlier in this report, yielded a world record I_c, up to 1400 A/cm width in self field. In field measurements on such a multilayer are

47

shown in Fig. 54a for a film with I_c(75 K, sf) ~ 880 A/cm width. The angular and field dependence (α) are similar to that of YBCO single layer films. If the scaling data in Fig. 54b, derived from single layer YBCO films can be applied to this multilayer, than the performance at 50 K and 3 T would be the very high value of ~570 A/cm width.

Summarizing this study of understanding and improving pinning in coated conductors, we have extended our knowledge of the temperature dependence of the various pinning mechanisms previously determined, we have introduced nanoengineered defects into YBCO to improve the J_c performance, and we have investigated CCs with different microstructures.
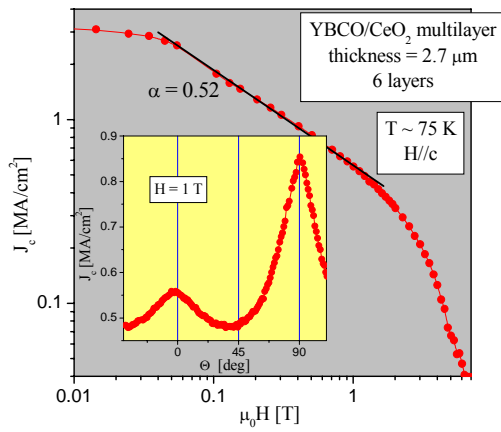
Fig. 54a. Critical current density of a YBCO/CeO$_2$ multilayer film as a function of magnetic field (// c) at 75 K . Inset shows critical current density as a function of angle at 1 T.
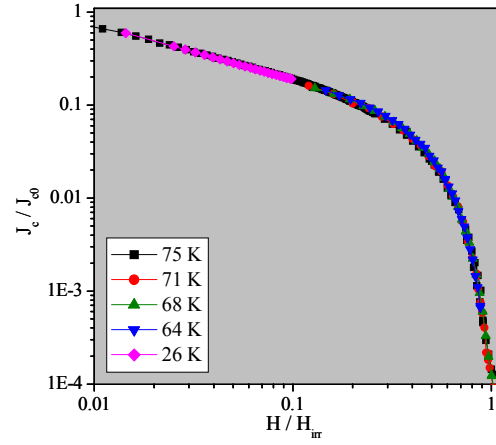
Fig. 54b. Scaled critical current density as a function of scaled magnetic field for a single layer YBCO film.

In PLD YBCO films, we have found that the angular range of influence of correlated pinning mechanisms (both along the c-axis and in the ab-planes) increases with decreasing temperature. In particular, at T ~ 26 K they are active for all field orientations. We have found that J_c for H//c can be scaled over wide ranges of H-T. This allows us to predict J_c values for arbitrary (H,T). The technologically relevant regime for H//c exhibits a power law dependence $J_c \propto H^{-\alpha}$ (α~0.6). The range of this "low field" regime increases with decreasing temperature, exceeding 7 T at 26 K.

Several successful routes have been demonstrated to nano-engineer defects into REBCO to enhance pinning. A simple, inexpensive and scaleable technique is to ablate YBCO and BaZrO$_3$. This yields BaZrO$_3$ nanoparticles and extra c-axis dislocations. The use of small but non-zero RE ion size variance and mixed RE compositions produces random uncorrelated defects. The use of mixed RE's containing Y and Sm produces random point defects and correlated defects. The use of a lower growth temperature of the STO buffer produces surface particles that cause a-b planes to tilt and result in low angle grain boundaries parallel to the c axis. All of these processes result in extra defects and enhanced J_c performance in an applied magnetic field.

In the study on the effect of different microstructures on $J_c(H,\Theta,T)$, MOCVD YBCO (and YBCO doped with Sm)/ IBAD (SuperPower) exhibits a very large c-axis peak and associated small $\alpha \sim 0.4$. This is consistent with 3D island growth and proliferation of c-axis correlated defects. The laminar growth associated with MOD YBCO (AMSC) results in a large density of planar defects parallel to the ab-planes; these dominate pinning in a wide angular range and produce a better field dependence for H//ab. A large $\alpha \sim 0.7$ for H//c is consistent with the small density of c-axis correlated defects for these films. The discontinuous Y211 layers in YBCO/Y211 multilayers (AFRL) act as a periodic extended planar defects parallel to the ab-planes and produce a tunable matching pinning effect. Finally, we determined that PLD YBCO/CeO_2 multilayers with record high I_c (up to 1400 A/cm) exhibit similar field and angular dependence of J_c as single layer PLD YBCO.

2.1.4 Comparative Study of REBa$_2$Cu$_3$O$_7$ Films for Coated Conductors

Q. X. Jia, B. Maiorov, H. Wang, Y. Lin, S. R. Foltyn, L. Civale, and J. L. MacManus-Driscoll

In the development of coated conductors, one of the main tasks is to deposit high performance superconducting films. For the superconducting films, YBa$_2$Cu$_3$O$_7$ (Y123) is the most widely investigated system. However, the use of Y123 films produced by pulsed laser deposition (PLD) for coated conductors also has its limitations. For example, the generation of particulates and outgrowth nucleation make the surface very rough for thicker films.

Recently, many efforts have been devoted to study rare-earth superconducting REBa$_2$Cu$_3$O$_7$ (RE123, RE = Nd, Sm, Eu, Gd, Dy, Ho, Er, and Yb) materials due to their many unique properties compared to Y123. It has been shown that the transition temperature of RE123 increases with the ionic size of the rare-earth. An increase on transition temperature by a value of 5 K over Y123 has been observed for Nd123, Sm123, and Eu123. Unlike Y^{3+}, for the RE's larger than Y, such as Nd^{+3}, Sm^{3+}, and Eu^{3+}, which have a similar ionic radius to Ba^{2+}. This can lead to more point defects in RE123 due to the higher possibility for RE/Ba substitution. Point defects introduced by the cation exchange between RE and Ba can be profitable since a large density of defects can act as strong vortex pinning centers. Advantages for the smaller RE materials are a lower processing temperature and wider processing window. More exceptional properties from certain RE123 materials are their much better surface morphology when they are deposited by physical vapor deposition techniques. The latter feature makes it possible to fabricate high quality multilayers desired for electronic devices. Higher deposition rate for Ho123 also makes it attractive for coated conductors. Nevertheless, there have been very limited systematic studies on the growth and characterization of high quality RE123 films. Here we report comparative studies of different RE123 films on single crystal substrates deposited by PLD.

Different RE123 films were deposited using PLD. PLD was performed using a XeCl excimer laser (λ = 308 nm, energy density at target surface 2 J/cm^2). All of the depositions were carried out at a substrate-to-target distance of 5 cm. Both substrate temperature and oxygen pressure were investigated as variables to explore the effects of processing conditions on the properties of RE123 films. It should be noted that the films were cooled to room temperature in O$_2$ at 300 Torr by turning off the power supply to the heater after the deposition. No further thermal treatment or post-annealing was performed on the as-deposited RE123 films. To deposit different RE123 films, we used stoichiometric REBa$_2$Cu$_3$O$_x$ pellets, commercially available from Superconductive Components Inc., as targets for laser ablation. To avoid the influence of substrate materials on the properties of the RE123 films, we used SrTiO$_3$ as the representative substrate for this comparative study.

To evaluate the orientation and epitaxial relationship between the substrate and the RE123 films, X-ray diffraction (XRD) patterns of the films were acquired on a Siemens D5000 four-circle diffractometer. Microstructures of a limited number of RE123 films were also studied by high-resolution x-ray diffraction using a Bede D1 x-ray diffractometer. The RE123 films were also imaged using scanning electron microscopy (SEM) and scanning tunneling microscopy (STM) to investigate the surface morphology and the detailed microstructures. The interface between the substrate and the RE123 films was also investigated using cross-sectional transmission electron microscopy (TEM).

Superconducting properties of RE123 films, such as the transition temperature and the transition width, were evaluated by using both ac susceptibility and transport measurement techniques. The critical current density was obtained by the standard four-point method from the patterned bridge using the 1 μV/cm criterion. Bridges of RE123 films were prepared using photolithography to produce patterns with dimensions of 2.0 - 6.0 mm long by 250 μm wide. The film thickness was measured after patterning using a profilometer. Field dependent critical current density measurements of RE123 films were carried out at liquid nitrogen temperature (75.5 K at Los Alamos).

From the perspective of coated conductor economics, deposition rate is an important factor for choosing superconducting materials. Under the given processing conditions, we have found that the growth rate changes widely depending on the RE123 material. Shown in Fig. 55 is the growth rate of RE123 materials as a function of the RE ion radius, where the growth rate of r_{RE} for a specific RE123 material is normalized by the rate of Y123, r_Y. It should be noted that the rates of different materials were obtained from fully modified targets. It is very interesting to note that the larger the RE ion radius, the higher the rate is.
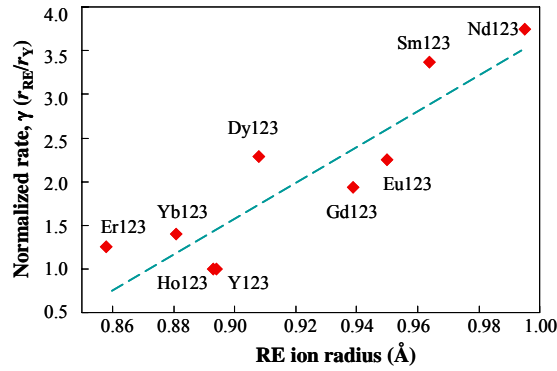
Fig. 55. Normalized growth rate of RE123 as a function of the RE ion radius. The dashed line is a guide to the eye.

It is technologically important to understand the reasons for the wide range of deposition rates, given the same processing conditions used during the growth of different RE123 films. To accomplish this, we have studied the surface morphologies of RE123 targets after extensive laser irradiation. It is well documented that the Y123 target surface is covered by "cones" after irradiation at certain PLD fluence levels. As indicated by Foltyn *et al.*, cones are formed as surrounding material is removed by successive laser pulses, and as a result of this erosion process, they grow in length as the laser exposure increases. The pronounced decrease in film deposition rate has been attributed to surface modification. In the case of RE123, the surface morphologies are quite different from Y123. Figure 56 (a), (b), and (c) show the scanning electron micrographs of Y123, Eu123, and Nd123 targets, respectively.
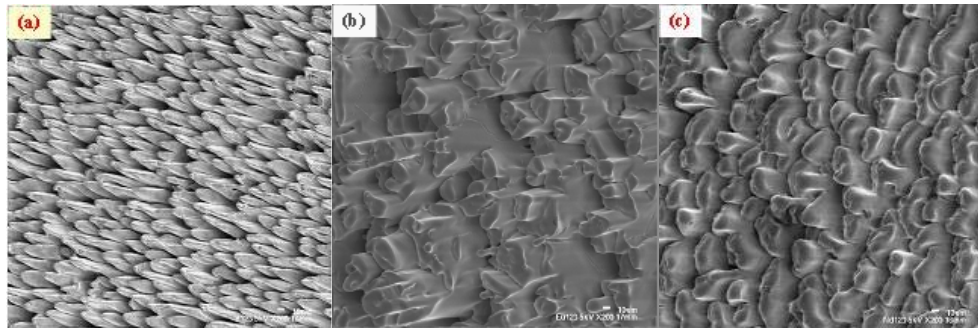
Fig. 56 Scanning electron micrographs of target surface of (a) Y123, (b) Eu123, and (c) Nd123 after long enough laser irradiation.

It should be noted that the micrographs were taken after the target surface was fully modified by the laser irradiation with a long cumulative exposure. As can be seen in Fig. 56 (b) and (c), the Eu123 or Nd123 target surfaces are covered by "mesas" after the laser irradiation instead of "cones". Although the specific reasons for the enhanced deposition rate of RE123, relative to Y123, is not fully understood, a higher deposition rate is potentially possible since the relatively large and flat "mesa" surface makes the fluence dilution much less compared to the porous-like "cones" of a Y123 target.

Depending on the RE123 materials, the processing parameters can significantly affect the superconducting properties of the RE123 films. Unlike large ion radius RE123 materials such as Nd123, Sm123, and Eu123 where the processing window for high performance is relatively small, the processing window to deposit small ion radius RE123 is relatively large. For example, a higher substrate temperature is generally required to obtain high J_c for Eu123 and Sm123 films. In addition, the substrate material also strongly affects the performance of the films. In contrast, oxygen pressure and the substrate temperature do not play significant roles for good quality films of small ion radius RE123. Figure 57 shows transition temperature (T_c) and the critical current density (J_c) at self-field for films deposited at different temperatures. As can be seen from this figure, both the T_c and the J_c of Dy123 are not so sensitive to the substrate temperature. It should be also pointed out that the T_c and the J_c are not sensitive to the oxygen pressure either. Superconducting properties of Dy123 films are essentially the same for oxygen pressure from 50 mTorr to 300 mTorr. This feature is important for scale-up process or fabrication of long-length conductors since the fluctuation of processing parameters is unavoidable in the production line.
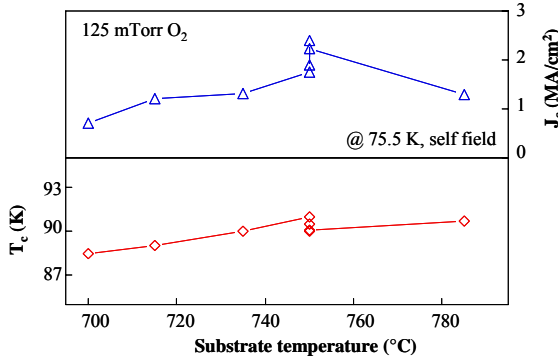
Fig. 57 Effect of substrate temperature on the superconducting properties of Dy123 films deposited by pulsed laser deposition.

We have characterized the field-angle dependent critical current densities of several RE123 films to investigate the flux pinning properties. In the field-angle dependent measurement, the current is always perpendicular to the field direction while varying the angle (θ) between the magnetic field and the c axis of the film. As can be seen from Fig. 58, Y123, Eu123, and Yb123 films all show an intrinsic peak at **H**||*ab*, as expected. It has been suggested that the peak in J_c for **H**||*ab* is produced by both the non-superconducting planes present in RE123 structure, which act as a periodic pinning structure, and by extended defects also parallel to the *ab*-planes but randomly distributed. The difference among these films (given the similar film thicknesses around 150 nm) is most dramatic for Eu123 in J_c for **H**||*c*. This peak has been observed for Sm123 films with a similar thickness. We have also observed that Dy123 films present an asymmetric angular dependence. The J_c peak at **H**||c has been attributed to correlated defects, such as twin

boundaries, screw and edge dislocations, and other defects such as those introduced by nano-particles.
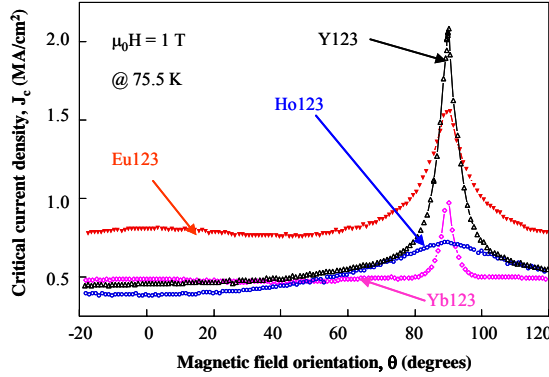
Fig. 58a Angular dependence of critical current density for Y123, Eu123, Ho123, and Yb123 at 1 T.
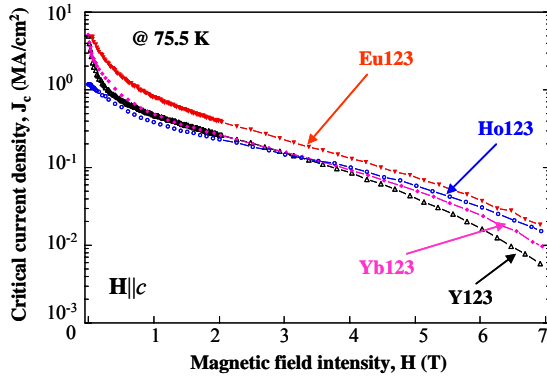
Fig. 58b. Field-dependent critical current density of the Y123, Eu123, Ho123, and Yb123 films. These films have similar thicknesses and transition temperatures.

Based on an Arrhenius plot, after 10 min @ 850°C, 6×10^{15} Cr atoms/cm^2 will be on the surface of a 50 nm thick Al_2O_3 film ($\simeq$ 8 ppm Cr in a 1 μm thick YBCO film). Some considerations must be taken into account to use of the diffusion coefficient data. Diffusion is a function of the source (element concentrations at the substrate film interface), film microstructure, temperature, etc. For a stainless steel substrate, Fe may also play a role as one of the diffusing elements.

The comparison of field-dependent J_c of Y123, Eu123, Ho123, and Yb123 is shown in Fig. 5. In comparison with Y123, the critical current of the RE123 films holds up quite well even at 7 T. Interestingly, Ho123 shows a higher J_c at 7 T even though its zero field J_c is 4 times lower than that of Y123. It should be pointed out that a sharp drop in critical current in the low field (< 0.1 T) region has been observed for Y123 when H∥c, while a smaller decrease in critical current appears for Eu123, Ho123, and Yb123 at the lower field. The dramatic decrease in current at low magnetic field in thin Y123 has been attributed to the absence of strong coherent pinning centers for flux lines oriented along the c axis. It is obvious from Fig. 58b that Eu123, Ho123, and Yb123 have more coherent pinning strength in this direction than Y123 at both low and high fields. It should be noted that the T_cs of RE123 films are not responsible for the enhanced J_c at the higher field since all the films have a T_c of around 90 K.

To summarize, under the given processing conditions, we have found that the deposition rate changes in a wide range depending on RE123 materials. The larger the RE ion radius is, the higher the growth rate. Investigation of the target surface reveals that the RE123 target surface is covered by "mesas" after laser irradiation instead of "cones," which are the typical case for Y123. To deposit good quality superconducting films, small ion radius RE123 materials are more forgiving to the processing conditions. On the other hand, the large ion radius RE123 materials exhibit more pinning strength, given a film thickness in the range of 150 nm, which is the case here.

[From Q.X. Jia, et al., IEEE Trans. Appl. Supercond. **15**, 2723 (2005)]

53

2.1.5 Development of High I_c Ex Situ Processed YBCO Coated Conductors

(Oak Ridge National Laboratory): R. Feenstra, D. K. Christen, A. A. Gapud, E. D. Specht, F. A. List, T. Aytug, A. Ijaduola, J. R. Thompson, S. Cook, (LANL) T. G. Holesinger, P. N. Arendt, S.P. Foltyn, R. F. DePaula, J. A. Kennison, (University of Wisconsin, Madison): D. M. Feldmann, X. Song, A. Gurevich, D. C. Larbalestier

The purpose of this work is to advance a materials science background for *ex situ* processing of high-performance ReBCO coated conductors with a long-term goal to increase I_c to 1000 A/cm at 77 K, enable broad implementation of CCs, and reduce cost/performance ratio: \$/kA-m. Some of the long-term objectives are to develop an understanding of the fundamental epitaxial growth mechanisms of the *ex situ* BaF_2 process, of the connectivity and the thickness dependence of J_c and of the origin of flux pinning in high J_c ReBCO coated conductors.

Several significant advancements in understanding *ex situ* YBCO film development have been made recently. We have increased our understanding of liquid phase development, laminar growth, and high-J_c structures, of grain boundary meandering and grain boundary overgrowth, and of fast processing (> 10 /s) of ex-situ YBCO films. Current levels of performance are now 400 A/cm-w (J_c= 3.3 -2.4 MA/cm^2) with film thickness 1.2-1.7 µm on an AMSC RABiTS™ template. The main LANL contribution to this effort has been an understanding of liquid phase formation, laminar growth, and the microstructural development of high-J_c *ex situ* films.

A microstructural summary is presented of a bi-modal structure in PVD-BaF_2 *ex situ* films that forms under a certain set of standard processing conditions, the causes for its formation, and variants of this structure and their relationship to the performance level of the films. The amount of liquid phase formation and porosity during processing plays a pivotal role in determining the microstructural uniformity, second phase assemblages, grain boundary structures, and ultimately the resulting performance levels. Based on these insights, new processing routes have been developed that have allowed for faster conversions, uniform microstructures, and higher performance.

The "standard" conversion of PVD-BaF_2 YBCO films produces high-J_c films with a bi-modal microstructure. This bi-modal structure consists of large, well formed, YBCO grains in the bottom half of the film and smaller, faulted YBCO grains in the top half (Fig. 59). This structure indicates two different growth modes. Some of the distinguishing microstructural features are the laminar growth mode, $Ba_2Cu_3O_y$ or Ba-O-F second phase layers, and large YBCO grains with layers of Y_2O_3 precipitates.

Fig. 59. TEM cross sectional images of ex situ processed YBCO films.
a and b: IBAD YSZ template (LANL)/CeO_2/BaF_2 YBCO (ORNL); J_c (77K) = 0.93 MA/cm^2/2.9 µm YBCO film/270 A/cm-w. c: RABiTS template with 5 µm BaF_2 YBCO film; J_c (77K) = 0.31 MA^2/ /155 A/cm-w. The arrow in b and c point to second phase layers.
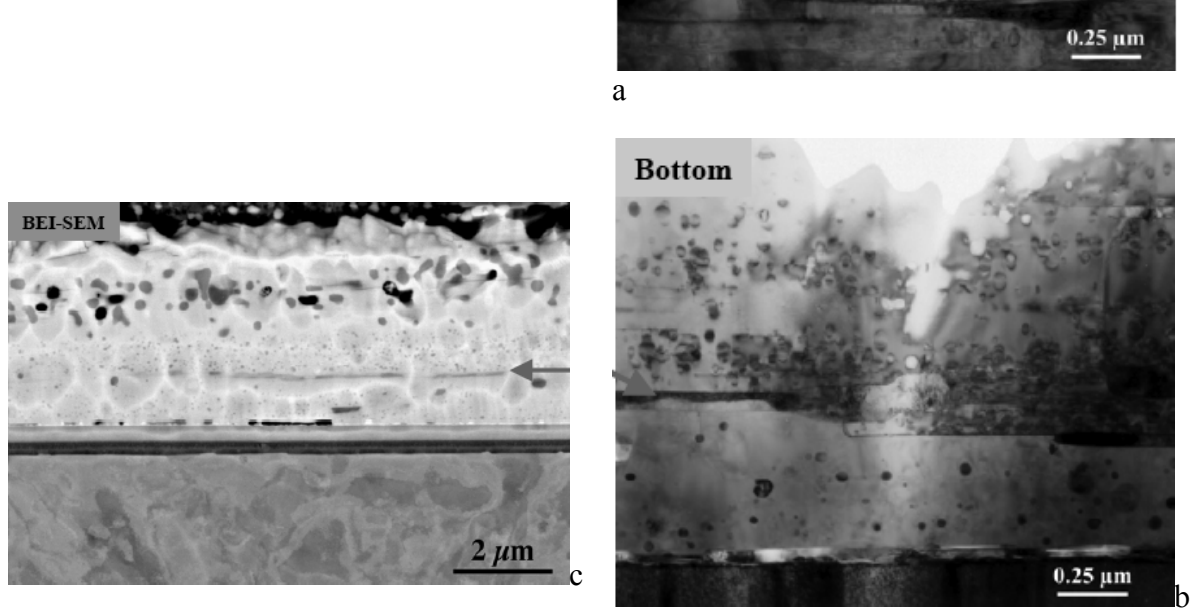
The bimodal structure shown in Fig. 59 is generated by several events that occur in the early stages of conversion. The first is that of CuO segregation. The second is that of excess liquid phase generation. During this process Y_2O_3 particles are floating in the Ba-O-F near growth front. The reaction (3) $YCuO_x$+ (2) Ba-O-F $\rightarrow$ $YBa_2Cu_3O_y$ + Y_2O_3 takes place, resulting in a layered Y_2O_3 structure within the large YBCO grains in the bottom half of the bimodal structure. Fig. 60 shows a 2.66 µm thick YBCO film on RABiTS quenched after 1.5 hours total processing time. The elemental maps show the segregation of phases and layering discussed above.

55
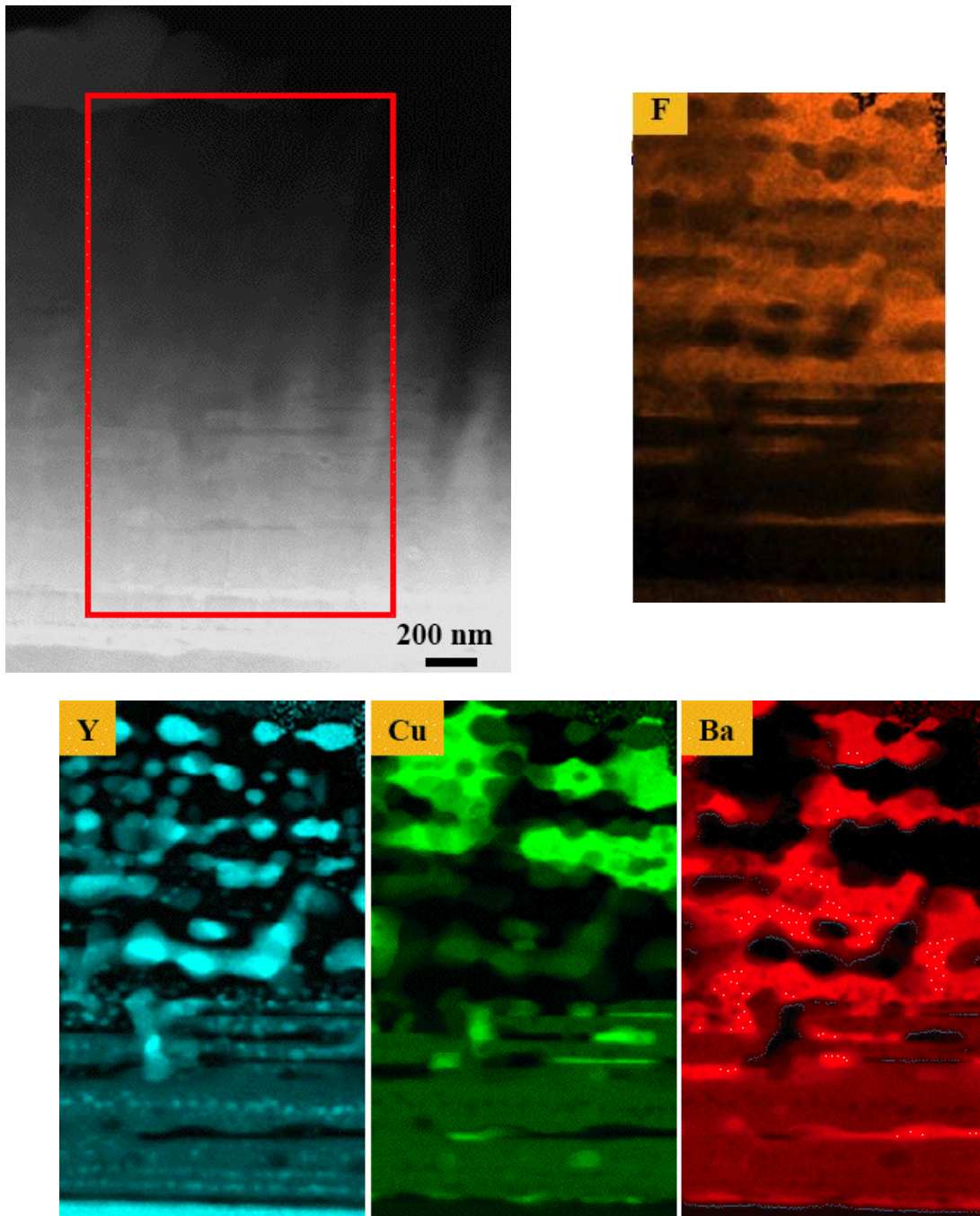
Fig. 60. Images of a 2.66 μm thick YBCO film on RABiTS quenched after 1.5 hours total processing time. The image at the upper left is a TEM image indicating the location of the elemental maps (for fluorine, yttrium, copper, and barium shown in the rest of the figure.

The laminar growth mode of the *ex situ* YBCO grains manifests itself in the structures seen above the RABiTS™ substrate grain boundaries. Fig. 61 shows a TEM cross sectional image of a fully processed film. The grain boundary in the substrate propagates through the substrate and buffers into the YBCO film. In the YBCO, it meanders around more than 1 μm laterally. This grain boundary meandering may have important ramifications for connectivity and J_c performance levels.
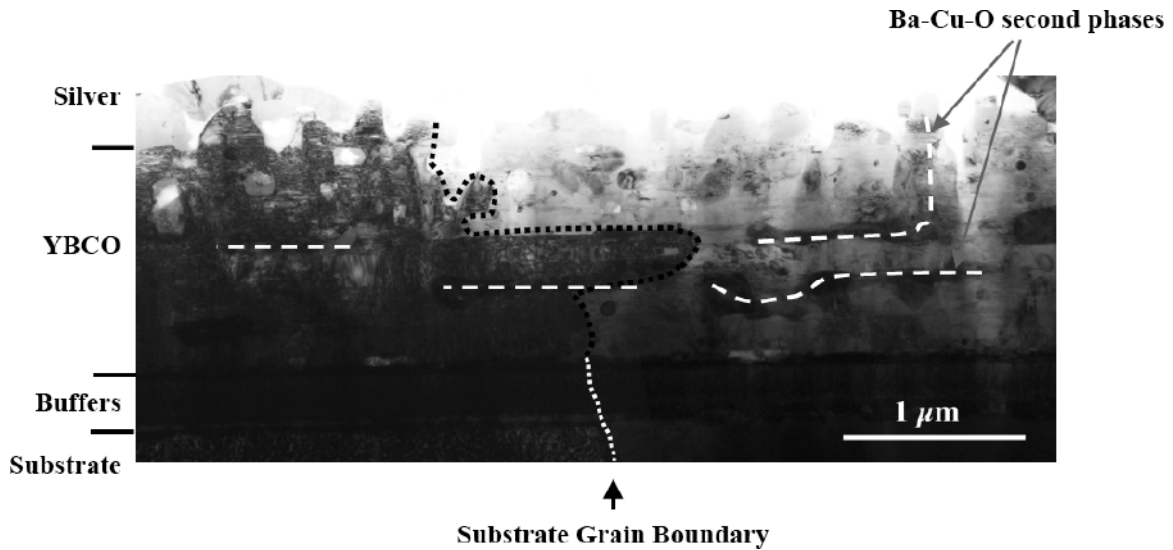
Fig. 61. TEM image of a substrate grain boundary meandering through a YBCO film on RABiTS.

Grain boundary meandering above substrate grain boundaries also occurs in YBCO films prepared by MOD, as indicated in Fig. 62.
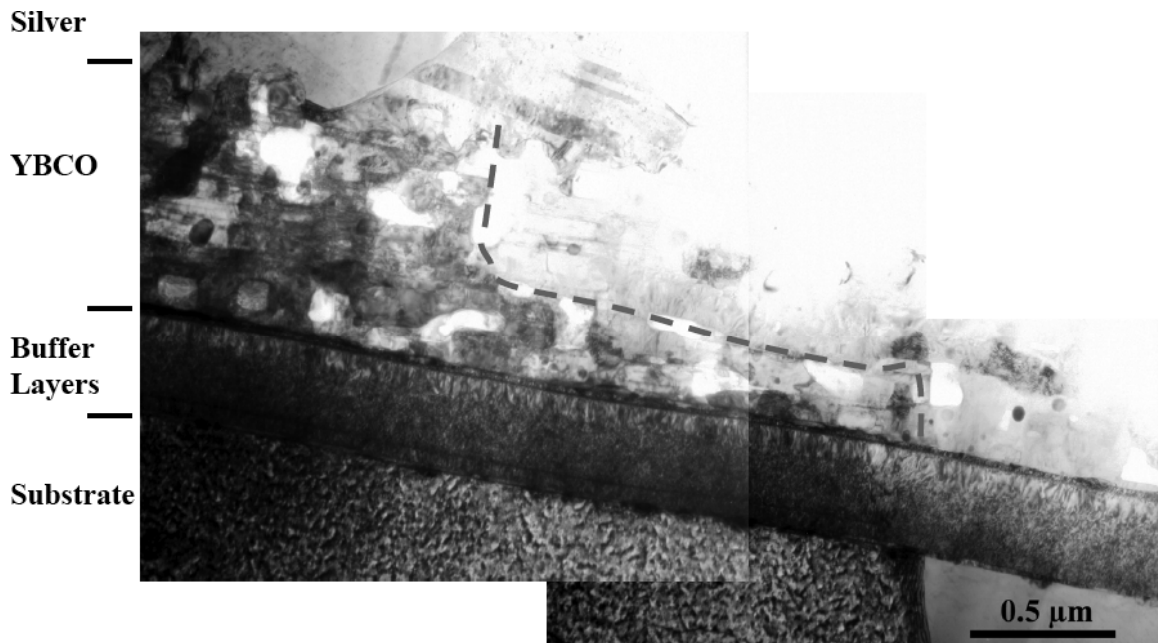
Fig. 62. TEM image of a substrate grain boundary in an MOD YBCO film.

Liquid phase assisted growth in the BaF_2 process films is evident from the large YBCO grains that can form as shown by EBSD (Fig. 63) and TEM. YBCO grains up to 50 μm in size were observed by EBSD and TEM, whereas the IBAD YSZ template has a grain size of ≈ 0.1 -0.25 μm.
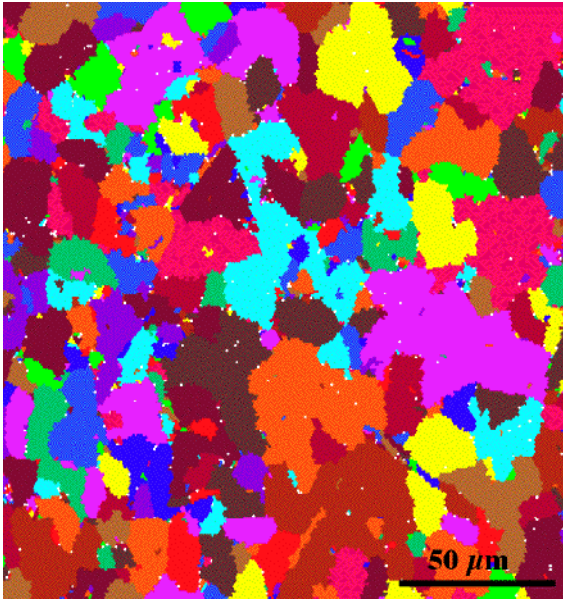
Fig. 63. EBSC image of IBAD YSZ (LANL) / CeO$_2$/ BaF$_2$YBCO (ORNL) J$_c$(77 K) = 0.93 MA/cm^2/ 2.9 μm YBCO film / 270 A/cm-w.

We have found that the YBCO films converted with the "standard" process (bi-modal structure) (Fig. 64) do not meet needed performance levels, therefore, there is a need to modify the processing conditions to increase J$_c$ to significantly greater than 1 MA/cm^2. Exceptions to the trend line (Fig. 64) were used as an opportunity to determine the direction to take for microstructure and performance optimization.
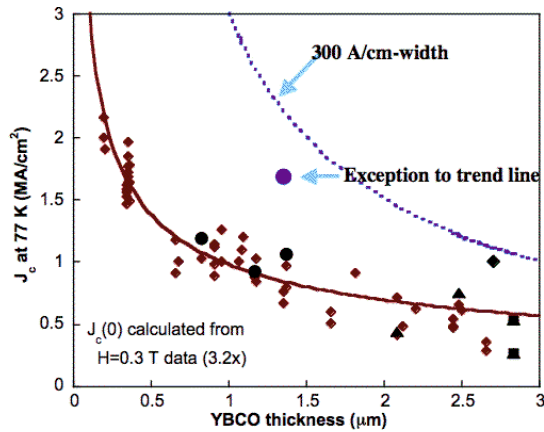
Fig. 64. Critical current density as a function of film thickness for BaF$_2$ "bimodal" process YBCO films showing exceptions and desired 300 A/cm-width performance level.

Exceptions to the J$_c$ trend line (Fig. 64) show variants of the bimodal structure, such as no second phase layers and reduced out-of-plane tilt. It appears that porosity plays a role in the development of high J$_c$ microstructures. A couple of examples illustrate this point. Fig. 65a is an example of a bimodal structure without second phase layers, and Fig. 65b shows a partial bimodal structure without second phase layers.

Fig. 65a. YBCO film with bimodal structure but no second phase layers. (1.4 μm thick, J_c = 1.69 MA/cm^2)

Porosity
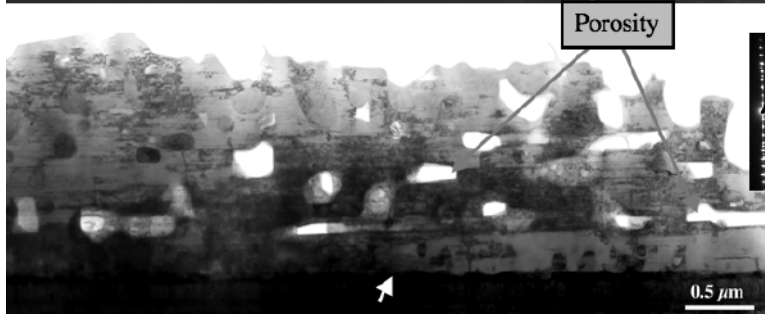
Fig. 65b. YBCO film with partial bimodal structure but no second phase layers. The white arrow points to the end of a large grain with precipitates. (1.8 μm thick, J_c = 0.9 MA/cm^2)

Each second phase layer in a bimodal structure has the potential for YBCO alignment degradation. This can be seen if Fig. 66 where it is clear that the YBCO grains change orientation when separated by the second phase layer.

YBCO
Ba$_2$Cu$_3$O$_y$
YBCO
Ba$_2$Cu$_3$O$_y$
YBCO (zone axis ∥ beam)
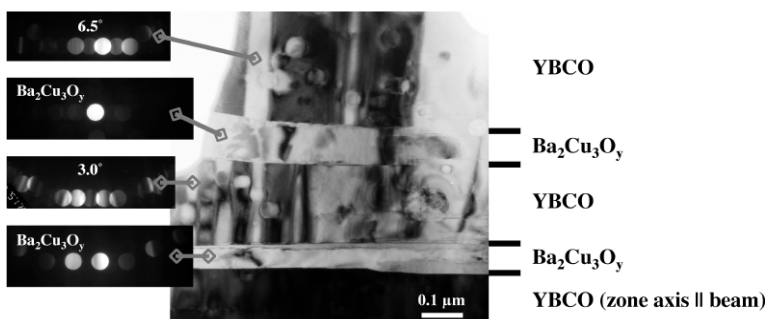
Fig. 66. TEM cross-section micrograph of BaF$_2$ YBCO film with second phase layers.

Modified processing has demonstrated a reduced out-of-plane misalignment for *ex situ* YBCO films of thicknesses greater than 1 μm as shown in Fig. 67. The XRD data is also consistent with the reduction or elimination of second phase layers in *ex situ* YBCO films made with the modified process.
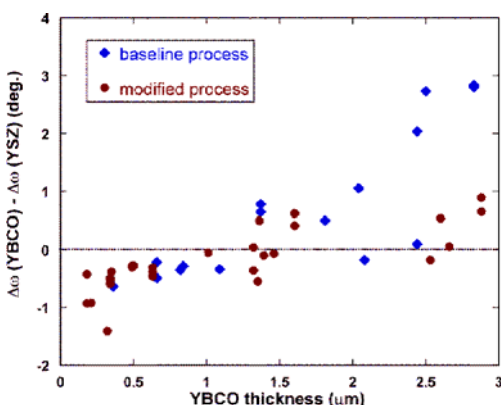
Fig. 67. Change in out of plane alignment from the YSZ layer to the YBCO layer as a function of YBCO film thickness.

59

A fast, modified process was developed to produce high-J_c, high-I_c films with a uniform, thru-thickness microstructure (Fig. 68). This has resulted in much higher performance levels, e.g., J_c= 2.7 MA/cm^2, I_c= 334 A/cm-w for t = 1.25 µm. The new process appears to modify liquid phase generation. There are no second phase layers but porosity is present. There is a uniform distribution of planar defects and secondary phases thru-thickness and minimized reactions with the CeO$_2$ layer.
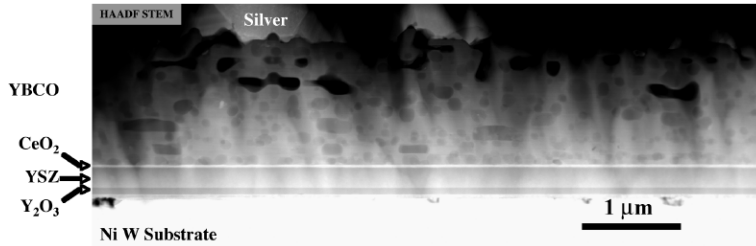
Fig. 68. TEM cross section image of a YBCO film produced uing the fast modified process.

High performance MOD BaF$_2$ YBCO *ex situ* films have a uniform, thru-thickness microstructure (Fig. 69) with a uniform distribution of secondary phases and planar defects. No second phase layers; porosity distributed thru thickness. Typical performance levels are I_c = 250 A/cm-w, J_c= 3.1 MA/cm^2 for a t = 0.8 µm film.
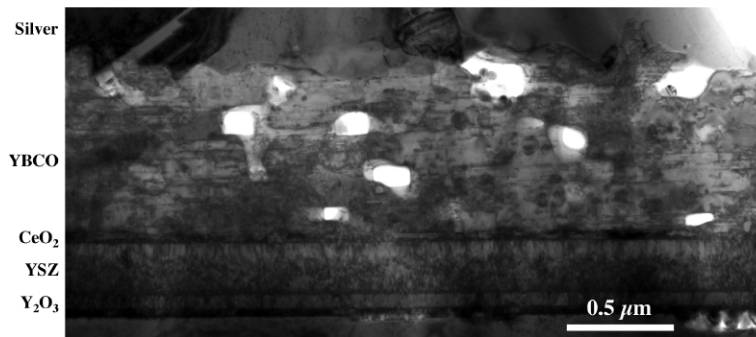
Fig. 69. TEM cross sectional image of MOD BaF$_2$ film.

In summary, we have developed an understanding of the causes and effects of the bimodal microstructure in ex situ BaF$_2$ YBCO films. Second phase layers were found to cause misalignments and reduce J_c. Variants of the bimodal structure without second phase layers allow for higher J_c values. A process for producing through-thickness uniform microstructure has been developed resulting in even higher J_c's. There are several unique characteristics of *ex situ* grown YBCO films. They are characterized by laminar growth and by the phenomenon of grain boundary meandering / grain boundary overgrowth. At present, it is believed that some porosity in the *ex situ* YBCO films is needed for material transport within the film during conversion, and that fully dense structures may trap liquid phases leading to detrimental second phase layers. On the other hand, samples processed by the new "fast-modified" process show uniform thru-thickness microstructures. They are characterized by a uniform distribution of planar defects and second phases and by reduced interfacial reactions with CeO$_2$. Finally, it was found that the microstructures of high-J_c MOD and PVD-BaF$_2$ films very similar.

60

2.1.6 Los Alamos Coated Conductor Development

V. Matias, B.J. Gibbons, S. Kreiskott, A.T. Findikoglu, P.C. Dowden, J.G. Storer, J.Y. Coulter, J. Sullard, C. Sheehan, G. Croes, S. Ashworth, T.G. Holesinger, P.N. Arendt, S. Foltyn, L. Civale, and B. Maiorov

Los Alamos initiated the Coated Conductor (CC) research in the US in 1994 and is accelerating the development of CC and supporting the industrial effort by developing cost-effective processes and high-performance wire. For this purpose an effort in continuous fabrication is required, coupled with state-of-the-art characterization facilities.

Ion beam assisted deposition (IBAD) of MgO is the best texturing process, and pulsed laser deposition (PLD) of YBCO is our choice for demonstration of CC. LANL has developed methods and technologies for fabricating and characterizing CC's, starting from the metal substrate, electropolishing, barrier and seed layer development, IBAD MgO, PLD buffers, Cu plating, to long length and ac loss characterization, and transferred many of these technologies to US industry.

In the past year, Los Alamos CC Continuous Processing has produces > 2 km of electropolished substrate, 400 m or IBAD MgO tape with the addition of ion scattering and a second RHEED for in situ diagnostics, 100 m of PLD YBCO tape and 200 A/cm results. The reactive coevaporation system is operational, and a significant increase in collaborations.

The Electropolishing System has been producing long lengths and on wider tapes. Excellent polishing results have been achieved on Hastelloy: 1 nm RMS roughness on 5 x 5 µm scale area with a (one cell) speed of 12 m/h. 100 µm and 50 µm thick 1-cm wide tapes are the standard ones to be polished; however, the system has been set up and has polished 3 cm-wide tapes (Fig. 70) and in the future, preparing to polish 6-cm wide tapes.
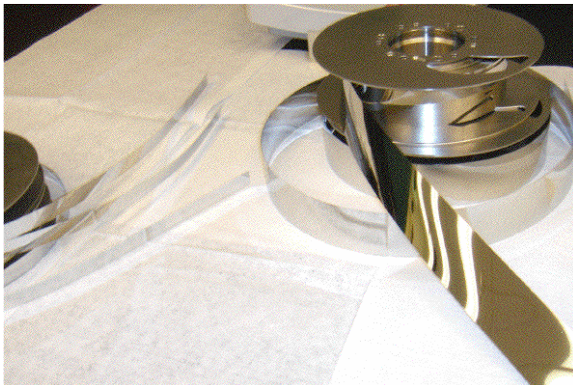
Fig. 70. Electropolished tape 1 cm and 3 cm wide.

The Electropolishing System is now serving needs of industrial efforts: Two years ago we demonstrated the utility of electropolishing, and within a year we transferred the technology to SuperPower for their manufacturing facility and they pursued further improvements. The system shown in Fig. 71 can polish tape at up to 42 m/h and yielded a surface finish Ra of < 1 nm over a 5 µm AFM line scan (measured at LANL).

Fig. 71. Electropolishing system set up and operating at SuperPower.

American Superconductor expressed an interest in electropolishing RABiTS precursor tape for cleaning purposes, and we successfully polished long lengths of RABiTS precursor Ni-5%W tape for AMSC this year. NiW tape is purchased from a vendor at 0.2 mm thickness and has variable surface contaminants, metal and oxide particles, and a relatively rough surface (Fig. 72a) such that surface cleaning before further rolling is essential. After electropolishing, Fig. 72b, the surface is markedly smoother. Fig. 73a shows this strip after final rolling to 0.06 mm thickness; it is clean and smooth with a surface finish Ra of 12 nm. After the final texture anneal, Fig. 73b, the surface is clean with a surface finish Ra of <0.2 nm inside the grains.

Before R_a = 122 nm   After R_a = 90 nm
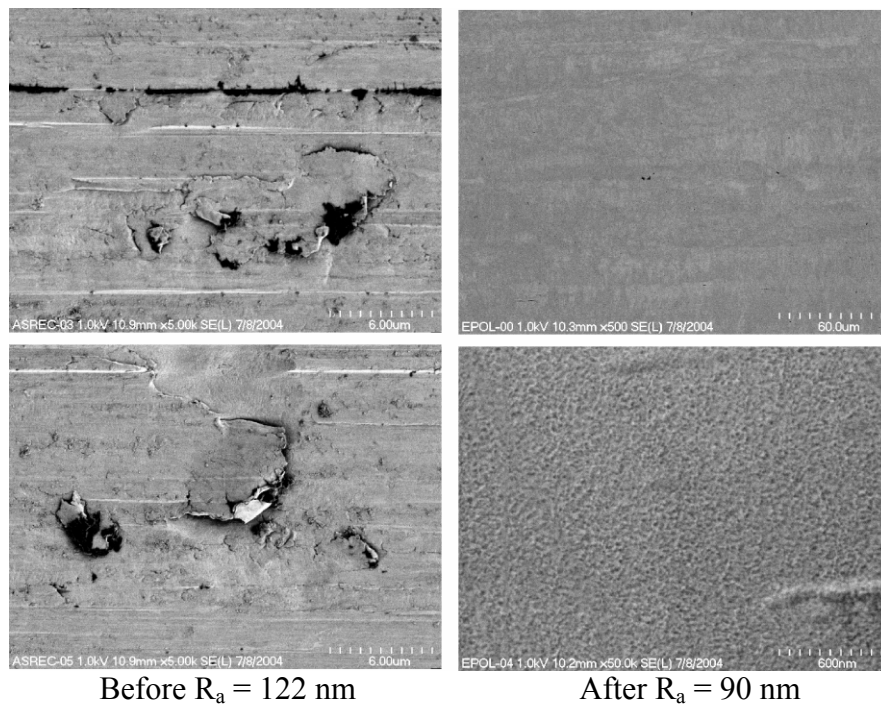
Fig. 72a. As rolled 0.2 mm thick NiW strip.   Fig. 72b. The strip of Fig. 72a after electropolishing.
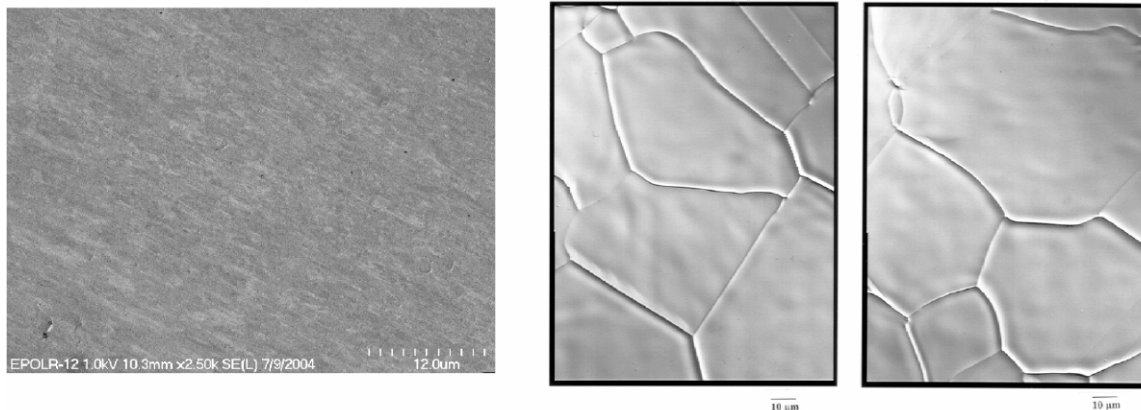
Fig. 73a. Surface finish after e-polishing strip and   Fig. 73b. Substrate of Fig. 4a after texture anneal.
rolling to 0.06 mm substrate thickness.

The LANL Coated Conductor geometry is shown in Fig. 74. The IBAD-textured MgO template on the Ni-superalloy is deposited by e-beam evaporation. The buffers and superconductor layer are produced by pulsed-laser deposition (PLD). Different layers are needed for different functionalities. The barrier layer prevents interdiffusion of substrate constituents into the MgO, and uses (amorphous) a-Al_2O_3 with an ion beam assist for densifying. The nucleation layer is needed for the IBAD-MgO process and uses a very thin (~5 nm) of Y_2O_3. IBAD-MgO provides the in-plane texture, and a homoepitaxial MgO layer relieves the strain in the MgO. The epitaxial buffer layer, typically a perovskite, provides a good lattice match to YBCO and improves the in-plane texture significantly.

Ag layer
YBCO
Epi buffer layer(s)
IBAD-MgO layer
Nucleation layer (Y_2O_3) + barrier layer (Al_2O_3)
Hastelloy
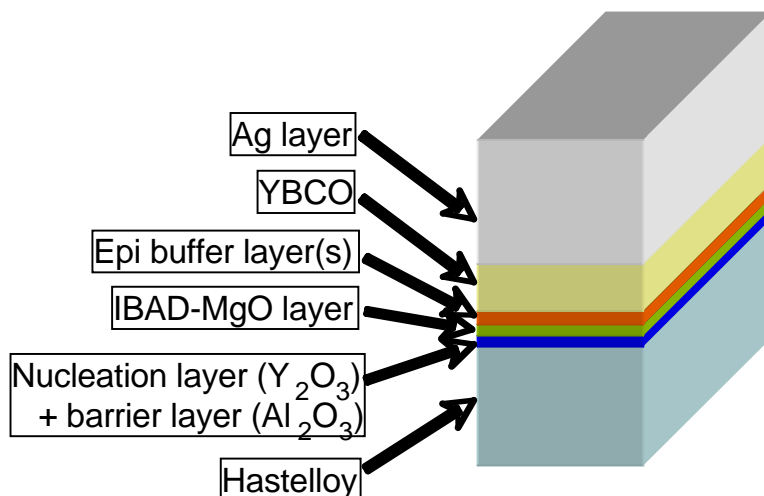
Fig. 74. Schematic of YBCO coated conductor architecture.

A good barrier layer prevents diffusion of metal species from the substrate going into the IBAD template layer. The LANL program developed and effectively used a thin (80 nm) layer of a-Al_2O_3 to serve as the barrier. Its effectiveness is evident from the results shown in Fig. 75, in which an unprotected IBAD template is destroyed by diffusion after heating.
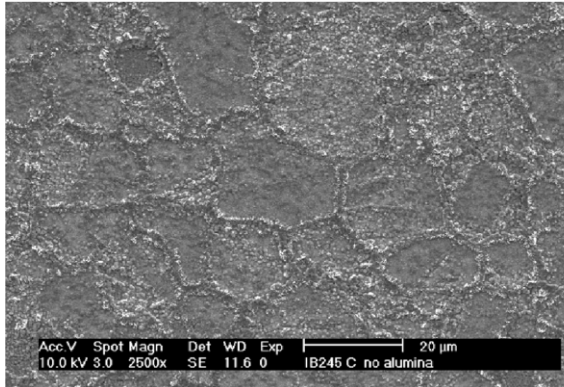
Fig. 75a. IBAD template with no aluminum oxide barrier after heating to 920°C.
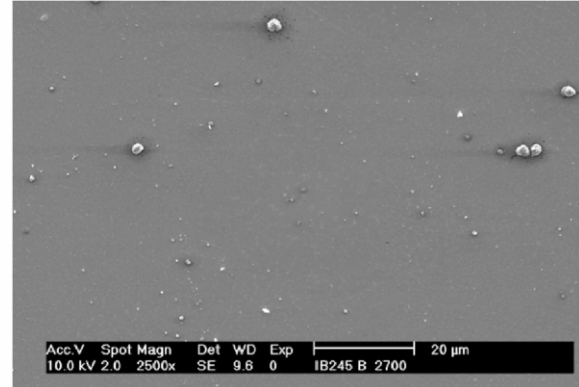
Fig. 75b. IBAD template with an aluminum oxide barrier after heating to 920°C.

An Ion Scattering Spectrometry has been added to the IBAD system for in situ diagnostics. Time-of-flight ion scattering spectroscopy (ISS), recoil spectroscopy (DRS), and reflectron mass spectrometer (MSRI) are all included in this package, Fig. 76a. The MSRI is similar to SIMS but is capable of high-resolution surface analysis at higher ambient pressures. These instruments allow for real-time, non-destructive *in-situ* analysis of the film growth process.

ISS was used to analyze metallic species diffusing from the Hastelloy substrate and through the barrier layer. The tests were done by heating the specimen in oxygen for 5 minutes at various temperatures with the results shown in Fig. 76b. It was found that fully oxygenated alumina improves as barrier
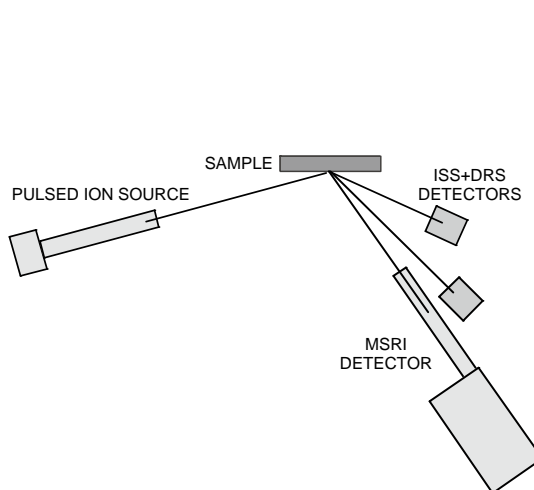
Fig. 76a. Schematic of the new detector systems.
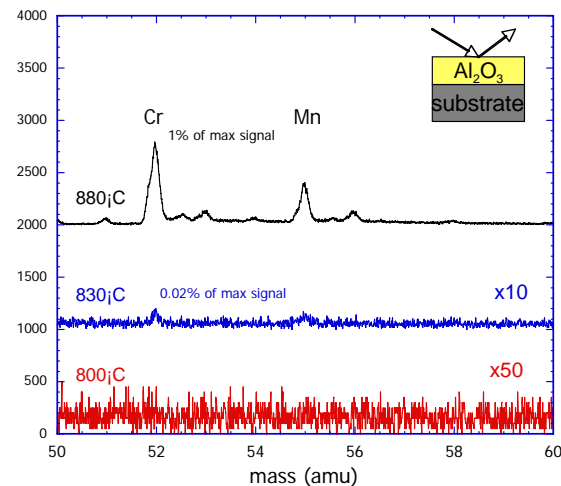
Fig. 76b. ISS measurement of diffusion through the alumina barrier.

The IBAD-MgO prepared by e-beam deposition is very stable. The best samples made exhibit FWHM in-plane < 4°. Longer lengths have been fabricated with in-plane texture of 6–8°. Multiple 10-15 meter pieces have been made at thicknesses of 100 μm and 50 μm (4-mil and 2-mil).

Previous results indicated the importance of the ion-to-molecule ratio during IBAD texturing. The in-plane and out-of-plane texture improves as the ion-to-molecule ratio, *r*

64

increases, and the accessible range of ratios depends on the nucleation surface; on alumina, the texture was typically not as good (1–2° worse in-plane) (Fig. 77).
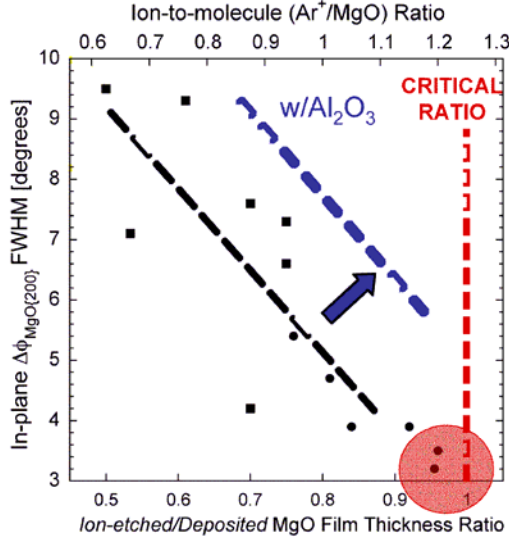
Fig. 77. Dependence of texture on ion-to-molecule ratio.

IBAD a-Al$_2$O$_3$ worked well as a barrier layer at thicknesses of 60–80 nm; with demonstrated I$_c$ in YBCO up to 200 A. We made about 400 meters of IBAD (~ 100 runs) in the last year, but the results were not always repeatable nor as good as we would like. We would sometimes get polycrystalline rings in the RHEED and reduced intensity in the XRD, depending on the condition of the alumina. The alumina barrier has two drawbacks: slightly poorer texture and occasionally worse crystalline fraction in IBAD-MgO.

We find that the IBAD-MgO texture depends on ratio *and* total deposit thickness. The results in Fig. 78a show that the process is more robust at higher ratios. The texture curves exhibit scaling, and the details depend on the growth surface. Fig. 78b shows that data rescaled to the deposit thickness. The curves are for flat deposition profiles. The texture can probably be improved, but this will require more research.
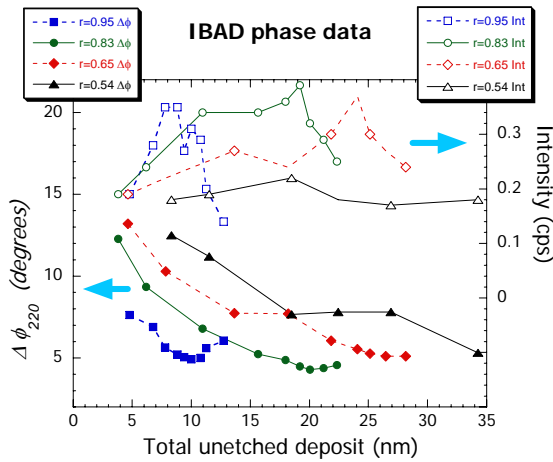
Fig. 78a. MgO texture and intensity as a function of total unetched deposit thickness.
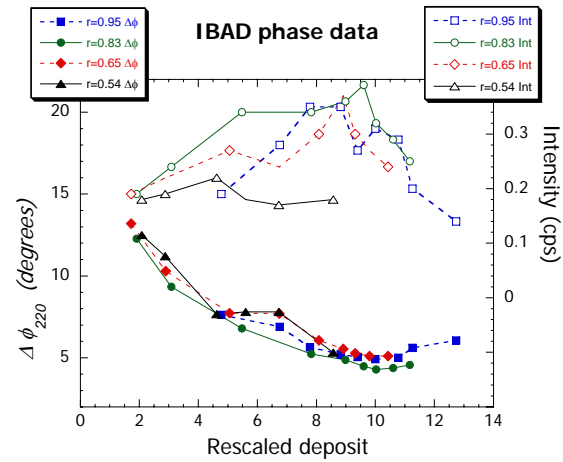
Fig. 78b. MgO texture and intensity as a function of rescaled deposit thickness.

The deposition of IBAD-MgO has been demonstrated at a speed of 3 cm/sec or 100 m/hr; this is orders of magnitude faster than competing IBAD technologies, as seen in Fig. 79. The speed is limited by the ion gun used. We can extrapolate to 5x wider tape yielding 500 m/hour of cm-equivalent tape with the same ion gun. Three ion guns could be placed in series to increase the throughput to 1.5 km/hour of cm-equivalent tape. (For a high-throughput manufacturing processes for CC, speeds of ~1 km/h are required.) Table I shows the status of various parts of the CC fabrication process at present and what could reasonably be extrapolated. As can be seen, some of the rate-limiting steps are the barrier (Al_2O_3), lattice matching buffer, and YBCO layers.
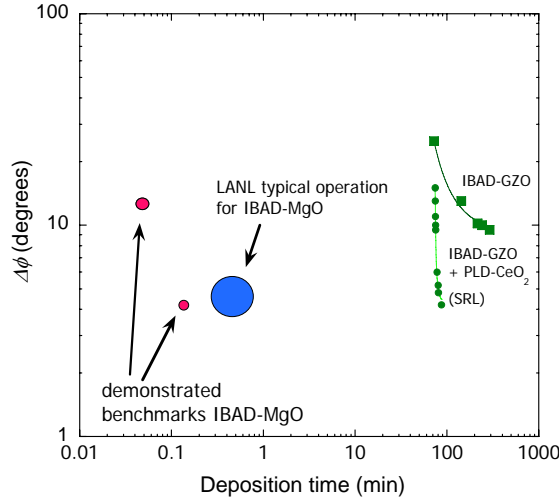
Fig. 79. IBAD template layer texture as a function of deposition time.

Table 1. Throughput of Coated Conductor Fabrication Process

	Electro-polishing	Barrier layer (AlO)	Nucleation Layer (YO)	IBAD-MgO	Epi-MgO	Buffer layer (LMO)	YBCO (PVD)	Normal metal (Ag/Cu)
Demonstrated speed cm-m/hr	36	4	15	100	10	20	15	-
Capable speed cm-m/hr	150	20	150	500	100	?	?	5
Status	4	?	4□	4□	4□	?	?	4□

The next stage in the production process of coated conductors is the use of pulsed laser deposition (PLD) to deposit the buffer layer and YBCO layer, Fig. 80a. We use a reel-to-reel PLD system for long length depositions. The system (Fig. 80b) uses a XeCl (308 nm) excimer laser and has four targets for deposition of a variety of oxide layers. It has a quartz lamp heater and in situ adjustment of the tape position with respect to the laser plume. This chamber also has a sputter gun to deposit the Ag layer over the YBCO.
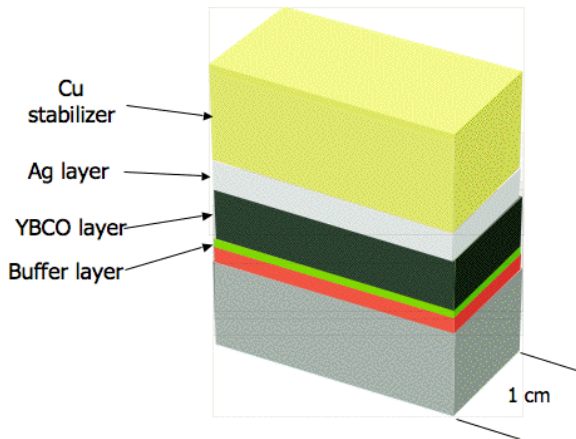
Fig. 80a. Layer stacking sequence of the coated conductor.
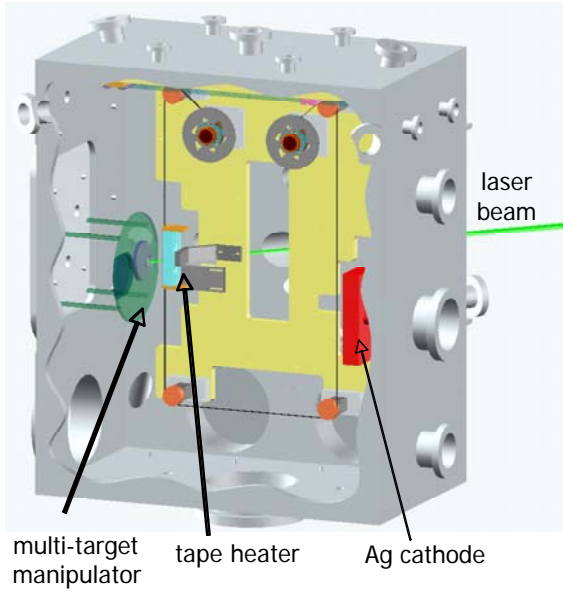
Fig. 80b. Schematic of the pulsed laser deposition chamber.

Significant progress has been made over the past year; previously our best results on 2 μm YBCO/50 nm LMO/IBAD template/Hastelloy were 178 A across 1 cm, 120 A across 10 - 20 cm, 50 A across 1.1 m, and microbridges – 1.1 MA/cm^2; reasonable results, but not up to the potential of the systems used. Reviewing the important factors for high quality PLD-deposited layers, these are a uniform, dense microstructure, reproducibility from run to run, uniformity over long lengths, high speed, and high I_c, and J_c.

Currently we are using LaMnO$_3$ and SrTiO$_3$ for our PLD-deposited buffer layer. The LaMnO$_3$ (LMO) buffer layer is a pseudo-cubic perovskite (110 spacing = 0.3985 nm) that allows a low deposition temperature, has a wide temperature window, a high deposition rate (0.1 nm/pulse), and can be deposited at up to 21 m/h. Fig. 81a shows the LMO crystal structure and Fig. 81b shows its epitaxial growth on the MgO layer. Fig. 82 shows several TEM images indicating a clean interface between the LMO layer and the underlying epi-MgO template layer.
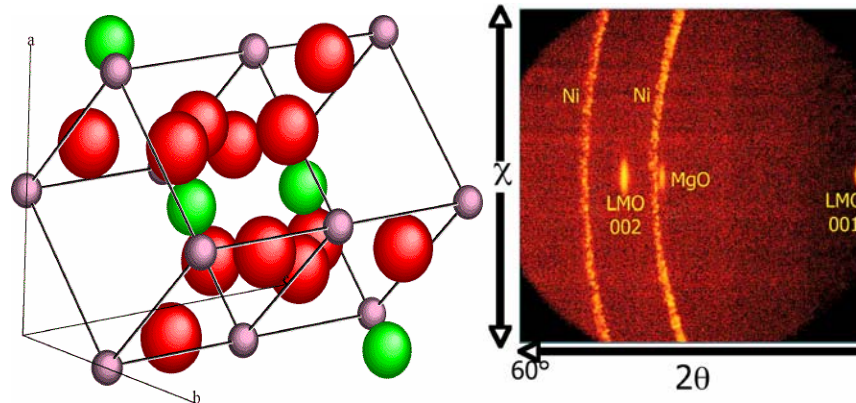
Fig. 81a. Crystal structure of LaMnO$_3$.

Fig. 81b. Bruker GADDS system showing epitaxial growth on the MgO and biaxial orientation of the LMO layer.
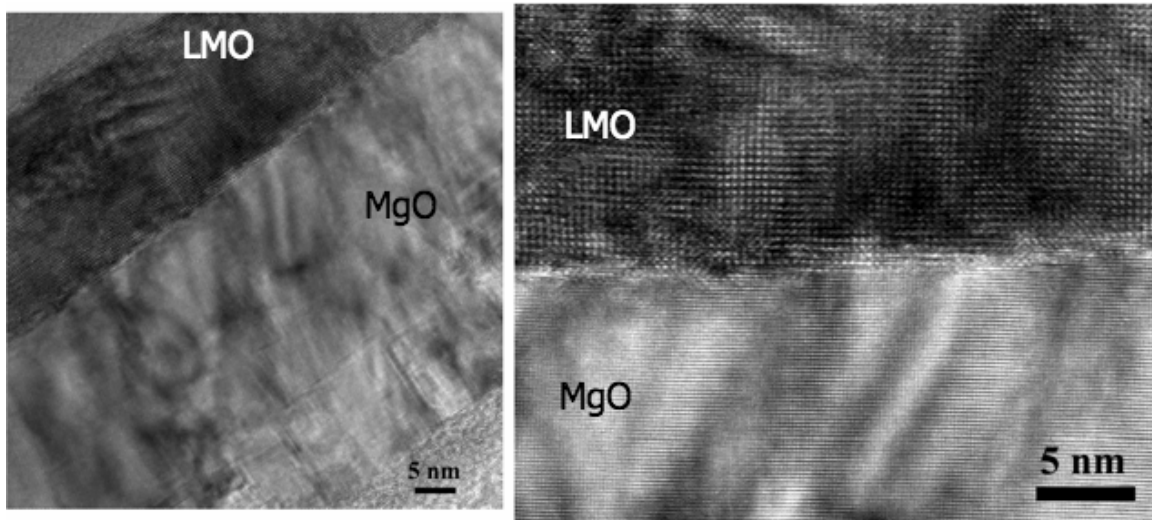
Fig. 82. TEM images showing the clean LMO/MgO interface.

Structural characterization (Fig. 83) indicates good c-axis texture throughout the stack. We typically deposit the LMO at 13.5 m/h in 200 mTorr of O_2 at a 15 Hz pulse rate for a 50 nm film. The YBCO is deposited at 1.8 to 2.7 m/h in 180-200 mTorr of O_2 at an 80-200 Hz pulse rate for a film 1 to 2 μm thick.
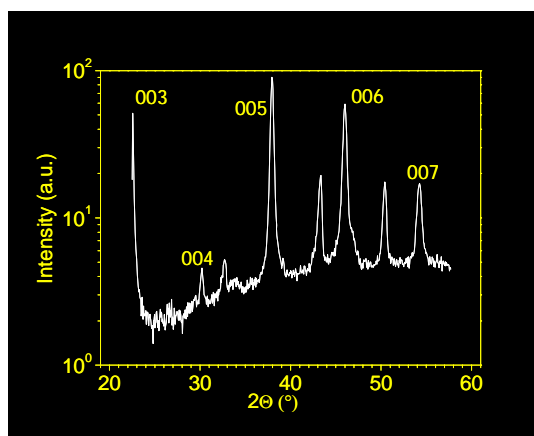
Fig. 83a. X-ray spectra showing YBCO 00*l* peaks.
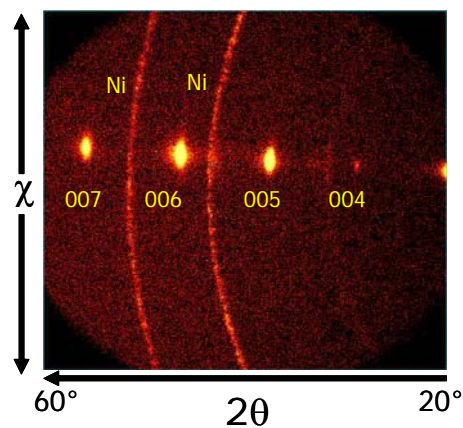
Fig. 83b. Bruker GADDS system showing c-axis alignment of YBCO.

Texture measurements by x-ray diffraction indicate comparable values for continuous deposition as compared to short samples prepared by paste-up. Typical results for the the layers for the 50 nm LMO layer are φ-FWHM ~ 5 − 6°, and for a 1.5 μm YBCO layer (Fig. 84) are φ-FWHM ~ 2.5 − 3.5°, and (out of plane) Ω-FWHM ~ 1.1 − 1.4°.
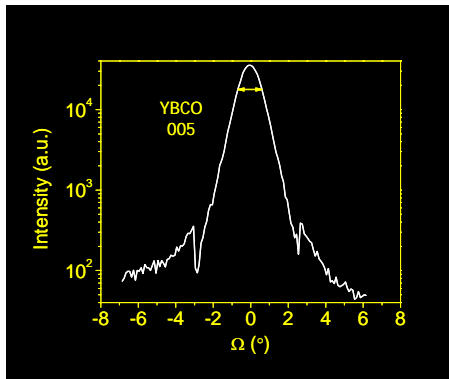
Fig. 84a. X-ray diffraction omega scan of the YBCO 005 line indicating good out of plane (c-axis) alignment.
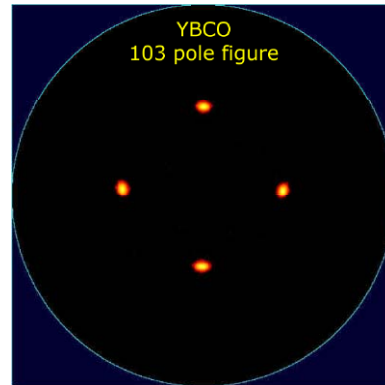
Fig. 84b. X-ray pole figure of YBCO 103 line showing good in plane orientation.

TEM shows the typical columnar microstructure for PLD-deposited YBCO films. Fig. 85 shows the cross sectional image of a film with a J_c of 1.9 MA/cm^2.
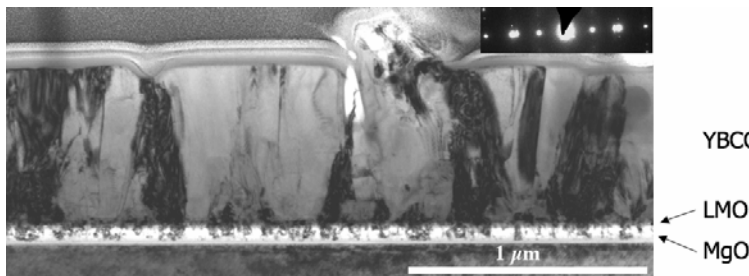
Fig. 85. TEM cross-sectional image of YBCO film.

It is very efficient to use continuous tape processing for exploring process parameters, for instance two different buffer layers on IBAD MgO, in a sequential way. Positions on a tape can be tracked from one process to the next to develop a matrix of experiments for optimization. To be useful, it is necessary to measure I_c in a continuous fashion. A continuous measurement system, Fig. 86a, uses a measurement (gauge) length of 5 cm and a step size of 2 cm. This latter can be decreased to < 1 mm in a region of interest, if required. In the figure, the two reels in the foreground are the feed and take up reels, the two in the background transport the tape and feed current through the tape, and the measuement stage is in the center with tape passing through. Using this combinatorial process, a 6 m long tape was profiled as a function of heater temperature and oxygen pressure with the results shown in Fig. 86b. These indicate that the optimum process parameters were 900 - 920°C heater temperature and 180 – 200 mTorr oxygen pressure.
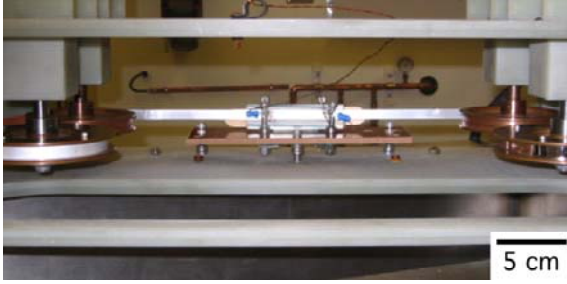
Fig. 86a. Continuous critical current measurement system.
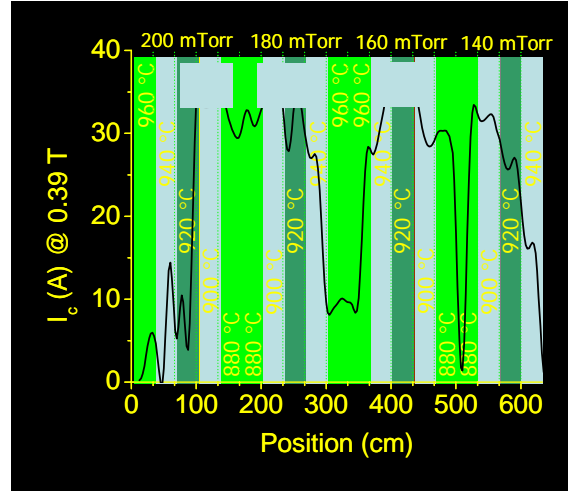
Fig. 86b. Critical current as a function of position with heater temperature and oxygen pressure as implicit parameters.

The best long length results to date were achieved on a 6 m IBAD-MgO-based coated conductor and are shown in Fig. 87. Over 1.6 m, I_c = 144 A/cm (±11%); over 3.75 m, I_c = 109 A (±20%); and over the entire 6 m, I_c = 44 A.
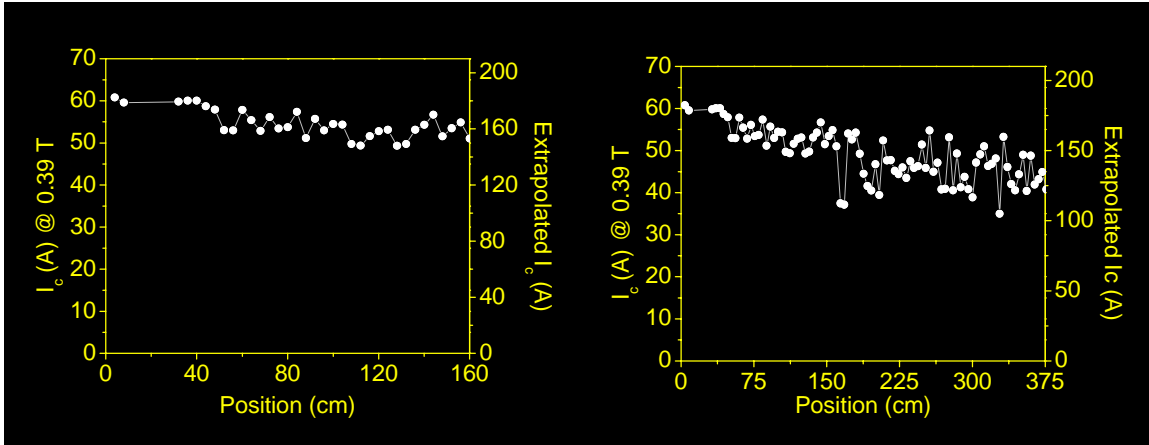
Fig. 87. Critical current at 0.39 T (and extrapolated self field values) as a function of position for the high current part of a 6 m long coated conductor.

Although the results were promising, the significant non-uniformity was not acceptable. Some of the reasons for this were considered.

Plume instability is associated with an unstable target raster mechanism. The use of a rotary magnetic feedthrough resulted in positional instabilities. This has been solved with a ferrofluidic feedthrough to a chain drive for the raster.

Heating the substrate is another potential problem area. The original heater (Fig. 88a.) used 4 lamps axial to the tape heating a Haynes[®] 214 v-shaped susceptor plate. The (recently installed) new heater (Fig. 88b) has 9 separately controlled zones, uses a quartz or Haynes[®] 214 susceptor plate, has the lamps are perpendicular to tape, and is designed for more uniform heating across the tape. This zonal heating system is important because

of the change in emissivity of a growing film results in a drop in the surface temperature at a critical thickness. This temperature decrease results in a change in the orientation of the film from c axis to a axis at the critical thickness, and a drastic decrease in J_c. By designing a temperature profile to account for this change in emissivity, it should be possible to better control the film microstructure.
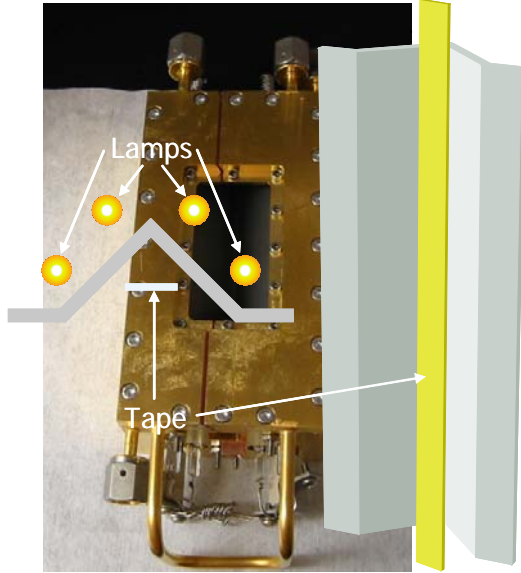
Fig. 88a. Original four lamp heater.
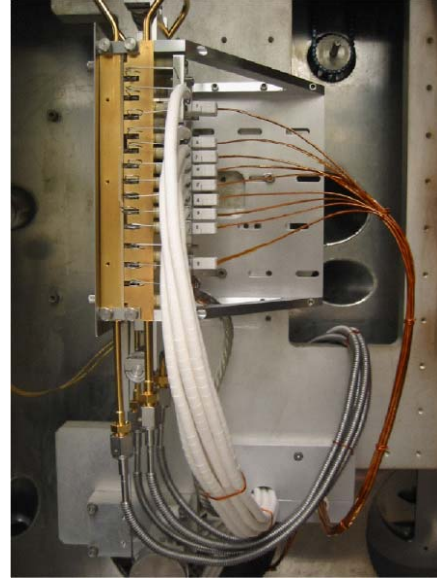
Fig. 88b. New nine lamp zone heater.

To begin, the temperature of the substrate is measured under two conditions, shown in Fig. 89a. It is clear that the substrate temperature begins to decrease when the sample thickness reaches about 0.7 μm; the emissivity has started to decrease at this thickness. By accounting for this, we hope to make higher quality thicker films with higher J_c's. The thermal profile for the heater that was designed to keep the substrate temperature constant across the deposition window is shown in Fig. 89b.
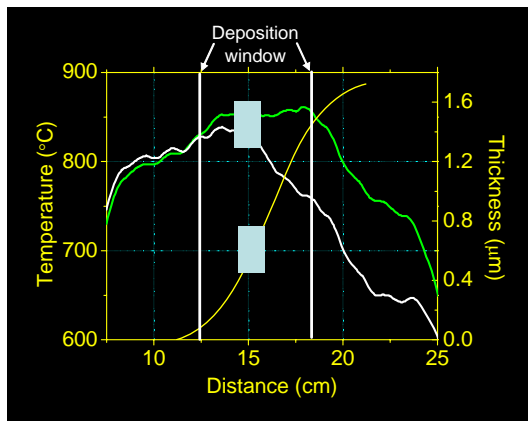
Fig. 89a. Temperature as a function of distance in the substrate heater.
The coral curve is a profile with the no laser plume (uncoated substrate), the white curve is with the plume (during coating), and the yellow curve shows the film thickness.
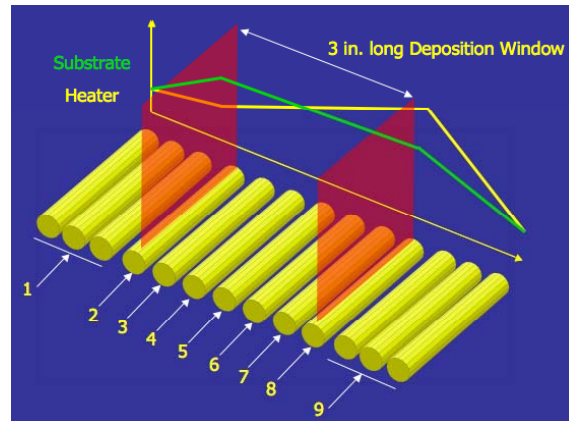
Fig. 89b. Thermal profile of substrate heater and substrate across the deposition zone.

With the engineered heating profile, a 2 μm thick film was deposited at 200 Hz and 1.8 m/h. It had a very good (in-plane) FWHM of φ of 3.65°, no evidence of a-axis growth Fig. 90a, b) and minimal 103 component.
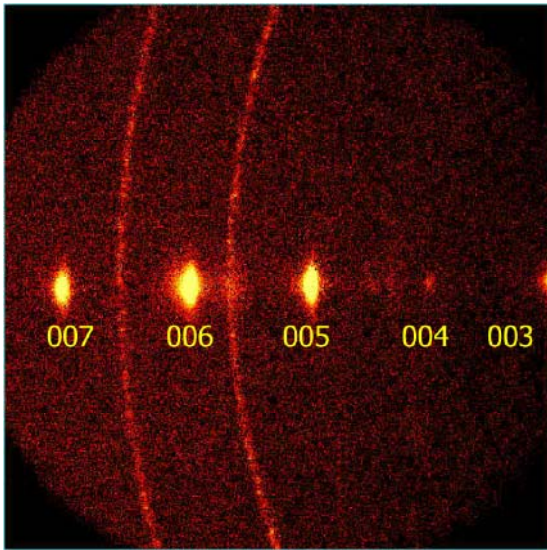
Fig. 90a. Bruker GADDS system showing good c-axis alignment of YBCO.
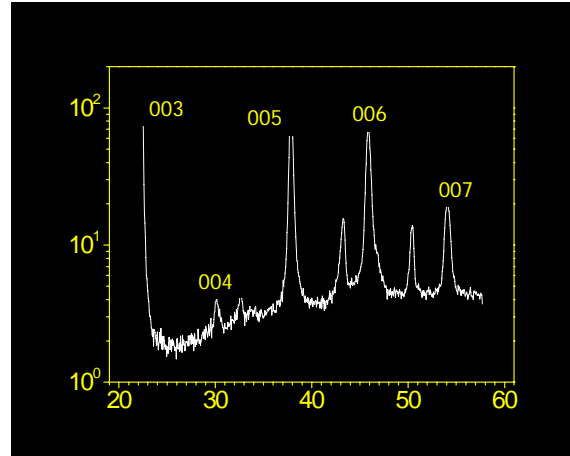
Fig. 90b. X-ray diffraction theta scan showing primarily 00l peaks.

Another advantage to engineered heating profiles is to minimize the thermal budget for high rate depositions. Fig. 91 compares deposition of two films both at 200 Hz and 1.8 m/h with two different heater profiles, the first (Fig. 91a) at a constant high temperature, and the second (engineered profile) (Fig. 91b) beginning at one end at a low temperature and then increasing across the deposition window to a higher temperature. The results show that the first profile resulted in a significant (103) line, indicating much a-axis oriented YBCO, while the engineered heater profile resulted in strong 00l spots (Fig. 91b), indicating good c-axis alignment.
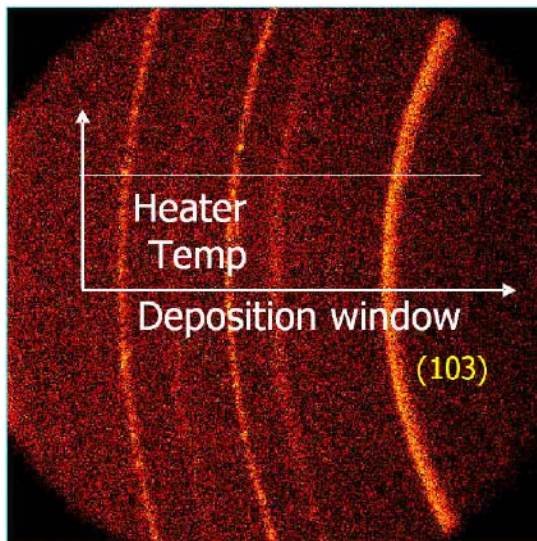
Fig. 91a. Flat heater profile and (103) oriented YBCO.
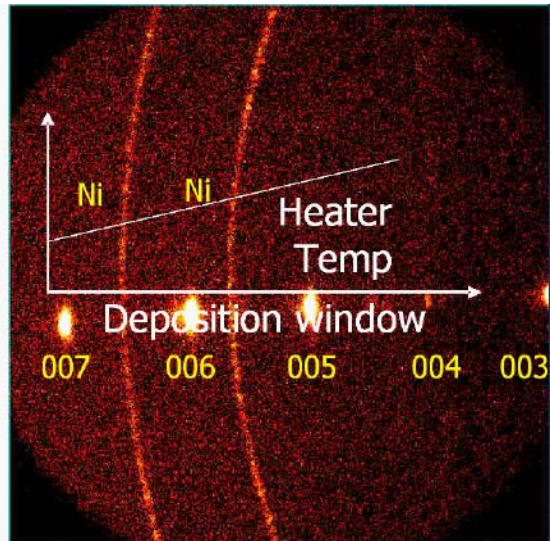
Fig. 91b. Engineered heater profile and sharp 00l peaks.

Ion scattering data indicate Cr, Al, and Mg diffuse into the YBCO (Fig. 92a) for an adversely reacted sample. With an engineered heater profile (Fig. 92b) however, Cr does not diffuse into the YBCO even thought some Al is present.
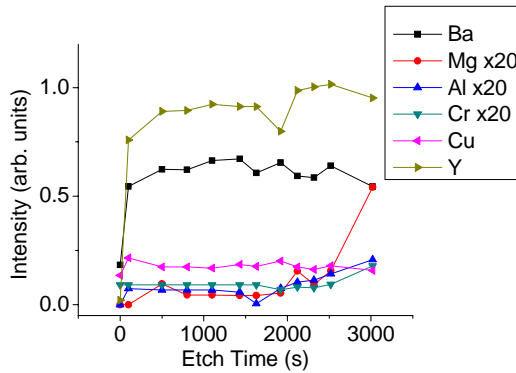
Fig. 92a. Ion scattering data for a YBCO sample grown with a flat heater profile and showing evidence of reaction with substrate elements.
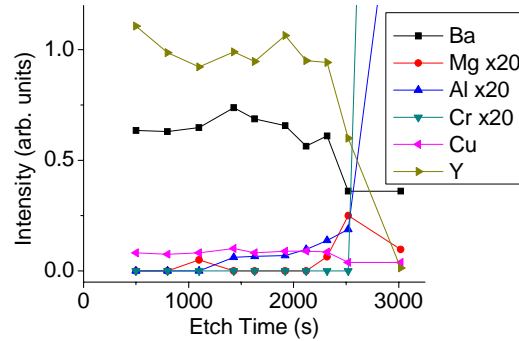
Fig. 92b. Ion scattering data for a YBCO sample grown with an engineered heater profile showing much less diffusion of substrate elements.

Samples made with the new heater show improvement (Fig. 93) in uniformity, reproducibility, and I_c. Optimization of the engineered heating profile, laser fluence, target-substrate distance, etc., led to significantly increased length uniformity.
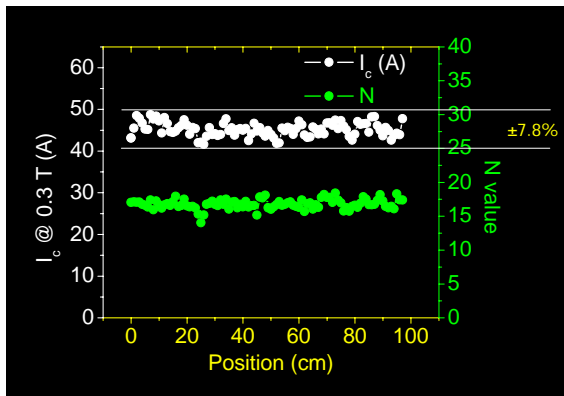
Fig. 93. Critical current and n value at 0.3 T and 75 K for a 1 μm YBCO sample on a 50 nm LMO buffer and the standard template stack.

We have also investigated the effects of copper plating as a current stabilizer on the performance of our CC's. The samples were plated with a standard Cu sulfate plating bath to deposit a 50 μm thickness on each side. This was not an optimized configuration, but the I_c decreased on average only about 2% after the plating, and the I_c uniformity was a good ±4.5%. Fig. 94 shows an current voltage characteristic for a Cu-plated CC at 75 K. The I_c value across 14 cm was a very repeatable 218 A. Above about 300 A, a significant amount of current begins to flow in the Cu and the slope of the characteristic changes. Above about 550 A, the sample experiences thermal runaway, and the sample was eventually destroyed at ~600 A. Without the Cu, the sample would have been destroyed at about ½ this current level.
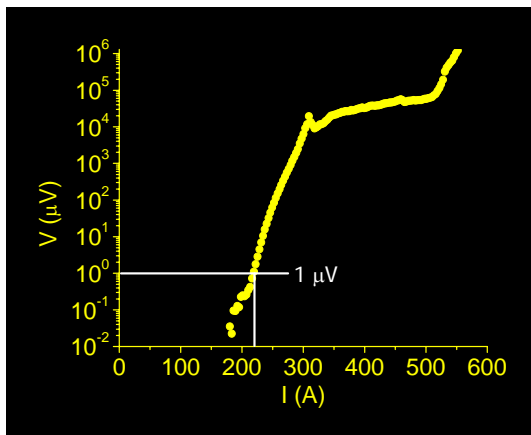
Fig. 94. Voltage as a function of current for a YBCO CC with 50 μm of Cu electroplated on each side.

We have also explored some alternative deposition techniques to PLD based on the data shown in Table 2. Because of some of these barriers for high throughput, the STC is pursuing reactive coevaporation (RCE) for fast deposition of the superconductor layer. Reactive coevaporation is a proven uniform process for deposition of YBCO on wafers in the electronics industry. A collaboration with Stanford University is testing the feasibility of high-rate YBCO deposition by RCE for wire manufacturing. The co-evaporation system is installed and operating at the Los Alamos Research Park, Fig. 95a. The e-beam evaporator is computer controlled such that the one e-gun (Fig. 95b) scans the three hearths at an appropriate rate and dwell time. Laser-atomic absorption spectroscopy is used for accurate feedback and growth rate control. The RCE system also uses inexpensive source materials (metals).

Fig. 95a. Reactive coevaporation system set up at LANL.
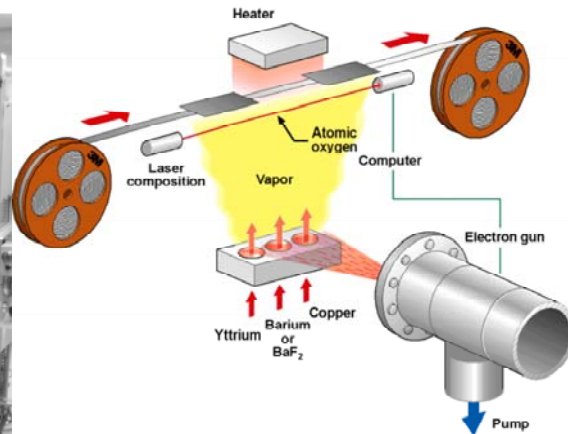
Fig. 95b. Schematic of the RCE system.

At present there are still some fundamental challenges for coated conductors in various applications. Table 2 lists several applications, areas where there have been significant accomplishments to date (checks), and areas where significant progress needs to be made (Xs). It is clear from this list that the area of ac losses still poses serious challenges for coated conductors.

Table 2. Fundamental challenges for CCs

	High I_c	I_c in magnetic field	Mechanical robustness	ac losses
Cables	4			X
Motors		4	X	X
Generators		4	X	X
Transformers		4		X

Fig. 96a shows the ac losses for a CC sample as a function of applied perpendicular (to the tape wide face) 60 Hz magnetic field at different ac transport currents. This is a typical state for a CC tape in a utility system, such as a power cable or an ac generator. At low fields, the losses are transport dominated, while above about 4 mT (40 Oe), not a very high field, the losses are field dominated. As can be seen from the figure, the loss levels are at least an order of magnitude too large for practical operation.

To aid in the study of these losses in CC, we have set up a new system (Fig. 96b) to investigate the positional dependent losses in a long CC. This system measures the magnetic ac losses, and has been set up to measure the losses every 1 cm, completing the measurements on a 5 m tape in 3 hours. The ac loss data can then be correlated with the measured dc transport critical current density, J_c. Fig. 96c shows the results of the ac loss measurements over a section of tape.
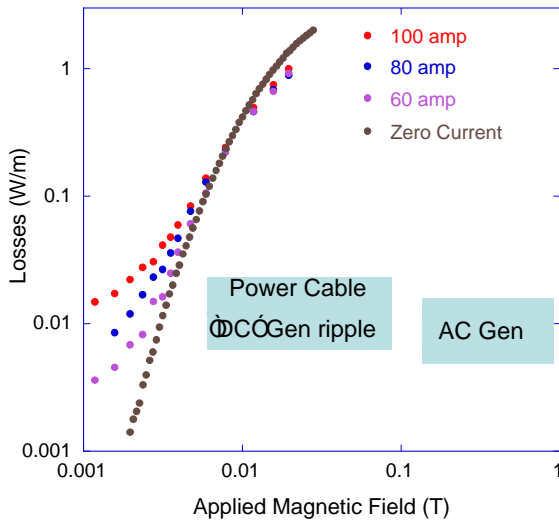
Fig. 96a. Ac losses in CC tape at 75 K carrying a 60 Hz transport current (I_c = 100 A) as a function of applied perpendicular 60 Hz magnetic field.
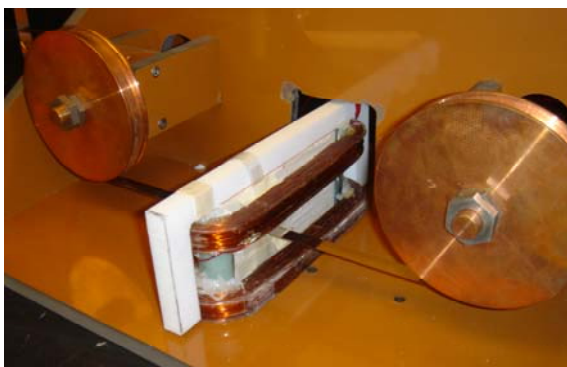
Fig. 96b. Experimental configuration for reel to reel ac loss measurement system.
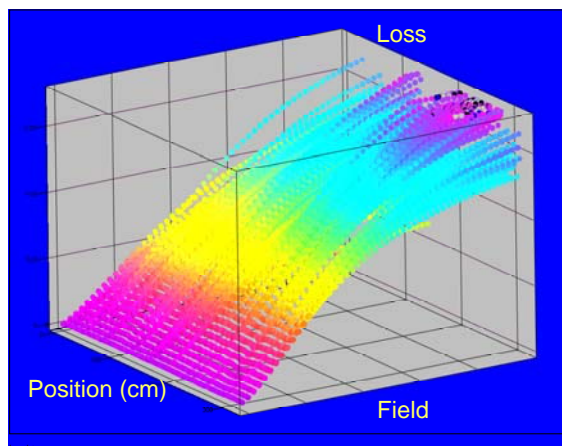
Fig. 96c. ac loss as a function of position and magnetic field for a long CC tape.

In summary, we have produced electropolished substrates over 100 m long with nm-scale surface roughness. Tape 3 cm wide and RABiTS tapes have also been polished for our industrial partners. IBAD MgO has been produced in 10 m lengths with in plane texture of 6 - 8°. Very high rates of 100 m/h have been demonstrated at slightly poorer texture levels. A TOF-ISARS surface analysis system has been installed and is providing *in situ* data for interdiffusion of substrate and buffer layers. Many meters of YBCO have been deposited on the IBAD MgO using PLD. An engineered heater profile has been used in conjunction with a new PLD substrate heater to improve the texture of the YBCO. PLD is producing CC meter long samples with champion values of 200 A/cm width. Cu plating of the CC results in a more robust conductor able to withstand higher fault currents. A reactive co-evaporation capability for YBCO deposition has been installed in the laboratory. A new facility has been established to measure ac losses of long length samples.

LANL provided technology and electropolished tape to industrial partners, both Hastelloy and RABiTS substrate. We provided 10's of meters of IBAD tape to industrial and university partners. LANL performed structural and electrical characterization on numerous samples from collaborators. We have ongoing collaborations with SuperPower, AMSC, and MetOx, Stanford U., U. Wisconsin, and Argonne and Oak Ridge National Laboratories.

2.2 System Technology

2.2.1 Long Term Vacuum Maintenance in HTS Equipment without External Pumping

J.A. Waynert, F.C. Prenger, T.A. Jankowski, and J.A. Stewart

Newly developed HTS devices generally operate at temperatures near 20-30 K or 60-70 K. At these low operating temperatures there is a universal desire to minimize the heat leak to the low temperature region. The heat leaks arise from conduction through support structure, radiation exchange between low and high temperature features, and convection through the remnant gas in the vacuum space. The conduction contribution can be controlled through knowledgeable design and appropriate selection of materials for the support configuration. The radiation exchange is minimized by use of multilayer insulation, materials with low emissivity, and controlling lines-of-sight between high and low temperature features. Here, we address the third factor contributing to the heat leak, the vacuum level and how to maintain the vacuum level for extended periods without the use of external, electrically driven vacuum pumps. There are many examples of the achievement of long-term vacuum in sealed-off systems. Besides vacuum tubes, and some particle accelerators, there are portable dewars, vacuum jacketed transfer lines and over-the-road cryogenic transport trailers that maintain low vacuum levels in their insulating space for five to ten years. Thus, much of the science and technology is known, but each situation requires an individual analysis. Here we present a roadmap for that analysis.

The general approach requires the knowledge of the outgassing rates and molecular species for the various materials present in the vacuum space. There may be several possible sources for gasses in addition to outgassing from the surface of materials, such as virtual leaks (slow leakage of gas trapped in small voids, such as threads), external leaks, and permeation through seals. Some of these will be discussed in a later section. The product of the three terms: the outgassing rate for a given gas species in terms of say, molecules/sec/m^2; the surface area contributing to the outgassing; and the time between maintenance intervals; yields the total quantity of a given species that must be removed to achieve an acceptable residual pressure. The molecules can be removed by a combination of physical adsorption and chemisorption on the surface of, or absorption into the bulk of specialized scavenging materials such as charcoals and getters. Given the total quantity of gas to be adsorbed, the amount of getter material can be estimated from available data.

It is instructive to work through an example. For simplicity, assume there is a component to be maintained at 77 K. The component has a volume of 2 m^3, which includes a multilayer blanket of insulation (MLI) of volume 0.2 m^3, all inside a vacuum chamber of volume 5 m^3. We assume half of the MLI volume is at room temperature and the remaining half is at 77 K. The volume of gas at room temperature, 295 K, which includes 1/2 the MLI volume, is 3.1 m^3. Hence, there are two gas volumes, V_1=3.1 m^3 at T_1=295 K and V_2=0.1 m^3 at T_2=77 K. In thermal equilibrium the pressure, assumed to be in the molecular flow regime, near the room temperature wall will be different from that near the cold surfaces. The pressure variation can be approximated from a related system. For two volumes at two different temperatures connected together by an aperture and in thermal equilibrium, the pressures in the two volumes are related by

$$P_1/P_2 = (T_1/T_2)^{1/2} = (295/77)^{1/2} = 1.96 \qquad (1)$$

It is convenient to obtain an effective volume V_{eff} at room temperature and at pressure P_1 such that the total number of molecules in the gas phase is equivalent to the two volume, two temperature system. Using the ideal gas law, and letting ρ be the mass density

$$\rho_1 V_1 + \rho_2 V_2 = \rho_1 V_{eff} \tag{2}$$

yields $V_{eff} = 3.3m^3$. Many cryogenic vacuum insulated systems begin to experience a significant increase in the heat load when the vacuum level P1 reaches 6.7 mPa ($5x\ 10^{-5}$ torr). Based on the ideal gas law, at this pressure, and volume V_{eff} from equation (2), our system contains $5.4x\ 10^{18}$ molecules. It is typical in outgassing and cryopumping literature to report the number of molecules in units of pressure x volume, such as Pa-m^3 at 295 K which is equivalent to $2.46x10^{20}$ particles (1 torr-liter = $3.27x10^{19}$ particles). Thus, our volume has 0.022 Pa-m^3 (0.17 torr-liter) particles in the gas phase at the onset of vacuum failure. Passive pumping may be achieved by adsorbing molecules on materials such as activated charcoal or a molecular sieve. For simplicity, let's assume we are considering using 100 g of a molecular sieve with a microscopic area per unit mass of 600 m^2/g. If one monolayer is considered to be $1x10^{19}$ molecules/m^2, which is roughly equivalent to a square array of molecules of diameter $3.6x10^{-10}$ m, then the 100 g could pump $6x10^{23}$ molecules or $2.4x\ 10^3$ Pa-m^3.

Adsorption data for a given species of gas are usually quoted as a fraction of a monolayer of coverage on the surface as a function of the pressure at a fixed temperature. In our example, we want adsorption isotherms for 77 K at pressure $P_2 = 3.4$ mPa ($2.6x\ 10^{-5}$ torr) based on equation (1). The gasses of interest are those common to vacuum chambers using stainless steel, aluminum, G-10 and similar materials and gasses that do not condense at 77 K. Table 3 is a list of the 10 gasses of interest and their adsorption capacities. As can be seen from the last column, most of the gasses are pumped quite well, with the exception of helium, hydrogen and neon.

Is the suggested 100 g of molecular sieve sufficient? The answer depends on the amount of gas to be adsorbed, which is dependent on the sources of the gas. Let's consider leaks first. If the vacuum is intended to have a lifetime of 5 years or 1.6×10^8 seconds, the acceptable leak rate for helium, based on Table 3 would be $(2.2x10^{-2}$ Pa-m$^3)/(1.6x\ 10^8$ seconds) = $1.4x\ 10^{-10}$ Pa-m^3/sec (1×10^{-9} torr-liter/sec). It is certainly feasible to measure a leak rate this small, but it may not be a desirable requirement from a manufacturing standpoint. A small ion pump might be needed to offset the leak rate requirement. Generally, helium and neon are present in a vacuum system only through external leaks to the atmosphere and then in relatively small proportion, less than 18 parts per million. If we assume the external leak issue has been addressed, the most problematic residual gas is hydrogen. Over the 5 year period, and assuming the 5 m^3 volume has 18 m^2 of warm surface area, the allowable outgassing rate for hydrogen is $2.2x10^{-2}$ Pa-m^3/$1.6x10^8$ sec/18 m^2 = $7.6x10^{-12}$ Pa-m^3/m^2-sec ($5.7x10^{-15}$ torr-liter/cm^2-sec). This outgassing rate is five to seven orders of magnitude lower than might be achieved with reasonable attention to cleaning and surface preparation. Thus, some additional means of pumping hydrogen is necessary.

TABLE 3. Adsorption isotherm data for various gasses at 77 K and P_2=3.4 mPa. The column 'Number of molecules in gas phase' assumes P_1=6.7 mPa in V_{eff}=3.3 m^3 or 0.022 Pa-m^3 molecules.

Gas	Fraction of monolayer coverage at 77 K	Number of molecules adsorbed (Pa-m^3)	Total number of molecules adsorbed + gas phase (Pa-m^3)	Fraction of gas in gas phase
Helium	5×10^{-10}	1.2×10^{-6}	2.2×10^{-2}	1.0
Hydrogen	5×10^{-8}	1.2×10^{-4}	2.2×10^{-2}	1.0
Neon	1×10^{-9}	2.4×10^{-6}	2.2×10^{-2}	1.0
Nitrogen	7×10^{-2}	1.7×10^{2}	1.7×10^{2}	1.3×10^{-4}
Argon	6×10^{-3}	1.4×10^{1}	1.4×10^{1}	1.6×10^{-3}
Carbon Monoxide	1.5×10^{-1}	3.6×10^{2}	3.6×10^{2}	6.1×10^{-5}
Methane	1×10^{-1}	2.4×10^{2}	2.4×10^{2}	9.2×10^{-5}
Oxygen	1×10^{-1}	2.4×10^{2}	2.4×10^{2}	9.2×10^{-5}
Carbon Dioxide	>1	$>2.4 \times 10^{3}$	$>2.4 \times 10^{3}$	$<9.2 \times 10^{-6}$
Water vapor	>>1	$>>2.4 \times 10^{3}$	$>>2.4 \times 10^{3}$	$<<9.2 \times 10^{-6}$

A common passive pumping system for hydrogen is a non-evaporable getter (NEG) based on zirconium or titanium alloys. In this case, the molecules chemically bond or, at least, strongly sorb to the surface of the NEG rather than forming a comparatively low-energy, physical bond to the charcoal adsorber. An additional advantage of the NEG is that the molecules are not re-introduced to the vacuum system when the system is brought up to room temperature as is the case with physical adsorbent materials mounted to cold surfaces. A typical commercial NEG has a hydrogen capacity of 2.6 Pa-m^3/g (20 torr-liter/g) for an alloy of zirconium operating near room temperature. Using a representative outgassing rate of 1.3×10^{-5} Pa-m^3/m^2-sec (1×10^{-8} torr-liter/cm^2-sec), we get an accumulation of 3.7×10^4 Pa-m^3 of hydrogen for the 5 years and 18 m^2 of surface. (We have made the assumption that all the gas evolved is hydrogen.) This would imply a need for 14 kg of getter, a large amount of material and likely unreasonable to pump with this commercial NEG getter. Another issue is that the hydrogen concentration within the getter operates in equilibrium with the hydrogen in the gas phase; lower concentrations are obtained with lower equilibrium pressures. For very high vacuum this implies the need for more getter material, but for pressures in the mPa range with the getter operating near room temperature, this is not an issue.

As seen in the example above, it is relatively easy to calculate the total gas load evolved in a system over a given period of time if the outgassing rate is known. The quantity of adsorbent/getter needed to maintain a specific vacuum level can then be estimated. The difficulty is in determining the outgassing rate. There are numerous sources of data on the outgassing properties of materials. Unfortunately, the outgassing properties are dependent on the type of material (aluminum, stainless steel, composites, etc.); how the material is prepared (machining, welding, polishing, etc.); how the materials are cleaned (chemical cleaning, etching, electropolishing, plating, baking out); how the materials are handled (gloves, machines); what the assembly environment is like (cleanliness, humidity); whether the device is baked out or not; and finally, the operating temperature of the material in the working device. The best approach is to install a reasonable amount

of adsorbent/getter materials in the actual device and measure the pressure and gas content after several extended periods of time, say every few months. From the pressure rise versus time and the known surface area of the materials, an average outgassing rate can be determined. Another approach is to measure the outgassing rates of the materials to be used in the device. Although there are several approaches to measuring outgassing rates, we chose the throughput method. The experimental equipment is shown in Fig. 97. A sample is placed in a chamber that is pumped through an orifice of known conductance. The pressure drop across the orifice times the conductance yields the throughput which when divided by the surface area of the sample gives the measured outgassing rate. There are a number of complicating issues: the possible pumping or outgassing from the pressure gauges and the residual gas analyzer (if used); the background outgassing from the chamber walls; the repeatability of the chamber outgassing on being brought up to air to admit new samples; and finally, the impact of gas evolved from the surface of the sample but, upon striking the chamber walls, being re-adsorbed. All except the last effect are probably familiar to the reader and can be addressed by standard methods. The re-adsorption effect is less well known and will be discussed further here.
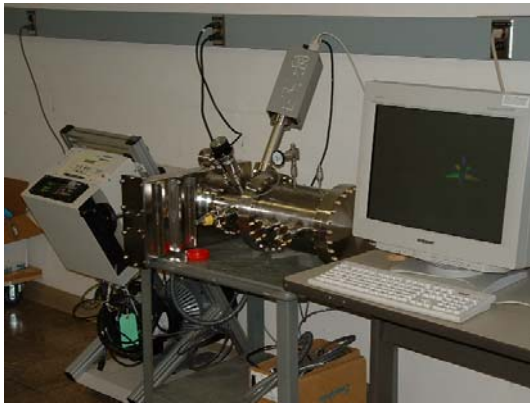
Fig. 97a. Photo of the chamber, pumping system and data acquisition system.
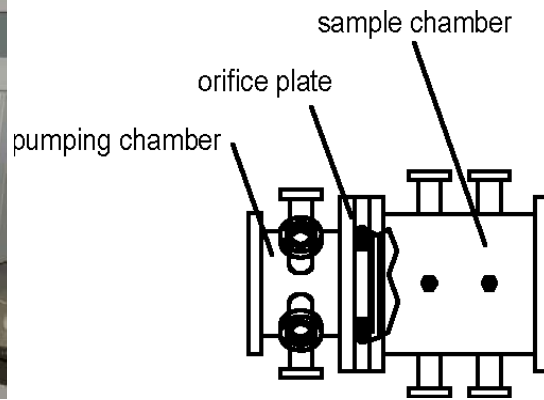
Fig. 97b. Schematic of the vacuum system.

The outgassing rates reported in the literature frequently do not distinguish between the measured rate, such as the flow rate through the orifice discussed above, and the intrinsic rate, which is the molecular evolution from the sample surface. For example, the effect of re-adsorption on an empty sample chamber can be shown to be

$$F_{measure}/F_{true} = (a/A_c s_c)/(1+a/A_c s_c) \qquad (3)$$

where 'a' is the orifice area, A_c is the geometric surface area of the chamber, and s_c is the sticking coefficient or probability of a particle striking the surface to stick rather than reflect off. The quantity in brackets in equation (3) is frequently called the pumping parameter. If the sticking coefficient is zero, i.e., there is no re-adsorption, then the measured rate is equal to the true rate. In the system used by the authors, 0.12 cm^2 < a < 2.0 cm^2 and $A_c = 2920$ cm^2. Hence, Equation (3) states that the measured outgassing rate is always less than the true outgassing rate, and possibly by several orders of magnitude, depending on the value of s_c. Figure 98a shows the measured outgassing rate after 50 hours of pumping on an empty, but baked out 304L stainless steel sample chamber for several different orifice sizes. As can be seen, the measured outgassing rate is a function of the pumping parameter. The best values for $F_{true} = 1.6 \times 10^{-7}$ Pa- m^3/m^2-sec and $s_c = 0.0004$ are determined by minimizing the root-mean-square (rms) difference between the experimentally and theoretically determined ratios of equation (3).
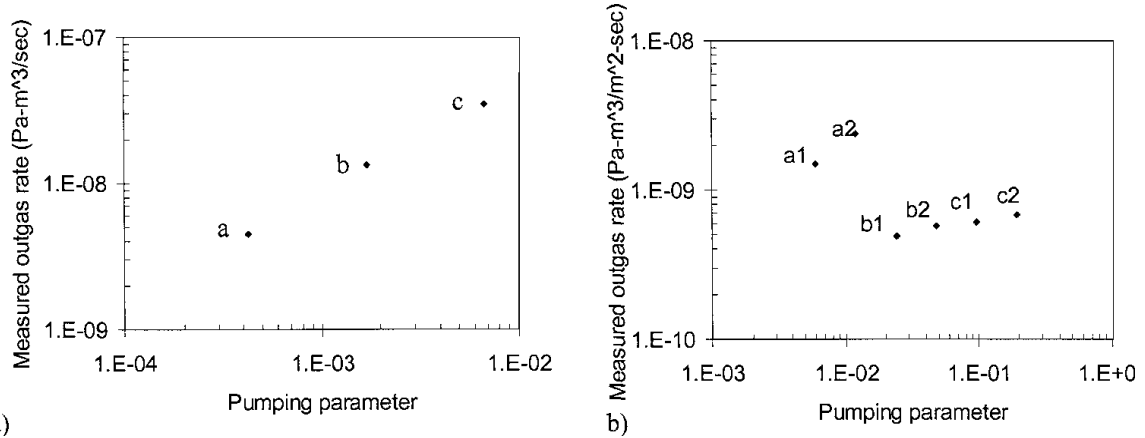
Fig. 98. a) On the left is a plot of the outgassing rate of the empty sample chamber for various values of the pumping parameter achieved by varying the diameter of the orifice: a - diameter = 0.4 cm; b - diameter = 0.8 cm; c - diameter = 1.6 cm. On the right b) is a plot of measured outgassing data on 304L stainless steel samples. The sample surface area is 51.6 cm^2. Point a1 is for 4 samples, a2 has 2 samples, both with "a" orifice; b1 - 4 samples, b2 - 2 samples, both with "b" orifice; c1 - 4 samples c2 - 2 samples, both with "c" orifice.

A derivation similar to that used for equation (3) can be used to show that with a sample in the chamber, the true outgassing rate of the sample F^s_{true} is given by

$$F^s_{true} = F^s_{meas}\left(1+\gamma_c\right)+F^s_{meas}\gamma_s + \frac{F^c_{true}}{\left(1+\gamma_c\right)}\frac{A_c}{A_s}\gamma_s \text{ , where } \quad \gamma_i = \frac{A_i s_i}{a}$$

(4)

and 's' refers to sample, 'c' refers to chamber. Figure 98b shows data taken on several 304L stainless steel (SS) samples for several different pumping parameters. Unlike the empty chamber analysis though, the rms difference between the theoretical and experimental values for F^s_{true} given a value of s_c does not undergo a minimum value. The calculation of F^s_{true} would be greatly simplified if the value of s_c were sufficiently small; only the first term in equation (4) would be needed. Table 4 shows the contribution of the individual terms in equation (4) to F^s_{true} as the value of ss is changed. It can be seen that term 1 of equation (3) represents 98, 80, and 30% of the total true outgassing rate for the SS samples and 100, 97, and 76% for the G-10 samples for s_c equals 0.0001, 0.001, and 0.01, respectively. It appears that for the relatively low outgassing SS, the validity of using only the first term decreases rapidly as the sticking coefficient increases. But we might expect the sticking coefficient of the SS to be similar to that of the chamber, again suggesting that the first term does describe the true outgassing value. Unexpectedly, the first term fairly accurately describes the high outgassing G-10. The most significant advantage to using only the first term is that the true outgassing is then known to be (1 +γ_c) larger than the measured outgassing rate.

TABLE 4. The individual contribution of the three terms in equation (4) to the value of the true sample outgassing rate, column 6, as a function of the sample sticking coefficient for SS samples with 1.6 cm orifice assuming the average value for the measured outgassing is 4×10^{-7} Pa-m^3/m^2-sec. Comparable values for the G-10 samples, same orifice, assuming the measured outgassing is 1.7×10^{-4} Pa-m^3/m^2-sec are given.

s_s	s_c	Term 1 Pa-m^3/m^2-sec	Term 2 Pa-m^3/m^2-sec	Term 3 Pa-m^3/m^2-sec	F_{true}^s Pa-m^3/m^2-sec	F_{true}^c Pa-m^3/m^2-sec
0.00001	0.0004	6.4E-7	2.1E-10	1.5E-9	6.4E-7	1.2E-10
0.0001	0.0004	6.4E-7	2.1E-9	1.5E-8	6.5E-7	1.2E-10
0.001	0.0004	6.4E-7	2.1E-8	1.5E-7	8.1E-7	1.2E-10
0.01	0.0004	6.4E-7	2.1E-7	1.5E-6	2.3E-6	1.2E-10
G-10 sample data below						
0.00001	0.0004	2.8E-4	9.0E-8	1.5E-9	2.8E-4	1.2E-10
0.0001	0.0004	2.8E-4	9.0E-7	1.5E-8	2.8E-4	1.2E-10
0.001	0.0004	2.8E-4	9.0E-6	1.5E-7	2.9E-4	1.2E-10
0.01	0.0004	2.8E-4	9.0E-5	1.5E-6	3.7E-4	1.2E-10

We have presented a general approach to determining the outgassing properties of typical materials used in HTS devices, the likely gas constituents, techniques for determining adsorber and getter materials and estimating the quantity of such materials needed based on the operating temperature of the device. As can be seen, the prescription for achieving long term vacuum maintenance is fairly straightforward once the vacuum load is known, but determining the vacuum loading is very case specific and far from trivial.

[From J.A. Waynert et al., Advances in Cryogenic Engineering **49**, 635 (2004).]

2.2.2 Magnetic Separation SPI: Waste Water Treatment

J.A. Waynert, F.C. Prenger, L.A. Wort, T.Y. Ying, R.M. Wingo, J.A. Stewart, D.E. Peterson, J.G. Bernard (DuPont, then LANL), and C. Rey (DuPont, now ORNL), M. Johnson, New Mexico State University

This is a Superconductivity Partnerships with Industry (SPI) project with DuPont employee J.G. Bernard stationed at LANL and leading the effort there. Magnetic separation has received much attention recently due to industrial, medical and governmental interest in selective separation technologies. This is a technique in which magnetic particles are removed from a process stream as they pass through a region of imposed magnetic field. High gradient magnetic separation (HGMS) takes this technology further by using large magnetic field gradients generated on a matrix to accomplish separations of micron-sized particles. A schematic of the system is shown in Fig. 99.
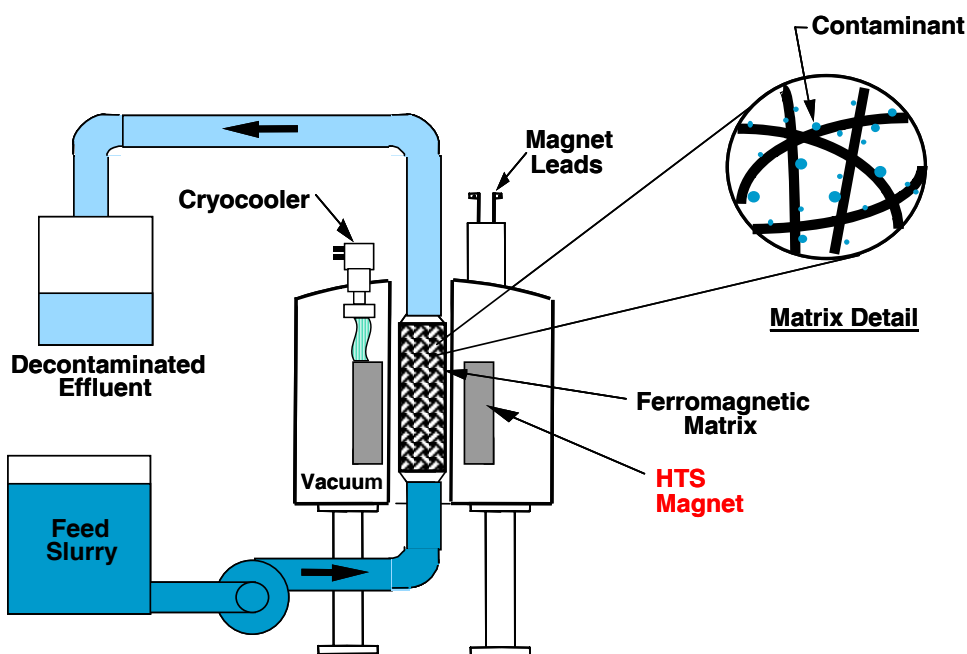
Fig. 99. Schematic of the HGMS process.

This technology has been shown to be very efficient at removing metal particles from such materials as kaolin clay and TiO_2. There are also many potential new market applications, such as wastewater treatment, water purification, medical/biological separations, and the capture of specific target compounds. One application with potential near term success is the removal of heavy metals from mine drainage water. There are thousands of mines in the USA with heavy metal drainage problems, endangering wildlife and humans through pollution of surface and ground water supplies for irrigation and domestic use. The market opportunity for this application is significant if the technique can be made cost effective.

An efficient and reliable high-temperature superconducting (HTS) magnet (Fig. 100) was used as the source of the magnetic field. It employs an HTS magnet wound from Bi-2223/Ag tape. It is 15.5 cm high with a 2.5 cm cold bore and is cooled by a two stage Gifford-McMahon cryocooler. Cooled to 40 K, the magnet can generate a central field of 2 T at a current of 120 A. This system provides significant advantages over conventional,

resistive coil technology. Power usage is significantly reduced. HTS magnets can also be portable in a cryogen-free configuration with cooling requirements supplied by a cryocooler powered by electricity or another source. This portability can be important for many applications, especially for temporary clean up or for use at a remote site. HTS magnets result in a smaller footprint than conventional systems, which is potentially less costly because less space is required, and support and auxiliary structures can be reduced in size and weight.

Fig. 100. Photographs of HGMS apparatus. On the left is a view of the magnet power supply In the center is the HTS magnet and other apparatus. The column in which the separations occur is shown on the right. It fits in the warm bore of the magnet.

The first step of the magnetic separation process takes advantage of the properties of a class of compounds known as ferrites. When the metals in a ferrite are iron, it is known as magnetite (Fe_3O_4), or more precisely $FeO \bullet Fe_2O_3$, and contains iron in the +2 and +3 oxidations states. A wide range of ferrites containing other metals are also known. These are _ferrimagnetic_ crystalline materials that precipitate as they form and are only soluble in strongly acidic media.

The equations showing the chemical reactions that occur are as follows:

$Fe^{2+} + Fe^{3+} + Fe^{3+} + 8 OH^- \rightarrow GR$ (solid) $\rightarrow FeOFeFeO_3$ (solid)$+ 4 H_2O$

$Fe^{2+} + M^{3+} + Fe^{3+} + 8 OH^- \rightarrow GR$ (solid) $\rightarrow FeOMFeO_3$ (solid) $+ 4 H_2O$

$M^{2+} + Fe^{3+} + Fe^{3+} + 8 OH^- \rightarrow GR$ (solid) $\rightarrow MOFeFeO_3$ (solid) $+ 4 H_2O$
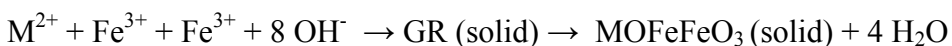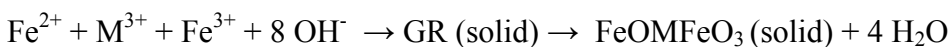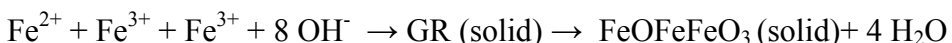
(M = Metal (i. e., Cu^{2+}, Mn^{2+}, Cd^{2+}, Pb^{2+}, Ag^+, As^{3+}); $FeOFe_2O_3 = Fe_3O_4$ (magnetite); substituted magnetite = ferrite)

Because this ferrite process uses fewer chemicals than the conventional precipitation technique, it is safer. It is also an environmentally friendly process that produces non-hazardous, non-leachable solid waste. Additionally, advantages of the ferrite co-precipitation technique, relative to traditional chemical precipitation methods, include: 1) simultaneous removal of a wide variety of metal ions, 2) precipitates have chemical stability with little risk of subsequent acidic dissolution under environmental conditions.

Experiments have established that ferrite formation occurs very readily in nanopure water. Ferrite formation was also demonstrated at temperatures below 10˚C that are often

associated with mine drainage water, though it forms at a slower rate. However, in a realistic mine drainage simulant, dehydration of the GR intermediate to form ferrite was inhibited. After further experiments, it was determined that calcium ions in the simulant acted to "poison" the reaction by preventing GR dehydration. Since GR has only a very weak magnetic susceptibility, magnetic separation under these conditions is not feasible. Removal of calcium ions prior to magnetite formation was considered but deemed to be cost ineffective. Increasing the temperature or aging the GR for at least several hours helped to alleviate this problem, but these are not practical solutions for the treatment of large volumes of water.

In an attempt to circumvent the problem of calcium poisoning, the reaction was seeded with small amounts of pre-formed magnetite. It was hoped this would provide a surface upon which nucleation and further ferrite formation would take place. Initial experiments demonstrated that GR formed on the surface of the magnetite seed, producing particles with magnetic properties suitable for magnetic separation, Fig. 101. Full conversion to a high quality ferrite was accomplished by filtration followed by drying the solids under an inert atmosphere. XRD (x-ray diffraction) experiments have confirmed that the magnetic product is indeed a ferrite and not some other dark colored oxide. Toxic characteristic leaching procedure (TCLP) experiments show minimal heavy metal leaching using a scaled down version of the standard EPA test. This is a direct result of the ferrite stability, and allows for inexpensive disposal in a non-hazardous waste landfill. Failure to sufficiently dry a sample causes variable degrees of decomposition to a brown, amorphous product if it is exposed to air for long periods of time.
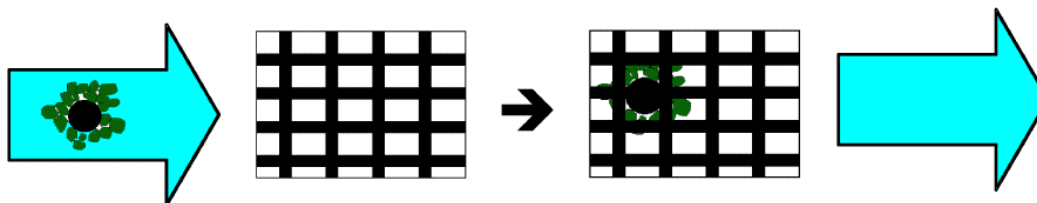
Fig. 101. The black magnetite acts as a "seed" for the green rust in the input stream (left) that during magnetic separation is attracted to the matrix, resulting in a purified effluent (right).

Some of the targets for the present work were to optimize the ferrite and HGMS processes, to determine the controlling parameters and ranges, including: particle concentrations (magnetite seed, Fe^{2+}), type of stainless steel wool (extra fine to coarse), applied magnetic field strength, flow velocity in the separator, residence time in the separator, and finally, to determine the scaling issues from laboratory to pilot plant.

The practical application of HGMS to the real world was to clean the water from the Leadville (Colorado) Mine Drainage Tunnel (LMDT), for which the contamination levels and target levels for effluent are shown in Table 5. One of the most stringent reductions is in the amount of Mn. The Environmental Protection Agency has designated the LMDT as a Superfund site, and the Bureau of Reclamation is funding a test bed for the Leadville Mine Drainage Tunnel (LMDT) treatment facility. This work is also being performed as a pilot plant partnership with Leadville Institute of Science and Technology (LIST).

The performance of the HGMS procedure can be measured by recording the breakthrough volume. This occurs when the capacity of the separator is reached and particles begin to escape. Breakthrough was defined as 1 ppm of particles collected in a 20 mL effluent vial as measured by a turbidimeter. In the experiments that follow, the breakthrough volume was limited by GR shearing from the seed during the magnetic separation and percolating through the separator. Developing ways to increase the

seed/GR stability should increase the breakthrough volume. Schematically, the process is illustrated in Fig. 102.

Table 5. Heavy Metal Contaminants at the LMDT

Contaminant	Influent water (mg/L)	Target (mg/L)
Zn	3.6	0.084
Cu	< 0.009	0.009
Pb	0.0031	0.003
Cd	0.02	0.0009
Ag	< 0.001	0.00005
Fe	1.4	1.00
Mn	1.8	0.05

a   b   c
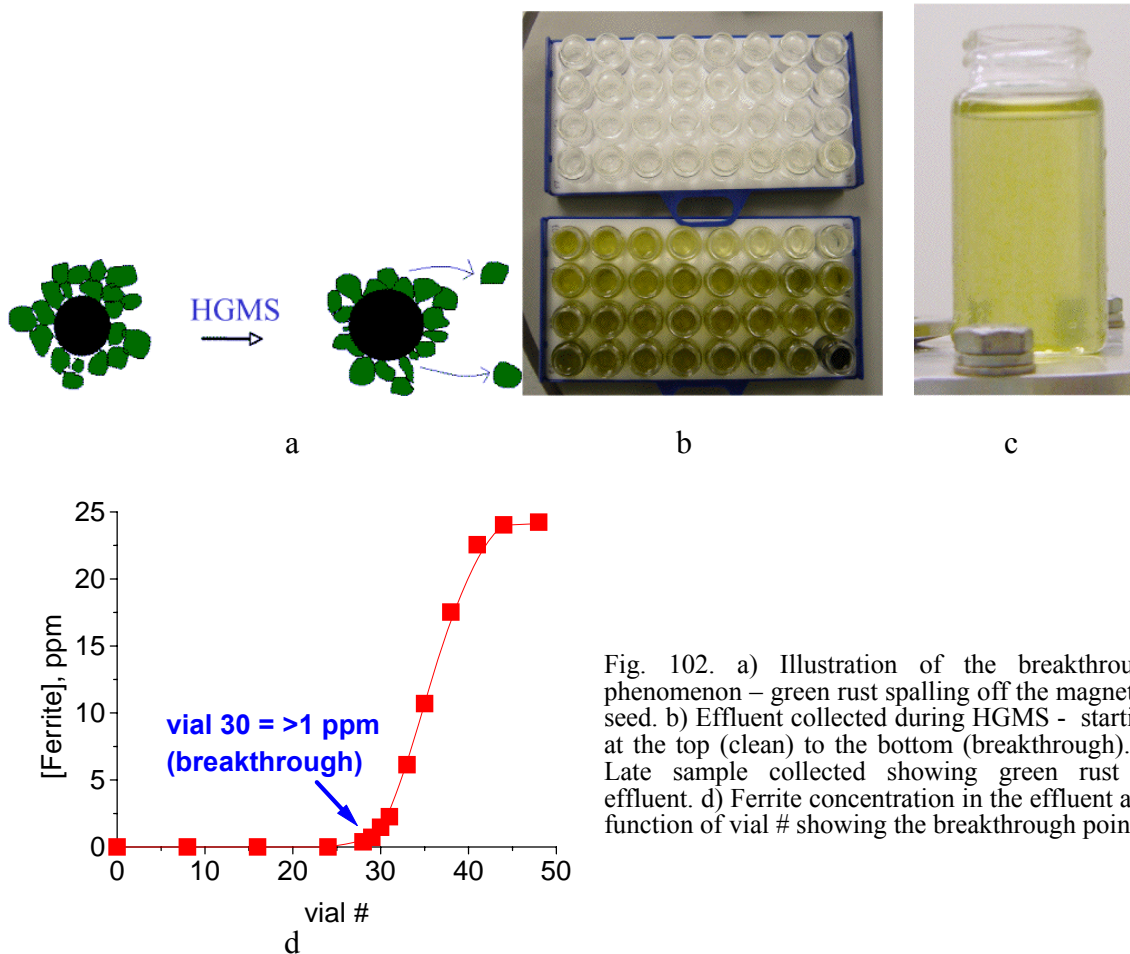
Fig. 102. a) Illustration of the breakthrough phenomenon – green rust spalling off the magnetite seed. b) Effluent collected during HGMS - starting at the top (clean) to the bottom (breakthrough). c) Late sample collected showing green rust in effluent. d) Ferrite concentration in the effluent as a function of vial # showing the breakthrough point.

d

We have determined the capacity of the HGMS system as a function of applied magnetic field strength in the matrix. Fig. 103 shows the result that the separator capacity saturates

above about 1 T. This is consistent with the saturation magnetization of the stainless steel wool that forms the matrix.
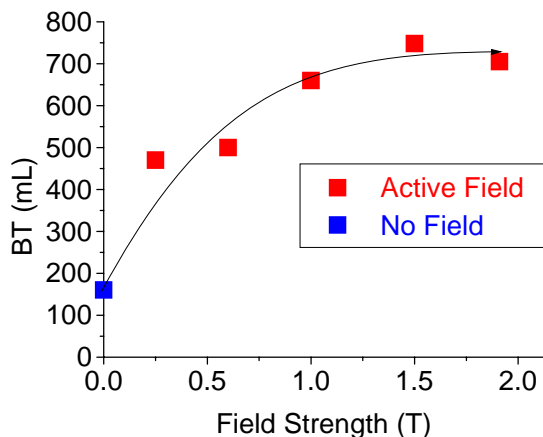
Fig. 103. Magnetic separator capacity as a function of magnetic field strength.

Fig. 104a shows the separator capacity as a function of superficial velocity, the nominal velocity of fluid through the separator column. Clearly, there is a trade-off between separator capacity and process time. The other time that is important in the process is the reaction time, the time for the input, the feed slurry, to react to form ferrite (green rust) and for this to attach to the magnetite seed particles. Fig. 104b indicates that a time of 3 minutes is sufficient for the reactions to occur and for the pH to be stablilized.
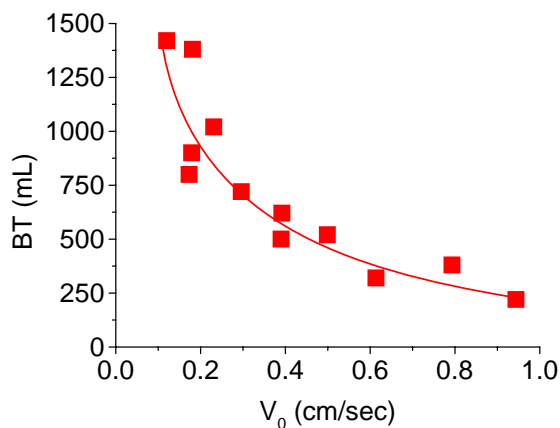
Fig. 104a. Magnetic separator output as a function of superficial velocity.
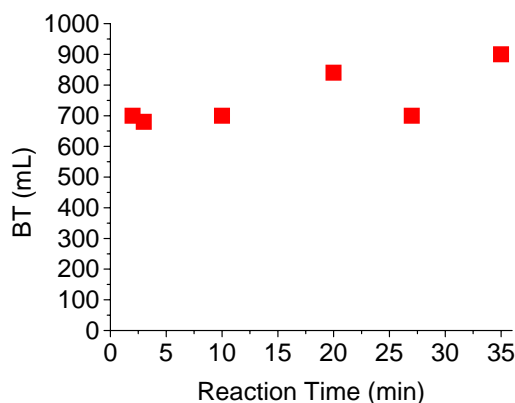
Fig. 104b. Magnetic separator output as a function of reaction time of the feed stream.

From our experiments to date, we may design an optimized laboratory-scale procedure for treating LMDT water. We conclude first that metal removal from LMDT water is a feasible process using a lab-scale HGMS. An optimized procedure might involve 100 ppm magnetite seed and 100 ppm Fe(II), a 3-4 minute reaction time, a high matrix packing density, a superficial velocity of ~0.2 cm/s, a maximum field strength of ~1 T, no requirement for excess oxygen, extra fine or finer stainless steel wool matrix, and column cleaning with high velocity water backflush, air sparge, and column agitation.

For a scale up pilot facility at Leadville, many factors need to be considered. The system should be automated with computerized monitoring and automation of the chemicals, pH, mixing, flow rate, flow path, etc. Chemical use and cost should scale directly with size.

Several considerations apply to the column (size, quantity of matrix, etc.), because these affect the processing cycles and are dependent on the water volume and composition. The column should also be monitored for possible capacity degradation with time. The method of ferrite synthesis requires that the method of solid/liquid separation (e.g., filter press, centrifuge) and controlling exposure to oxygen (e.g., with a nitrogen generator) be examined. Finally, cost is always a consideration in the selection of capital equipment.

A concept for a pilot plant is shown in Fig. 105. This is designed to fit on two pallets for ease of assembly, transportation, and siting. It is designed to treat a stream of 10 gal/minute (~39 l/m) in a continuous fashion. There are two separator units so that one can be operated to produce purified effluent while the other is backflushed (to remove the separated metals) to the holding tank, centrifuge, and ultimate landfill disposal.
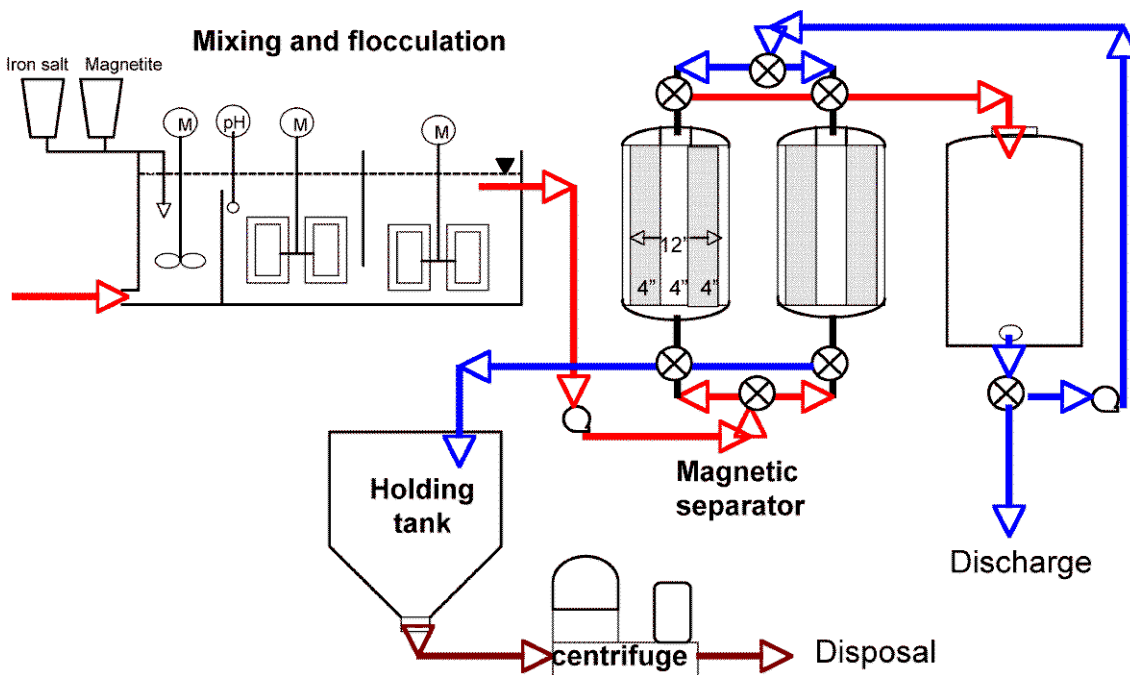
Fig. 105. Conceptual design for a continuous process pilot plat that could fit on two pallets.

To summarize the work that has been accomplished to date, we have determined the controlling parameters and ranges for the ferrite process and have performed a parameter sensitivity evaluation and optimization. We have optimized the ferrite and HGMS processes. The process has been optimized for a specific application or site (Leadville Mine Drainage Tunnel), and we have determined how process variables might change for different conditions or applications. We have determined the scaling issues in going from laboratory scale to a pilot plant including the quantities of chemicals required and processing times. We have also established a pilot plant partner with LIST.

Future plans call for extending the program with DuPont or another possible partner. This may be necessary because DuPont appears to have realigned their R&D direction/portfolio and may discontinue support of this program. The HGMS technology needs to be refined and extended to other sites or applications. A larger HTS magnet needs to be developed at LANL to test some of the scale up calculations. Finally, a pilot plant facility should be designed, fabricated, assembled and tested to verify its operational capability.

Postscript: DuPont did end their participation in the SPI program and this project at LANL was terminated.

2.2.3 Open Geometry MRI Superconductivity Partnership Initiative: National Laboratory Support

T.G. Holesinger, J.O. Willis, J.Y. Coulter, and J. Kennison, (National Renewable Energy Laboratory): R. Bhattacharya, P. Spagnol, T. Chaudhuri, S. Phok

The goal of this effort is to provide unique expertise and capabilities that exist at the National Laboratories to our industrial partners in support of the Open Geometry MRI Superconductivity Partnership Initiative. The main LANL contribution is in powder synthesis, microscopy, and electrical characterization. Work at the NREL is in nanoparticle additions for improving flux pinning.

One of the major LANL goals ts to improve the morphology of the Bi-2212 phase by elimination of large second phase particles, which can act to degrade current transport. We have found that alumina addition to the starting powder is a viable approach for refinement of secondary phases in Bi-2212 tapes, as seen in Fig. 106a (top). With no alumina, large secondary phases can disrupt the local alignment of the superconducting phase. In contrast, Fig 106a (bottom) shows that alumina additions produce secondary phases that are smaller and don't disrupt the local alignment or performance of the superconducting phase. Fig. 106b indicates the improvement in critical current density (J_c) performance resulting from alumina additions.
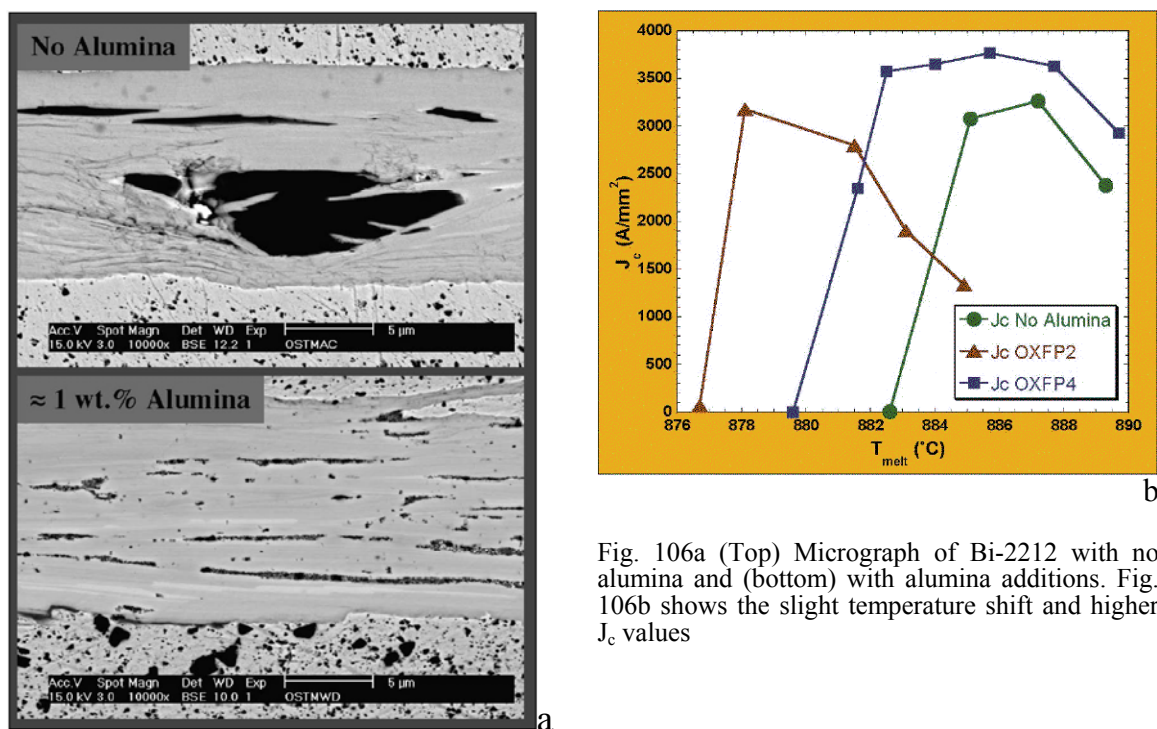
Fig. 106a (Top) Micrograph of Bi-2212 with no alumina and (bottom) with alumina additions. Fig. 106b shows the slight temperature shift and higher J_c values

We have also learned that the formation of (Mg,Cu)O impurity phases in tapes with AgMg substrates / sheaths, used to add mechanical strength, appears responsible for degradation in J_c. Fig. 107a shows evidence for Bi-2201 and Cu-free impurity phase content in the Bi-2212 matrix at the same time the (Mg,Cu)O particles are present. These effects are absent with a pure Ag sheath and substrate, Fig. 107b. Fig. 107c shows the presence of (Mg,Cu)O (Cu ≈ 10-15 at.%) particles at the sheath interface and within filaments. We believe that the problem can be fixed with CuO additions to starting

powder (in progress). With excess Cu in the powder, the Bi-2212 can remain on stoichiometry, resulting in fewer second phase particles and a higher J_c.
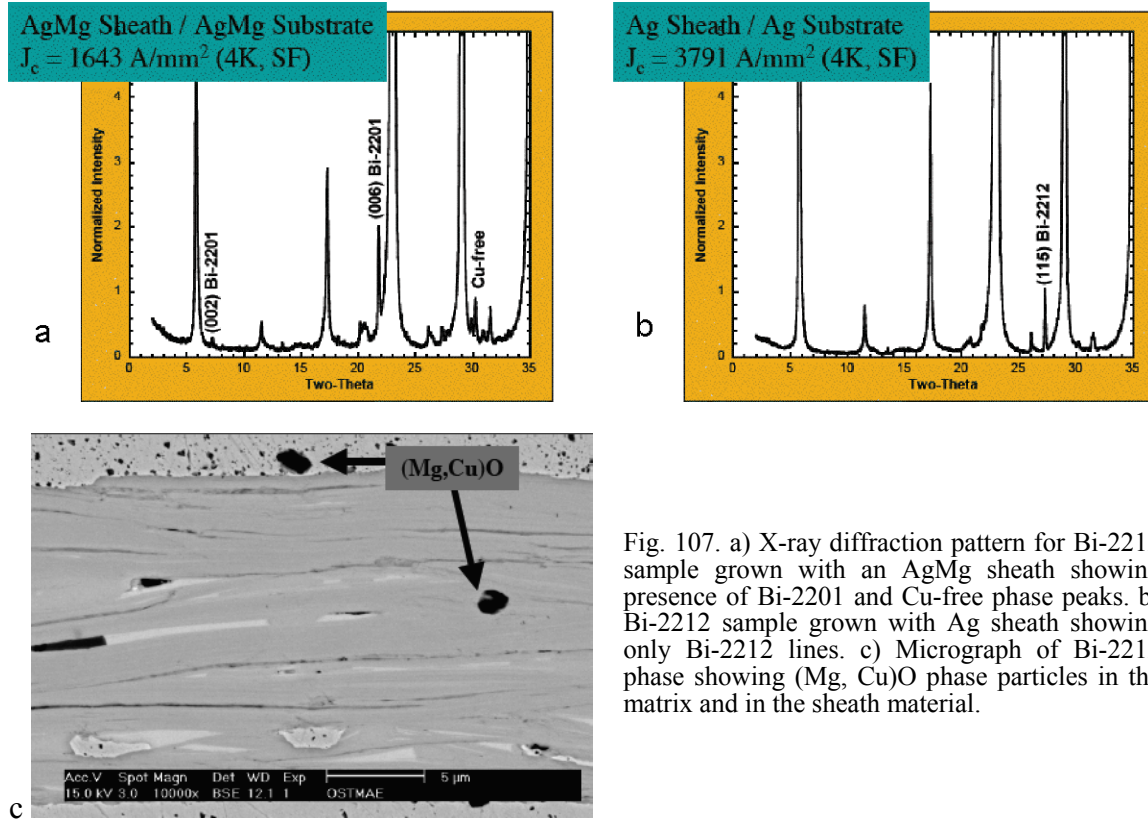
Fig. 107. a) X-ray diffraction pattern for Bi-2212 sample grown with an AgMg sheath showing presence of Bi-2201 and Cu-free phase peaks. b) Bi-2212 sample grown with Ag sheath showing only Bi-2212 lines. c) Micrograph of Bi-2212 phase showing (Mg, Cu)O phase particles in the matrix and in the sheath material.

Chemical analysis of the superconducting phase within fully processed tapes has helped to refine values for the starting powder compositions. We have found that all of the compositions of the Bi-2212 superconducting phase were Sr-rich and Ca deficient relative to the ideal composition: $Bi_{2.17}Sr_{2.02}Ca_{0.84}Cu_{1.97}O_y$. The starting powders that are close to this measured composition have produced the highest J_c values in the Bi-2212 tapes. Other compositions often show Bi-2201 layers and other fine intergrowths, Fig. 108.
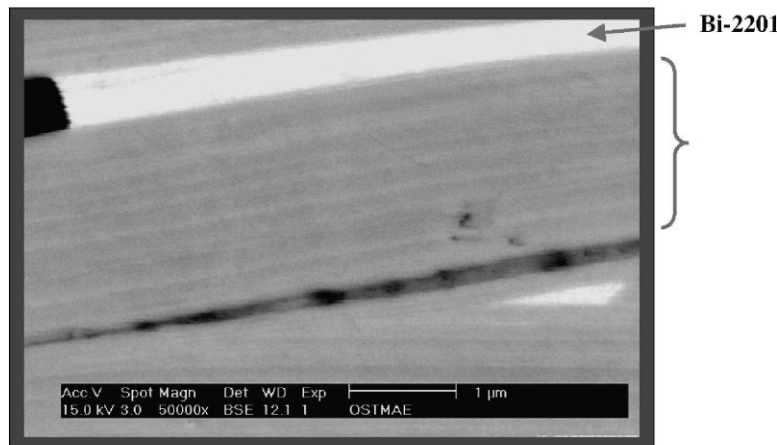
Fig. 108. Stoichiometries away from the ideal one for Bi-2212 often result in Bi-2201 intergrowths and other fine structures, indicated by the layers within the curly bracket.

91

Transport measurements in boiling liquid neon, 26.4 K in Los Alamos, were used to gather the J_c data needed for coil simulations and design for the open geometry MRI.

Values were determined on 2 mm wide patterned tape with results scaled to 1 cm wide, double sided tape (Fig. 109). Typical results were for I_c(26.4 K, sf) of about ~200 A, a power law exponent n of about 7.2 and good in field performance.
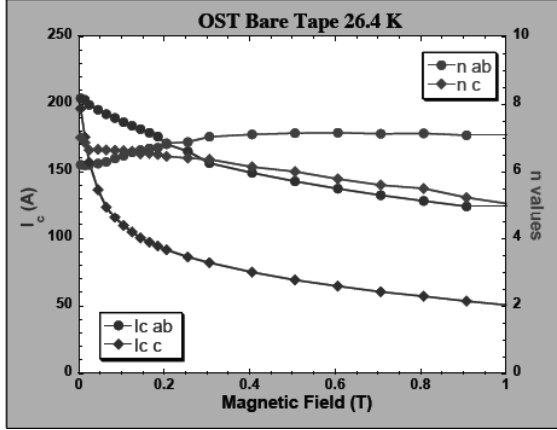
Fig. 109a. Critical current I_c and power law exponent n for OST bare tape as a function of magnetic field parallel to the ab plane and to the c axis.
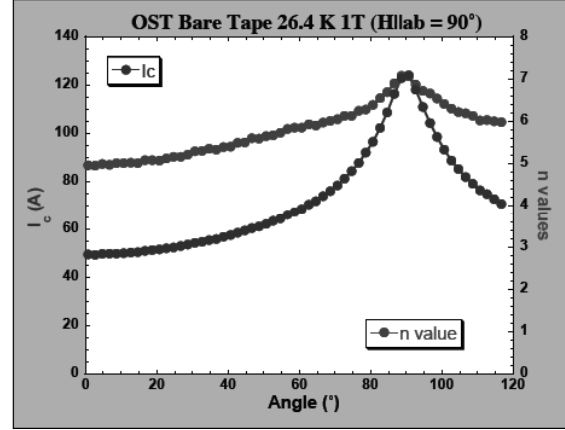
Fig. 109b. Critical current I_c and power law exponent n for OST bare tape as a function of angle at 1 T.

J_c measurements using a SQUID magnetometer and the Bean critical state model showed little J_c degradation with double layer tapes, Fig. 110. Two layer tapes can be used for doubling the critical current of the conductor. We found that the field and temperature dependence of one and two layer tapes are similar. Typically, J_c(4.3K) is approximately field independent, whereas J_c at 20 K and 26.5 K decreases exponentially with H. J_c(20 K) is about 15-20% of J_c(4.3K); J_c (26.5 K) ranges from 12% (at 1 kOe) to 2% (at 10 kOe) of the value of J_c(4.3K).
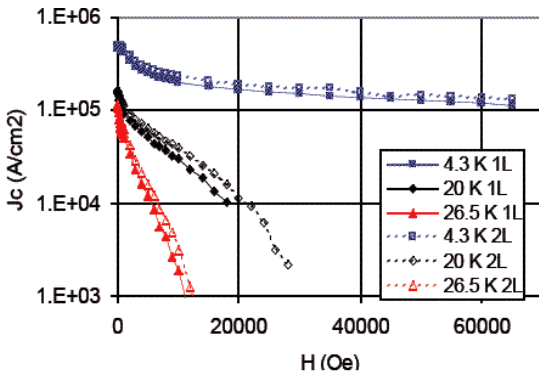
Fig. 110a. Magnetically determined critical current density J_c for OST single layer (1L) and double layer (2L) tape as a function of magnetic field parallel to the c axis.
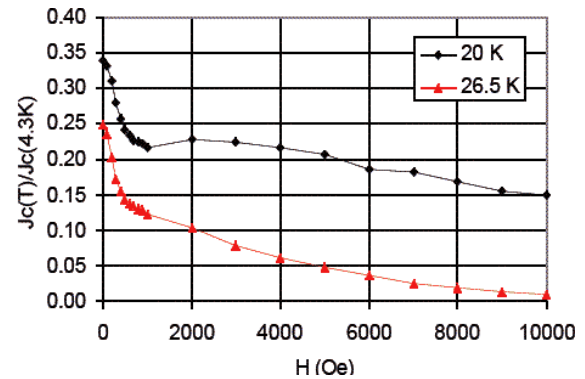
Fig. 110b. Magnetically determined normalized critical current density J_c for OST single layer tape as a function of magnetic field parallel to the c axis at two temperatures.

Work at NREL concentrated on techniques for increasing the J_c levels using MgO nanoparticle additions, as shown in Fig. 111. The MgO nanopaticles were mixed into the

Bi-2212 slurry before dip coating. The measurements were at self-field and at 4.2 K. The self-field data indicate that the optimum concentration of MgO nanoparticles is 0.5 wt%.
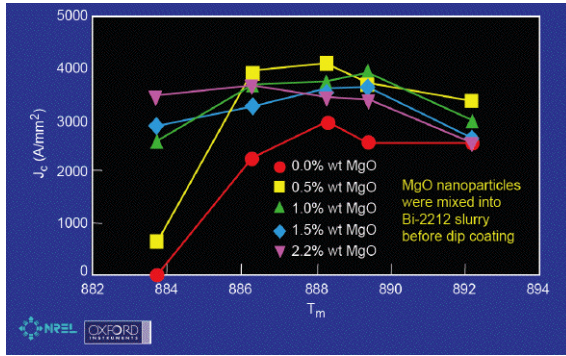
Fig. 111. Self-field measurements at 4.2 K of the critical current density of Bi-2212 tapes doped with MgO nanoparticles as a function of the melt processing temperature.

Measurements (Fig. 112) of the angular field dependence of the critical current density also show that the best J_c improvement in field is for 0.5 wt% additions. This is true relatively independent of the direction of the applied magnetic field.
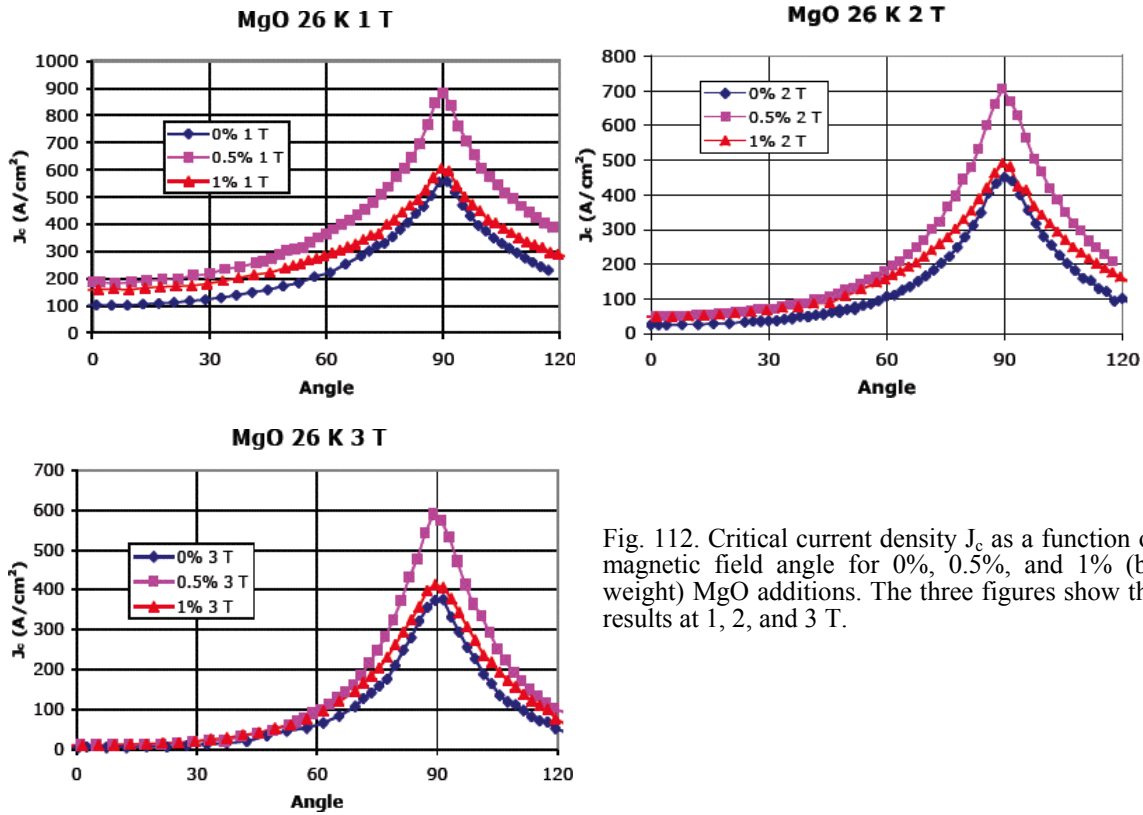
Fig. 112. Critical current density J_c as a function of magnetic field angle for 0%, 0.5%, and 1% (by weight) MgO additions. The three figures show the results at 1, 2, and 3 T.

In a slightly different process, 0.012 g/cm^2 of MgO nanoparticles were sprayed onto the surface of the dip-coated Bi-2212 tape. J_c shows an improvement for H∥c at 26 K with doping. This improvement over the undoped tape is by nearly a factor of 2 at 3 T, as shown in Fig. 113.
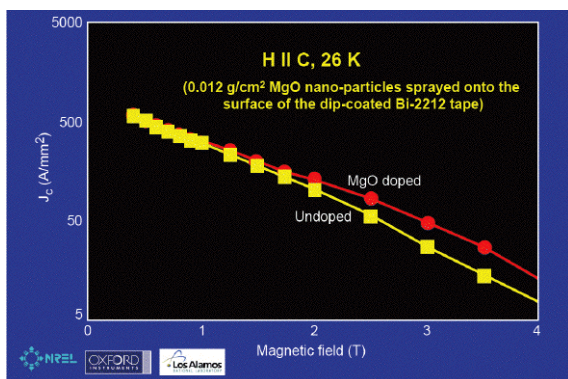
Fig. 114a. Transport critical current density as a function of applied field at 26 K for MgO doped and undoped samples.
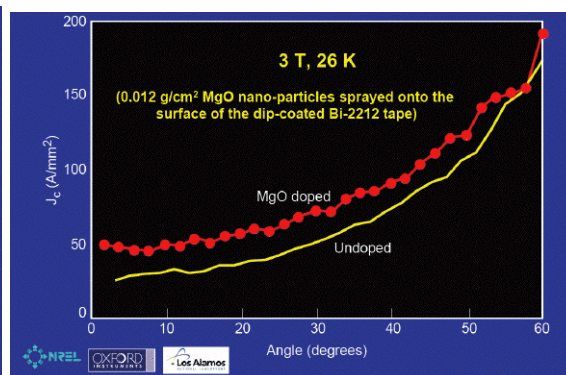
Fig. 114b. Transport critical current density as a function of angle at 26 K and 3 T for MgO doped and undoped samples.

TEM micrographs of MgO doped Bi-2212 tape show the presence of small (~300 nm) size MgO particles (Fig. 115, top). Analytical analyis (Fig. 115, bottom) also showed that the particles were consistent with MgO.
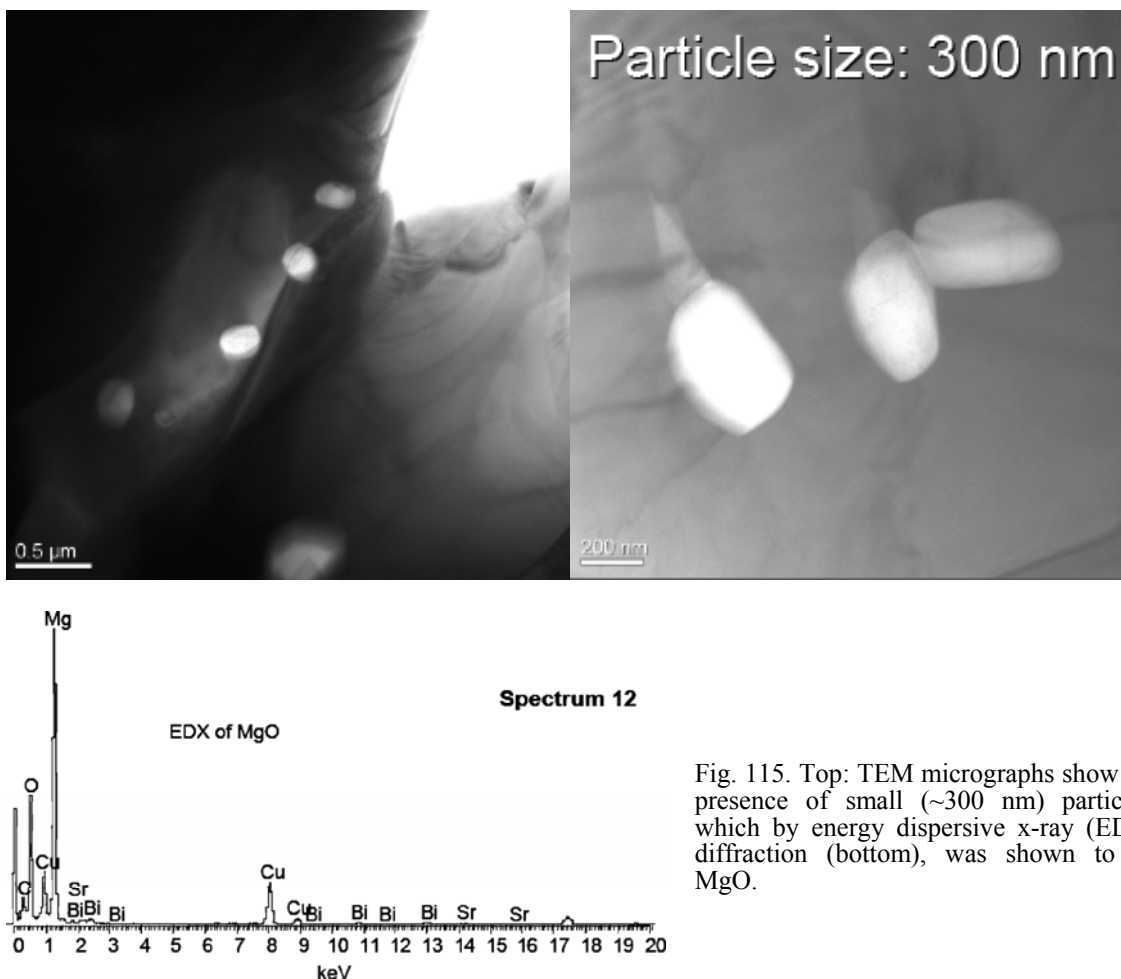
Fig. 115. Top: TEM micrographs show the presence of small (~300 nm) particles, which by energy dispersive x-ray (EDX) diffraction (bottom), was shown to be MgO.

Summarizing this effort on behalf of the Oxford open geometry MRI system, the national laboratories have played a significant role in optimizing the Bi-2212 wires by introducing

Al_2O_3 additions for secondary phase control and performance enhancement. Microstructural analysis has been used to provide compositional information and to optimize powder composition. Transport and magnetization measurements of the Bi-2212 conductor have been made to provide for temperature dependent performance benchmarks and conductor development. Finally, nano-phase MgO additions have been made for field performance (flux pinning) improvements.

Postscript: This project was ended for business reasons in July 2004 by mutual consent of Oxford Instruments (project leader) and Siemens (magnet/cryogenics/system integrator). Technically the project aim appears attainable, but the system economics did not warrant additional investment. A primary factor in this decision was the significant shift in the MRI market to higher field strengths since this project was proposed in 2000/2001.

3. Fiscal Year 2004 Publications

3.1. Journal Articles Published

Thickness dependence of ac losses in circular disks of $YBa_2Cu_3O_7$ films in perpendicular magnetic fields.
Suenaga, M; Li, Q; Ye, Z; Iwakuma, M; Toyota, K; Funaki, F; Foltyn, SR; Wang, H; Clem, JR
J. Appl. Phys.; v.95, no.1, p.208-13 (2004)

Angular-dependent vortex pinning mechanisms in $YBa_2Cu_3O_7$ coated conductors and thin films
Civale, L; Maiorov, B; Serquis, A; Willis, JO; Coulter, JY; Wang, H; Jia, QX; Arendt, PN; MacManus-Driscoll, JL; Maley, MP; et al.
Applied Physics Letters; v.84, no.12, p.2121-2123 (2004)

Systematic enhancement of in-field critical current density with rare-earth ion size variance in superconducting rare-earth barium cuprate films
MacManus-Driscoll, JL; Foltyn, SR; Jia, QX; Wang, H; Serquis, A; Maiorov, B; Civale, L; Lin, Y; Hawley, ME; Maley, MP;
Applied Physics Letters; v.84, no.26, p.5329-31 (2004)

Crossover of thickness dependence of critical current density Jc(T,H) in $YBa_2Cu_3O_{7-d}$ thick films.
Qiang Li; Suenaga, M.; Ye, Z.; Foltyn, SR; Wang, H.
Applied Physics Letters; v.84, no.18, p.3528-30 (2004)

Improving flux pinning in $YBa_2Cu_3O_7$ coated conductors by changing the buffer layer deposition conditions
B. Maiorov, H. Wang, P. N. Arendt, S. R. Foltyn and L. Civale
Ceramic Transactions v.160, 3 (2004).

Numerical modelling of a HTS cable in AC regime
Grilli, F; Stavrev, S; Dutoit, B; Spreafico, S; Tebano, R; Gomory, F; Frolek, L; Souc, J
IEEE Transactions on Applied Superconductivity; v.14, no.1, p.94-102 (2004)

Understanding high critical currents in $YBa_2Cu_3O_7$ thin films and coated conductors
Civale, L; Maiorov, B; Serquis, A; Willis, JO; Coulter, JY; Wang, H; Jia, QX; Arendt, PN; Jaime, M; MacManus-Driscoll, JL;
J. Low Temperature Physics; v.135, no.1-2, p.87-98 (2004)

Anisotropic scaling in $YBa_2Cu_3O_7$ crystals with columnar defects
Silhanek, AV; Civale, L
J. Low Temperature Physics; v.135, no.1-2, p.157-60 (2004)

Bose-glass-like phases in oriented-twin $YBa_2Cu_3O_{7-d}$ crystals
Maiorov, B; Osquiguil, E
J. Low Temperature Physics; v.135, no.1-2, p.131-4 (2004)

Role of beam divergence and ion-to-molecule flux ratio in ion-beam-assisted deposition texturing of MgO
Findikoglu, AT; Kreiskott, S; te Riele, PM; Matias, V
Journal of Materials Research; v.19, no.2, p.501-4 (2004)

Characteristics of alumina diffusion barrier films on Hastelloy
Usov, I; Arendt, P; Stan, L; DePaula, R; Wang, H; Foltyn, S; Dowden, P
Journal of Materials Research; v.19, no.4, p.1175-80 (2004)

Microstructure of $SrTiO_3$ buffer layers and its effects on superconducting properties of $YBa_2Cu_3O_7$ coated conductors
Wang, H; Foltyn, SR; Arendt, PN; Jia, QX; MacManus-Driscoll, JL; Stan, L; Li, Y; Zhang, X; Dowden, PC
Journal of Materials Research; v.19, no.6, p.1869-1875 (2004)

Biaxially textured IBAD-MgO templates for YBCO-coated conductors
Arendt, PN; Foltyn, SR
MRS Bulletin; v.29, no.8, p.543-550+537-538 (2004)

Magnetic field anisotropy measurements of J(c) and n-values for two YBCO coated conductor bridges
Coulter, JY; Civale, L; Willis, JO
Materials Research Society Symposium Proceedings; 2004; v.3, p.65-67 (2004)

Continuous preparation of pulsed laser deposited oxide buffer layers and YBCO for coated conductor applications
Gibbons, BJ; Kreiskott, S; Matias, V; Holesinger, TG; Coulter, JY
Materials Research Society Symposium Proceedings; v.3, p.9-11 (2004)

Recent Processing Advances for Increased J_c in $(Bi, Pb)_2Sr_2Ca_2Cu_3O_x$ Tapes
Y. Yuan, J. Jiang, X. Y. Cai, D. C. Larbalestier, E. E. Hellstrom, Univ of WI, T. G. Holesinger, MST-STC, Y. Huang, R. Parrela, American Superconductor, V. A. Maroni, Argonne Nat. Lab,
Transactions of the Materials Research Society of Japan, 29 [4] 1235-1239 (2004)

Strongly enhanced current densities in superconducting coated conductors of $YBa_2Cu_3O_{7-x}$ + $BaZrO_3$
Macmanus-Driscoll, JL; Foltyn, SR; Jia, QX; Wang, H; Serquis, A; Civale, L; Maiorov, B; Hawley, ME; Maley, MP; Peterson, DE
Nature Materials; v.3, no.7, p.439-443 (2004)

High critical current YBCO coated conductors based on IBAD MgO
Arendt, PN; Foltyn, SR; Civale, L; DePaula, RF; Dowden, PC; Groves, JR; Holesinger, TG; Jia, QX; Kreiskott, S; Stan, L;
Physica C; v.412-14, no.2, p.795-800 (2004)

Influence of crystalline texture on vortex pinning near the ab-plane in $YBa_2Cu_3O_7$ thin films and coated conductors
Civale, L; Maiorov, B; Serquis, A; Foltyn, SR; Jia, QX; Arendt, PN; Wang, H; Willis, JO; Coulter, JY; Holesinger, TG;
Physica C; v.412-14, no.2, p.976-982 (2004)

Improved critical currents in a Bi-2223/Ag coil using splayed columnar defects
Coulter, JY; Willis, JO; Maley, MP; Ullmann, JL
Physica C; v.412-14, no.2, p.1079-1084 (2004)

Numerical modelling of a HTS cable in AC regime
Grilli, F; Stavrev, S; Dutoit, B; Spreafico, S; Tebano, R; Gomory, F; Frolek, L; Souc, J
Physica C; 15 v.401, no.1-4, p.176-81 (2004)

Progress on MOD/RABiTS™ 2G HTS wire
    Rupich, MW; Zhang, W.; Li, X.; Kodenkandath, T.; Verebelyi, DT; Schoop, U.;
    Thieme, C.; Teplitsky, M.; Lynch, J.; Nguyen, N.; Siegal, E. ; Scudiere, J. ;
    Maroni, V. ; Venkataraman, K. ; Miller, D. ; Holesinger,TG
    Physica C; v.412-14, no.2, p.877-884 (2004)

Detection of interfacial strain and phase separation in $MBa_2Cu_3O_{7-x}$ thin films using
    Raman spectroscopy and X-ray diffraction space mapping.
    Venkataraman, K; Kropf, AJ; Segre, CU; Jia, QX; Goyal, A; Kang, BW;
    Chattopadhyay, S; You, H; Maroni, VA
    Physica C; v.402, no.1-2, p.1-16 (2004)

Thermodynamic properties of excess-oxygen-doped $La_2CuO_{4.11}$ near a simultaneous
    transition to superconductivity and long-range magnetic order
    G. A. Jorge, M. Jaime, L. Civale, C. D. Batista, B. L. Zink, F. Hellman, B.
    Khaykovich, M. A. Kastner, Y. S. Lee, and R. J. Birgeneau
    Physical Review B; v.69, no.17, p.174506 (2004).

Light-Induced Oxygen-Ordering in $(Y,Pr)Ba_2Cu_3O_{6.7}$: A Raman Spectroscopy
    Experiments and Monte Carlo Study
    S. Bahrs, A. Goni, C. Thomsen, TU Berlin, B. Maiorov, MST-STC, G. Nieva, A.
    Fainstein, CAB-CNEA
    Physical Review B; v.70, no.1, p.14512 (2004)

Magneto-optical Evidence for a Gapped Fermi Surface in Underdoped YBa2Cu3O6+x
    L. B. Rigal, D. C. Schmadel, D. Drew, B. Maiorov, E. Osquiguil, J. S. Preston, R.
    Hughes, and G. D. Gu
    Physical Review Letters; v.93, p.137002 (2004)

STEM Study on $YBa_2Cu_3O_{7-d}$ Seed Layer for the Growth of High Quality $EuBa_2Cu_3O_{7-d}$
    Films
    H. Wang, Y. Lin, S. R. Foltyn, P. N. Arendt, J. Driscoll, and Q. X. Jia.
    MST-STC, X. Liao. Univ of CH, X. Zhang, Huifang Xu of Univ. WI,
    Superconductor Science and Technology, v.201, p.2880-2885 (2004)

Modeling of coupling between superconductors of finite length using an integral
    formulation
    Bouzo, MC; Grilli, F; Yang, Y
    Superconductor Science & Technology; v.17, no.10, p.1103-12 (2004)

Prediction of resistive and hysteretic losses in a multi-layer high-Tc superconducting
    cable
    Grilli, F; Sjostrom, M
    Superconductor Science and Technology; v.17, no.3, p.409-416 (2004)

Reel-to-reel preparation of ion-beam assisted deposition (IBAD)-MgO based coated
    conductors
    Kreiskott, S; Arendt, PN; Coulter, JY; Dowden, PC; Foltyn, SR; Gibbons, BJ;
    Matias, V; Sheehan, CJ
    Superconductor Science & Technology; v.17, no.5, p. S132-4 (2004)

Nanoparticle Incorporated Superconductor Bi-2212 Tapes
> R. N. Bhattacharya, NREL, H. Miao, K. Marken, Oxford, J. Willis, MST-STC, P. Spagnol, NREL,
> Phys. Stat. Sol. v.201, no.13, p.2880-5 (2004)

Effect of mechanical deformation on the critical current in YBa2Cu3O7-b superconducting films
> Ibragimova, EM; Kalanov, MU; Kirk, MA; Foltyn, SR
> Technical Physics; v.49, no.4, p.512-515 (2004)

3.2. Journal Articles Submitted for Publication

The Effect of Growth Rates on the Microstructures of Europium Barium Copper Oxide Films on Strontium Titanate Substrates
> Y. Lin, H. Wang, S. R. Foltyn, Q. X. Jia, and M. E. Hawley
> Submitted to Applied Physics Letters.

RE Ion Effects and Enhanced Critical Current Densities in $Y_{2/3}Sm_{1/3}Ba_2Cu_3O_{7-x}$ Coated Conductors
> Judith L. Driscoll, Steve Foltyn, Boris Maiorov, Quanxi Jia, Haiyan Wang, Adriana Serquis, Leonardo Civale, Marty Maley, Dean Peterson, Marilyn Hawley
> Ibid.

Systematic Enhancement of In-Field Critical Current Density with Rare Earth Ion Size Variance in Superconducting Rare Earth Barium Cuprate Films
> Judith L. MacManus Driscoll, Steve R. Foltyn, Quanxi Jia, Haiyan Wang, Adriana Serquis, Boris Maiorov, Leonardo Civale, Yuan Lin, Marty Maley, Marilyn Hawley
> Ibid.

STEM Study on YBCO Seed Layer for the Growth of High Quality EuBCO Films
> H. Wang, Y. Lin, S. R. Foltyn, P. N. Arendt, J. Driscoll, and Q. X. Jia LANL; X. Liao. Univ of Chicago; X. Zhang, Huifang Xu, Univ. WI
> Ibid.

Crystallographic Orientation Dependence of Radiation Damage in Ar+ implanted YSZ and MgO Single Crystals
> I. O. Usov, P. N. Arendt, L. Stan, R. F. DePaula, MST-STC
> Ibid.

Effect of misalignment between the applied and internal magnetic fileds on th critical current of 'miscut' coated conductors
> B. A. Maiorov, L. Civale, B. J. Gibbons, V. Matias, T. G. Holesinger, S. Kreiskott
> Ibid.

Enhancement of Critical Current Density In Low Level A1-Doped MgB(2)
> A. Berenov, Cambridge, Adriana Serquis, Xiaozhou Liao, Yuntian Zhu, Dean Peterson, LANL; Y. Bugoslavsky Argentina, K.A. Yates, M.G. Blamire, Cambridge, L.F. Cohen, Imperial College, Judith L. Driscoll, Cambridge
> Ibid.

A Shell Model for the Structure of Bi-2223 Filaments in a Multifilamentary Conductors
T. G. Holesinger, J. A. Kennison; S. Liao, Y. Yuan, J. Jiang, X. Y. Cai, E. E. Hellstrom, D. C. Larbalestier, Univ. of WI; R. M. Baurceanu, V. A. Maroni, ANL, Y. Huang, AMSC
Submitted to IEEE Trans. Appl. Supercond.

Critical Currents Ic(77K) > 350 A/cm-Width Achieved in ex situ YBCO Coated Conductors Using A Faster Conversion Process
R. Feenstra, A.A. Gapud, F. A. List, E. D. Specht D. K. Christen, ORNL, T. G. Holesinger, LANL; D.M. Feldmann, Univ. Wisconsin
Ibid.

Long Term Anneal Study and Composition Variation for Reducing residual Bi-2212 in Bi-2223 Wires
J. Jiang, X.Y. Cai, Y. Yuan, E.E. Polyanski, E.E. Hellstrom, D.C. Larbalestier, Univ. of WI, V.A. Maroni, ANL; T.G. Holesinger, LANL; and Y. Huang, AMSC
Ibid.

Continuous Fabrication of IBAD-MgO Based Coated Conductors
V. Matias, B.J. Gibbons, A.T. Findikoglu, P.C. Dowden, J.J. Sullard, and J.Y. Coulter
Ibid.

Optimazion of Critical Currents in MgB_2 Wires and Coils
A. C. Serquis, Argentina, L. Civale, D. L. Hammon. LANL; G. Serrano, Argentina, and V. F. Nesterenko, Univ. of CA, San Deigo
Ibid.

Influence of Tilted Geometries on Critical Current in Superconducting Thin Films
Boris Maiorov, Leonardo Civale, Brady Gibbons, Sasha Kreiskott, Vladimir Matias, Quanxi Jia, and Terry Holesinger
Ibid.

Identification of intrinsic ab-plane pinning in YBaCuO thin films and coated conductors
L. Civale, B. A. Maiorov, J. L. MacManus-Driscoll, H. Wang
Ibid.

Microstructual Study of Europium Barium Copper Oxide Films by High-Resolution X-Ray Diffraction
Y. Lin, H. Wang, P. Arendt, S. R. Foltyn, Q. X. Jia, M. Hawley
Ibid.

Comparative Study of REBaCuO Films for Coated Conductors
Q. X. Jia, B. A. Maiorov, H. Wang, Y. Lin, S. R. Foltyn, L. Civale, and J. L. MacManus-Driscoll
Ibid.

Natural Correlated Inclined Defects in DyBaCuO
Boris A. Maiorov, Brady J. gibbons, Yuan Lin, Yuan Li, Quanxi X. Jia, Leonardo Civale
Submitted to MRS Bulletin

Comparative Study of Microstructural Properties for Yttrium Barium Copper Oxide
Films on Single Crystal and Nickel-Based Metal Substrates
Y. Lin, H. Wang, P. Arendt, S. R. Foltyn, Q. X. Jia, M. Hawley, C. J. Wetteland
Submitted to Journal of Applied Physics

Liquid Mediated Growth and the Bi-Model Microstructure of Yba(2)CU(3)O(7-a) Films
Made by the Ex Situ Conversion of PVD-BaF(2) Precursors
T. G. Holesinger, P. N. Arendt, MST-STC, R. Feenstra, A. A. Gapud, E. D.
Specht, ORNL, D. M. Feldmann, D. C. Larbalestier, Univ. of WI
Submitted to Journal of Materials Research.

Thickness Effects of $SiTiO_3$ Buffer Layers on Superconducting Properties of YBaCuO
Coated Conductors
H. Wang, S. R. Foltyn, P. N. Arendt, Q. X. Jia, Y. Li, and X. Zhang
Ibid.

Microstructure of $SrTiO_3$ Buffer Layers and its Effects on Superconducting Properties of
YBCO Coated Conductors
Haiyan Wang, Steve Foltyn, Paul Arendt, Quanxi Jia, LANL; Judith MacManus
Driscoll, Univ. of Cambridge
Ibid.

Biaxially Textured YBCO/IBAD-MgO Coated Conductors
Paul Arendt, Steve R. Foltyn, MST-STC
Submitted to the MRS Bulletin, August 2004 Issue.

Recent Processing Advances for Increased Jc in Bi-2223 Tapes
Y. Yuan, J. Jiang, X. Y. Cai, D. C. Larbalestier, E. E. Hellstrom, Univ of WI, T.
G. Holesinger, LANL; Y. Huang, R. Parrela, AMSC, V. A. Maroni, ANL
Submitted to Transactions of the Materials Research Society of Japan.

Improving Flux Pinning in Yba2Cu307 Coated Conductors By Changing the Buffer
Layer Deposition Conditions
B. A. Maiorov, H. Wang, S. R. Foltyn, P. N. Arendt, L. Civale, MST-STC
Submitted to the 106th American Ceramic Society Meeting Proceedings,
Indianapolis, IN, 4/18-21/04.

Light-Induced Oxygen-Ordering in $(Y,Pr)Ba_2Cu_3O_{6.7}$: A Raman Spectroscopy
Experiments and Monte Carlo Study
Sabine Bahrs, Alejandro Goni, Christian Thomsen, TU Berlin, Boris Maiorov,
LANL; Gladys Nieva, Alejandro Fainstein, CAB-CNEA
Submitted to Physical Review B.

Large Field Generation with Hot-Isostatically-Pressed Powder-in-Tube MgB_2 Coil at 25
K
A. Serquis, L. Civale, Y. Coulter, D. Hammon, X. Liao, Y. Zhu, D. Peterson, F.
Mueller, LANL; V.R. Nesterenko, S.S. Indrakanti, University of California
Submitted to Superconductor Science and Technology (Rapid Communication)

Nanoparticle Incorporated Superconductor Bi-2212 Tapes
Raghu N. Bhattacharya, NREL, Hanping Miao, Ken Marken, Oxford, Jeffrey
Willis, LANL, Priscila Spagnol, NREL
Submitted to Superconductor Science and Technology.

Detection of Interfacial Strain and Phase Separation in Mba(2)Cu(3)O(7-x) Thin Films
Using Raman Spectroscopy and X-Ray Diffraction Space Mapping
K. Venkataraman, A.J. Kropf, ANL, C.U. Segre, Illinois, Quanxi Jia, MST-STC,
A. Goyal, ORNL
Submitted to Physica C.

Effect of Mechanical Deformation on the Critical Current of Superconducting YBCO
Films
E.M. Ibragimova, M.U. Kalanov, Uzbekistan, M.A. Kirk, ANL, Steve R. Foltyn,
LANL
Submitted to the Journal of Technical Physics.

3.3. Other Publications and Conference Abstracts

Channeling Study of Radiation Damage in (100), (110) and (111) MgO Single Crystals
I. O. Usov, P. N. Arendt, L. Stan, R. F. DePaula
Abstract submitted to 18th international Conference on Application of
Accelerators in Research & Industry, Ft. Worth, TX, 10/9-16/04

Ion Beam Assisted Deposition of Biaxially Textured MgO Thin Films as Template for
High Temperature Superconducting Coated Conductors
Liliana Stan
Abstract for talk presented at the University of New Mexico, 11/12/04

Development of High temperature Superconducting Wire in the United States
Dean E. Peterson
Abstract submitted to ISS 2004 Conf. Niigata, Japan 11/15-30/04

Optimization of IBAD Coated Conductors
Dean E. Peterson
Abstract submitted to ISS 2004 Conf. Niigata, Japan 11/15-30/04

Making Useful High Temperature Superconducting Coatings
Vladimir Matias
Abstract submitted to Korea Electrotechnical Research Institute, Seoul Changwon
South Korea 11/24-12/2/04

Effect of the misalignment between the applied and internal magnetic fields on the
critical currents in tilted superconducting thin films
B.A. Maiorov, L. Civale, B.J. Gibbons, V. Matias, T.G. Holesinger, Q.X. Jia, S.
Kreiskott
Abstract submitted to APS March Meeting Los Angeles, CA 3/21-25/04

Matching Field Effect in the Critical Current of YBaCuO Films Due to Periodic
Y_2BaCuO_5 Inclusions
B. A. Maiorov, L. Civale, T. G. Holesinger LANL; T. Haugan, P. N. Barnes
WPAFB
Abstract submitted to 2005 MRS Spring Meeting, San Francisco, CA 3/28-
4/1/2005.

Understanding and Improving Vortex Pinning in REBaCuO Thin Films and coated
      Conductors
      L. Civale, B. A. Maiorov, H. Wang, S. R. Foltyn, P. N. Arendt, T. G. Holesinger,
      Q. X. Jia, B. J. Gibbons, V. Matias, LANL; J. L. MacManus-Driscoll Cambridge,
      and A. Serquis
      Ibid.

Microstructures of Europium Copper Oxide Films on Strontium Titanate Substrates with
      Different Seed Layers
      Y. Lin, H. Wang, L. Civale, Y. Li, S. R. Foltyn, J. L. MacManus-Driscoll, Q. X.
      Jia, and B. A. Maiorov MST-STC
      Ibid.

YBCO/IBAD Mgo Coated Conductors - Functionality of Template Architecture and
      recent Processing Improvements
      P. N. Arendt, S. R. Foltyn, Q. X. Jia, R. F. DePaula, T. G. Holesinger, J. R.
      Groves, L. Stan, I. Usov, and H. Wang
      Ibid.

Overcoming the Barrier to 1000 A/cm-Width Coated Conductors
      S. F. Foltyn, H. Wang, Q. X. Jia, P. N. Arendt, L. Civale, B. A. Maiorov, J. L.
      MacManus-Driscoll, Y. Li, and M. P. Maley
      Ibid.

Techniques for Substrate Temperature Monitoring and Control During Stationary and
      Continuously Processed Ion Beam Assited Deposited Magnesium Oxide
      R. F. DePaula, P. N. Arendt, J. R, Groves, L. Stan, and I. Usov
      Ibid.

Influence of the Substrate Temperature on the Texture of MgO Films Grown by Ion
      Beam Assisted Deposition
      L. Stan, P. N. Arendt, R. F. DePaula, I. Usov, and J. R. Groves
      Ibid.

Vortex Pinning Mechanisms in REBaCuO Thin Films and Coated Conductors
      Leonardo Civale, Boris A. Maiorov, Adriana C. Serquis, Haiyan Wang, Stephen
      R. Foltyn, Quanxi Jia, Paul N. Arendt, Jeffrey O. Willis, James Y. Coulter, Judith
      L. MacManus-Driscoll, Marcelo Jaime
      Abstract submitted to Condensed Matter and Materials Physics Conference
      (CMMP04), April 4-7, 2004

Superconducting Films with High Critical Current Density for Coated Conductors
      Quanxi Jia, Steve Foltyn, Paul Arendt, Leonardo Civale, Haiyan Wang, Yuan Lin,
      Marilyn Hawley
      Abstract submitted to the 106th Annual Meeting of the American Ceramic Society
      in Indianapolis, Indiana, April 18-21, 2004.

Chemical Routes to Increasing Low Field and High Field Pinning in Epitaxial REBaCuO
      on Ion Beam Assisted Deposition Coated Conductors
      Judith L. Macmanus-Driscoll, Steve Foltyn, Quanxi Jia, Haiyan Wang
      Ibid.

Development of IBAD Coated Conductors
Dean E. Peterson, MST-STC
Abstract submitted to the International DAPAS Workshop, Gveongiu, South
Korea, April 19-23, 2004

Microstructural Study of Europium Barium Copper Oxide Films by High-Resolution X-
Ray Diffraction
Yuan Lin, Haiyan Wang, Steve E. Foltyn, Quanxi X. Jia, Marilyn E. Hawley,
Abstract submitted to the Applied Superconducting Conference, Jacksonville, FL,
10/3-8/04.

AC Loss Reduction Techniques in Coated Conductors
Steve Ashworth
Ibid.

Comparative Study of RE123 Films for Coated Conductors
Q. X. Jia, B. A. Maiorov, H. Wang, Y. Lin, S. R. Foltyn, and L. Civale
Ibid.

Analysis of Magnetic Field and Geometry Effects in the Design of HTS Devices for AC
Power Applications
F. Grilli, MST-STC, L. Martini, Italy, B. Dutoit, S. Stavrev, Switzerland, R.
Brambilla, Italy
Ibid.

Continuous Fabrication of IBAD-MgO Based Coated Conductors
Vladimir Matias, Brady J. Gibbons, Sascha Kreiskott, Paul Dowden, John J.
Sullard
Ibid.

Phase Equilibria in the SrO-CuO-TiO(2) System; Application to High-Temperature
Superconductors (HTS) Via Chemical Solution Deposition (CSD)
A. Ayala, T. G. Holesinger, LANL; W. Wong-Ng, L. P. Cook, NIST
Ibid.

Processing Advances for Ag-Sheathed (Bi,Pb)(2)Ca(2)Cu(3)O(x)
Yongwen Yuan, Xueyu Cai, Jianyi Jiang, David Larbalestier, Eric Hellstrom,
University of Wisconsin; Yibing Huang, AMSC; Vic Maroni, ANL; Terry
Holesinger, LANL
Ibid.

Correlated Pinning along the ab-Planes in Re-123 Thin Films and Coated Conductors
Leonardo Civale, Boris Maiorov, Haiyan Wang, Quanxi Jia, Judith Driscoll, Steve
Foltyn, Paul Arendt, Adriana Serquis
Ibid.

A Shell Model for the Structure of a Bi-2223 Filament in a First Generation
Terry Holesinger, Jack Kennison, MST-STC, Y. Huang, J. Jiang, X. Cai, Eric
Hellstrom, D. Larbalestier, Wisconsin, Vic Maroni, ANL
Ibid.

Compositional Analysis of the Bi-2212 Phase in High-Ic, Jc Bi-2212 Conductors
T.G. Holesinger, J.A. Kennison, MST-STC, K.R. Marken, H. Miao, M. Meinesz,
Oxford, S. Campbell, SCI
Ibid.

Nano-Structured MOD YBCO Films with Improved Flux Pinning
D. T. Verebelyi, U. Schoop, C.L. H. Thieme, J. Scudiere, AMSC, L. Civale, T. Holesinger
Ibid.

Grain Boundary Over Growth in ex-situ YBCO Coatings (BaF$_2$ Process) on RABiTS and IBAD Templates: Potential Mechanism to Improve Texture and Jc
D.M. Feldmann, D. C. Larbalestier, UW, R. Feenstra, A.A. Gapud, ORNL, T.G. Holesinger, LANL
Ibid.

Microstructural Development in High-Jc (Ic) YBCO Coated Conductors Based on ex-situ YBCO Conversion Processes
Terry Holesinger, Leonardo Civale, Yates Coulter, LANL; W. Zhang, X. Li, T. Kodenkandath, D.T. Verebelyi, M. W. Rupich, AMSC; D.M. Feldmann, S.I. Kim, D.C. Larbalestier, Wisconsin, R. Feenstra, A.A. Gapud, E.D. Specht, ORNL
Ibid.

Optimization of Critical Currents in MgB$_2$ PIT Wires and Coils
A.C. Serquis, Leonardo Civale, Xiaozhou Liao, D. L. Hammon, Y. T. Zhu, D. E. Peterson, F.M. Mueller, J. Driscoll, Vitali F. Nesterenko, Univ. of California
Ibid.

Recent Progress in Thickness Related Studies to Enhance Ic In ex situ YBCO Coated Conductors
R. Feenstra, A.A. Gapud, C. Cantoni, S.K. Christen, ORNL, D.M. Feldmann, D.C. Larbalestier, Wisconsin, T.G. Holesinger, M.W. Rupich, AMSC, A. Palau, T. Puig, ICMAB
Ibid.

Temperature and Magnetic Field Dependence of Critical Currents in YBCO Coated Conductors with Processing-Induced Variations in Pinning Properties
A.A. Gapud, R. Feenstra, D.K. Christen, ORNL, T.G. Holesinger, M.W. Rupich, AMSC
Ibid.

Addition of ultra-high density nanoparticle dispersions to enhance flux pinning of YBCO thin films
T.J. Haugan, P.N. Barnes, T.A. Campbell, J.M. Evans, J. W. Kell, L.B. Brunke, J.P. Murphy, J.C. Tolliver, C.V. Varanasi, I. Maartense- AFRL; L. Civale, and B.A. Maiorov- LANL; W. Wong-Ng, L.P. Cook- NIST
Ibid.

4. Patent and License Activity (April 1988 to September 2004)

4a. Invention Disclosures and Patent Applications

Designation	Date	Subject	Submitted by
DOE 94,720	7/13/00	Apparatus for Heating a Moving Tape	S. R. Foltyn, P.C. Dowden
DOE S-97,787 S.N. 10/208,086	Filed 7/29/02	Dual Ion Beam Assisted Deposition of Biaxially Textured Template Layers	James Groves Paul N. Arendt
DOE S-97,795 S.N. 10/209,391	Filed 7/31/02	Multilayer Composites and Manufacture of Same	T.G. Holesinger, Q.X. Jia
DOE S-97,803 S.N. 10/161,132	Filed 5/29/02	Reduced AC Losses in HTS Coated Conductors	S.P. Ashworth
DOE S-99,943 S.N. 10/242,895	Filed 9/11/02	Buffer Layers on Metal Alloy Substrates for Superconducting Tapes	Q.X. Jia, S.R. Foltyn, P.N. Arendt, J.R. Groves
DOE S-99.947 S.N. 10/456,639	Disclosed 9/10/02 Filed 6/5/03	Processing of High Density MgB_2 Wires by Hot Isostatic Pressing	Y.T. Zhu, A. Serquis, D. Hammon, L. Civale, X.Z. Liao, F.M. Mueller, D.E. Peterson, V. Nesterenko, Y. Gu
DOE S-99.952 S.N. 10/624,350	Disclosed 9/16/02 Filed 7/21/03	Use of High Current Density Electropolishing for the Preparation of Very Smooth Substrate Tapes for Coated Conductor Applications	S. Kreiskott, V. Matias, P.N. Arendt. S.R. Foltyn
DOE S-100,536 S.N. 10/624,348	Filed 7/21/03	Simplified Biaxially Textured Composite Substrates	James Groves, Paul Arendt, Stephen Foltyn, Sankar Sambasivan
DOE S-100,550 S.N. 10/321,156	Filed 12/17/02	Superconducting Structure	Chuhee Kwon, Quanxi Jia, Stephen R. Foltyn
DOE S-100,556 S.N. 60/483,146	Filed 6/26/03	Underground Radio	David Reagor, Jose Vasquez-Dominquez
DOE S-100,564 S.N. 10/624,855	Filed 7/21/03	Buffer Layer for Thin Film Structures	Stephen Foltyn, Quanxi Jia, Paul Arendt, Haiyan Wang
DOE S-100,569 S.N. 10/359,808	Filed 2/7/03	Substrate Structure for Growth of Highly Oriented and/or Epitaxial Layers	Paul Arendt, Stephen Foltyn, James Groves, Quanxi Jia
DOE S-100,586 S.N. 10/387,952	Filed 3/13/03	High Temperature Superconducting Thick Films	Paul N. Arendt, Stephen R. Foltyn, James R. Groves, Terry G. Holesinger, Quanxi Jia
DOE S-100,600	Disclosed 4/8/03	Magnetic Infrasound Sensor	Frederick Mueller, Lawrence Bronisz, Holger Grube, David Nelson, Jonathon Mace

Designation	Date	Subject	Submitted by
DOE S-100,631 S.N. 10/888,868	**Disclosed 8/03 Filed 7/8/04**	**Polymer-assisted deposition of films**	**T.M. McCleskey, A.K. Burrell, Q.X. Jia, Y. Lin**
DOE S-100,663 S.N. 10/925,479	**Disclosed 9/5/03 Filed 8/25/04**	**Enhanced Pinning in Mixed RE-123 Films with Low Variance and Specific Ionic Radius**	**Judith Driscoll Stephen Foltyn**
DOE S-100,664	Disclosed 9/5/03	Balanced Inductance Current Limiter	Stephen Ashworth
DOE S-100,667 S.N. 10/900,639	**Disclosed 9/5/03 Filed 7/24/04**	**Enhanced Pinning in YBCO Films with BaZrO$_3$ Nanoparticles**	**Judith Driscoll Stephen Foltyn**
DOE S-102,337	**Disclosed 2004**	**Method for Improving the Critical Current Density of thick YBCO Coatings**	**Stephen Foltyn, Quanxi Jia, Haiyan Wang**
DOE S-102,368	**Disclosed 2004**	**Superconducting Current Controller**	**Stephen P. Ashworth**
DOE S-102,393	**Disclosed 2004**	**Method For Improving Performance Of High-Temperature Superconductors in a Magnetic Field**	**Haiyan Wang, Boris Maiorov, Stephen R Foltyn, Leonardo Civale**
DOE S-104,805	**Disclosed 2004**	**Simplified Architecture for Coated Conductors**	**Stephen R. Foltyn, Paul N. Arendt, Haiyan Wang, Liliana Stan**
DOE S-104,806	**Disclosed 2004**	**High-Rate Buffer Layer for IBAD MgO Coated Conductors**	**Stephen R. Foltyn, Quanxi Jia, Paul N. Arendt**

4b. Patents Granted

Designation	Date	Subject	Issued to	Status
DOE S-63,245 S.N. 07/041,950 US Pat.4,784,686	Filed 04/24/87 Issued 11/15/88	Synthesis of Ultrafine Powders by Microwave Heating	T.T. Meek H. Sheinberg R.D. Blake	Expired 05/15/00
DOE S-68,033 S.N. 07/454,607 US Pat. 5,008,622	Filed 12/21/89 Issued 04/16/91	Superconductive Imaging Surface Magnetometer	W.C. Overton, Jr D. van Hulsteyn E.R. Flynn	Expired 10/16/98
DOE S-68,041 S.N. 07/330,329 US Pat 5,006,672	Filed 03/29/89 Issued 04/09/91	Apparatus for Storing High Magnetic Fields Having Reduced Mechanical Forces and Reduced Magnetic Pollution	M.L. Prueitt F.M. Mueller J.L. Smith	Maint. Fee 3 paid 10/09/02
DOE S-68,042	Filed	Detection of Surface	D.W. Cooke	Expired

Designation	Date	Subject	Issued to	Status
S.N. 07/276,188 US Pat 4,873,444	11/23/88 Issued 10/10/89	Impurity Phases in HTS Using Thermally Stimulated Luminescence	M.S. Jahan	10/10/97
DOE S-68,086 S.N. 07/311,998 US Pat 4,992,696	Filed 02/17/89 Issued 02/12/91	Apparatus Having Reduced Mechanical Forces for Supporting High Magnetic Fields	M.L. Prueitt F.M. Mueller J.L. Smith	Maint. Fee 3 paid 08/12/02
DOE S-68,098 S.N. 07/324,264 US Pat 5,015,952	Filed 03/14/89 Issued 05/14/91	Apparatus for Characterizing Conductivity of Materials by Measuring the Effect of Induced Shielding Currents Therein	J.D. Doss	Expired 05/14/99
DOE S-71,082 S.N. 07/671,231 US Pat 5,102,863	Filed 03/19/91 Issued 04/07/92	Process for Producing Clad Superconducting Materials	R.B. Cass K.C. Ott D.E. Peterson	Expired 10/07/99
DOE S-71,084 S.N. 07/670,111 US Pat 5,134,360	Filed 03/15/91 Issued 07/28/92	Apparatus and Method for Critical Current Measurements	J.A. Martin R.C. Dye	Expired 01/28/00
DOE S-72,816 S.N. 07/690,725 US Pat 5,268,646	Filed 04/24/91 Issued 12/07/93	Apparatus & Method for Characterizing Conductivity of Materials	J.D. Doss	Maint. Fee 2 due 06/07/05
DOE S-72,851 S.N. 07/860,337 US Pat. 5,238,913	Filed 03/30/92 Issued 08/24/93	Superconducting Microcircuitry by the Microlithographic Patterning of Superconducting Compounds and Related Materials	N.V. Coppa	Expired 08/24/01
DOE S-72,861 S.N. 813,726 US Pat 5,262,394	Filed 12/27/91 Issued 11/16/93	Superconductive Compositions Including Cerium Oxide Layer	X.D. Wu R. Muenchausen	Maint. Fee due 05/16/05
DOE S-72,880 S.N. 07/774,748 US Pat 5,278,138	Filed 10/11/91 Issued 01/11/94	Aerosol Chemical Vapor Deposition of Metal Oxide Films	K.C. Ott T.T. Kodas	Maint. Fee due 07/11/05
DOE S-72,898 S.N. 814,355 US Pat 5,252,551	Filed 12/27/91 Issued 10/12/93	Superconductive Articles	X.D. Wu, R.E. Muenchausen	Maint. Fee due 04/12/05
DOE S-72,899 S.N. 813,727 US Pat 5,270,294	Filed 12/27/91 Issued 12/14/93	Free-Standing Superconductive Articles	X.D. Wu, R.E. Muenchausen	Maint. Fee due 06/14/05
DOE S-75,023 S.N. 08/419,485	Filed 03/31/94	Substrate Heater for Thin Film Deposition	S.R. Foltyn	Maint. Fee due

Designation	Date	Subject	Issued to	Status
US. Pat 5,554,224	Issued 09/10/96			03/10/04
DOE S-75,081 S.N. 08/067,911 US Pat 5,300,486	Filed 05/27/93 Issued 04/06/94	Synthesis of BiPbSrCaCuO Superconductor	W.L. Hults, K.A Kubat-Martin, K.V. Salazar, D.S. Phillips, D.E. Peterson	Maint. Fee due 10/05/05
DOE S-78,394 S.N. 08/419,485 US Pat. 5,569,641	Filed 04/10/95 Issued 10/29/96	Preparation of Superconducting Bi-2223 Wire	M.G. Smith J.O. Willis D.E. Peterson	Maint. Fee due 04/29/04
DOE S-80,400 S.N. 08/168,331 US Pat 5,434,128	Filed 12/17/93 Issued 07/18/95	Superconducting Wire	D.A. Korzekwa J.F. Bingert D.E. Peterson H. Sheinberg	Maint. Fee due 01/18/07
DOE S-82,620, S.N. 08/425,752 US Pat. 5,872,080	Filed 04/19/95 Issued 02/16/99	High Temperature Superconducting Thick Films	P.N. Arendt X.D. Wu S.R. Foltyn	Maint. Fee 1 due 08/16/06
DOE S-82,623 S.N. 08/608,069 US Pat. 5,958,842	Filed 02/28/96 Issued 09/28/99	Melt Processing of Superconductors Using Alumina	T.G. Holesinger	Maint. Fee 1 due 03/28/07
DOE S-82,633 US Pat. 5,726,848	Filed 05/8/96 Issued 3/10/98	Fault Current Limiter and Alternating Current Circuit Breaker	H.J. Boenig	Maint. Fee due 09/10/05
DOE S-84,942 S.N. 08/597,061 US Pat. 5,908,812	Filed 02/05/96 Issued 06/01/99	Structure for HTS Composite Conductors & Manufacture of Same	J.D. Cotton G.N. Riley	Maint. Fee due 12/01/06
DOE S-84,965 S.N. 08/865,827 US Pat.5,820,678	Filed 09/23/96 Issued 10/13/98	Solid Source MOCVD Delivery System	B.N. Hubert X.D. Wu	Maint. Fee due 04/13/06
DOE S-89,600 S.N. 60/074,717 S.N. 09/249,476 US Pat. 6,195,870	Filed 2/13/98 Filed 02/12/99 Issued 3/6/01	Compressive Annealing of BSCCO-2223 Superconductive Tapes	Y.T. Zhu, P.S. Baldonado, J.F. Bingert, T.G. Holesinger, D.E. Peterson	Maint. Fee due 3/06/04
DOE S-91,761 S.N. 60/213,111 S.N. 09/867,842 US Pat. 6,383,989	Filed 6/21/00 Filed 5/29/01 Issued 5/7/02	Architecture for High Critical Current Superconducting Thick Films	Q.X. Jia S.R. Foltyn T.G. Holesinger	
DOE S-89,624 S.N. 08/942,038 US Pat. 6,428,635	Filed 10/1/97 Issued 8/6/02	Substrates for Superconductors	L.G. Fritzemeier, E. Thompson, E. Siegel, C. Thieme, R.D. Cameron, J.L. Smith, W.L. Hults	Maint. Fee due 8/6/05

Designation	Date	Subject	Issued to	Status
DOE S-89,678 S.N. 09/152,813 US Pat. 6,541,136	Filed 9/14/98 Issued 4/1/03	Superconducting Structure	C. Kwon, Q.X. Jia, and S.R. Foltyn	Maint. Fee due 10/1/06
DOE S-89,679 S.N. 60/100,215 S.N. 09/787,224 US Pat. 6,602,588	Filed 9/14/98 Filed 3/14/01 Issued 8/5/03	Superconducting Structure Including Mixed Rare-Earth Barium Copper Oxide Compositions	C. Kwon, Q.X. Jia, S.R. Foltyn, J.L. Smith, W.L. Hults, E.J. Peterson	Maint. Fee due 2/5/07
DOE S-91,736 S.N. 60/138,326 S.N. 09/615,640 US Pat. 6,451,742	Filed 06/09/99 Filed 7/13/00 Issued 9/17/02	High Temperature Superconducting Com-posite Conductor & Method for Manufac-turing the Same	T.G. Holesinger and J.F. Bingert	Maint. Fee due 9/17/05
DOE S-91,748 S.N. 60/143,781 S.N. 09/615,640 US Pat. 6,452,375	Filed 7/13/99 Filed 7/13/00 Issued 9/17/02	Apparatus for Measurement of Critical Current in Superconductive Tapes	J. Y. Coulter R.F. DePaula	Maint. Fee due 9/17/05
DOE S-91,761 S.N. 60/213,111 S.N. 09/867,842 US Pat. 6,383,989	Filed 6/21/00 Filed 5/29/01 Issued 5/7/01	Architecture for High Critical Current Superconducting Thick Films	Q.X. Jia S.R. Foltyn T.G. Holesinger	Maint. Fee due 11/7/05
DOE 94,732 S.N. 09/721,834 US Pat. 6,624,993	Filed 11/22/00 Issued 9/23/03	Adjustable Direct Current and Pulsed Fault Current Limiter	H.J. Boenig J.B. Schillig	Maint. Fee due 3/23/07
DOE S-97,723 S.N. 10/113,476 US Pat. 6,624,122	Filed 5/30/01 Issued 9/23/03	High Critical Current Superconducting Tapes	T G. Holesinger, Q.X. Jia S.R. Foltyn	Maint. Fee due 3/27/07
DOE S-97,804 S.N. 10/096,774 US Pat. 6,511,943	Filed 3/13/02 Issued 1/28/03	Synthesis of Magnesium Diboride by Magnesium Vapor Infiltration	A. Serquis, Y.T. Zhu, F.M. Mueller, D.E. Peterson, X.Z. Liao	Maint. Fee due
DOE 94,734 **S.N. 60/333,917** **S.N. 10/113,475** **US Pat. 6,716,545**	**Filed 11/21/01** **Filed 3/28/02** **Issued 4/6/04**	**High Temperature Superconducting Composite Conductors**	**T.G. Holesinger, S.R. Foltyn, P.N. Arendt, J.R. Groves, Q.X Jia, A. Ayala**	
DOE S-94,668 **S.N. 60/170,968** **S.N. 09/616,570** **US Pat. 6,730,410**	**Filed 7/14/00** **Issued 5/4/04**	**Surface control alloy substrates and methods of manufacture thereof**	**L.G. Fritzemeier, Q. Li, M.W. Rupich, E.D. Thompson, E.J. Siegel, C.L.H. Thieme, S. Annavarapu, P.N. Arendt,**	

Designation	Date	Subject	Issued to	Status
			S.R. Foltyn	
DOE S-97,725 **S.N. 10/113,476** **US Pat. 6,756,139**	**Filed 3/28/02** **Issued 6/29/04**	**Buffer Layer on Metal Alloy Substrates for Superconducting Tapes**	**Q.X. Jia, S.R. Foltyn, P.N. Arendt, J.R. Groves**	

4c. Licenses Granted

License Number	Dates	Subject	Issued to
89-41-0000-1	12/28/88 - 11/94	Apparatus for Characterizing Conductivity of Materials by Measuring the Effect of Induced Shielding Currents Therein	Lakeshore Cryotronics
99-C00510.1	11/11/98	Superconductive Article including Cerium Oxide Layer	DuPont Superconductivity
01-C01080.0	05/29/01 - - 12/17/03	High Temperature Superconductor Material	IGC-SuperPower, LLC
01-C01081.0	05/29/01 - - 12/17/03	High Temperature Superconductor Material	IGC-SuperPower, LLC
01-C01082.0	05/29/01 - - 12/17/03	Fault Current Limiter and Alternating Current Circuit Breaker Device	IGC-SuperPower, LLC

5. Agreements in Progress (8 Active, all types)

5a. Superconductivity Pilot Center Agreements – Active
None

5b. CRADA Agreements - Active

Organization	Topic	PI	Funding,$K DOE	Funding,$K Partner	Dates
Oxford Superconducting Technology	Bi-2212 HTS Tapes	Smith Holesinger Holesinger	290 55 700	290 100 730	11/93 -11/96 10/97–10/98 5/99-10/05
American Superconductor Corp.	**Bi-2223 Wire Development** **HTS Wire Technologies**	**Holesinger** **Holesinger**	**450** **375**	**450** **300**	**5/02-5/04** **5/04-5-05**
General Electric	**HTS Generator**	**Waynert** **Schmierer**	**860** **860**	**860** **860**	**8/02-8/04** **8/04-8/06**
DuPont	HGMS Magnetic Separation	Waynert	120 LANL 300 FI Dupont	200	6/02-6/04
Hyper Tech Research, Inc.	MgB$_2$ Wire Development	Mueller	400	400	9/02-9/04

| IGC-SuperPower | Coated Conductors | Foltyn Balachandran | 700, LANL 500, ANL | 1300 | 1/00-1/03 |
| | | Foltyn | 1700 | 1700 | 3/03-3/05 |

<u>5c. Funds In / Funds Out Agreements – Active</u>

Organization	Topic	PI	Type	Value $K	Dates
Long Electro-magnetics, Inc.	**AC Losses in HTS Wires**	**Willis**	**Funds In**	**30**	**2/04-11/04**
SCI Engineered Materials, Inc.	**Bi2212 Round Wires for High Field Magnets**	**Holesinger**	**Funds-In**	**100**	**10/04-10/06**

<u>5d. Other Collaborations - Active</u>

Organization	Topic	PI	Dates
ASC/ ANL/ ORNL/ U. Wisconsin/ (previously, NIST-Gaithersburg)	Bi-2223 Wire Development (Wire Development Group)	J. Willis Holesinger	11/91-11/00 11/00-
3M/ORNL/ Southwire / Stanford University	Coated Conductor Group	E. Peterson	3/97-
ASC/ ORNL/ LBNL/U. Wisconsin/ Stanford U./MIT/ Wright-Patterson AFB/ EPRI (previously, TCSUH)	Coated Conductor Development Group	J. Willis Holesinger	2/96- 11/00-
Oak Ridge National Laboratory	HTS Information Exchange	D. Peterson	In Progress
Argonne National Laboratory	HTS Information Exchange	D. Peterson	In Progress
Sandia National Laboratories	HTS Information Exchange	D. Peterson	In Progress
Brookhaven National Lab.	HTS Information Exchange	D. Peterson	In Progress

6. Completed Agreements

<u>6a. Superconductivity Pilot Center Agreements - Completed</u>

Organization	Topic	PI	Funding,$K DOE	Funding,$K Partner	Dates
CPS Superconductor	Metal-Ceramic Interfaces	Mitchell	102.6	80.8	9/89 - 9/90
DuPont / Hewlett-Packard	HTS Electronic Components	Peterson	3777	7200	10/89 - 10/92
Space Industries, Inc.	Microgravity Processing	Peterson	205	247	4/90 - 4/91
Cryopower Associates	Improvement of Bulk HTS Materials	Maley Maley	45.2 199.4	60 485.9	Ph 1: 2/90 Ph 2: 1/92 1/94
HiTc	Optimizing	Wu	136.6	125	Ph 1: 9/89

Superconco	Performance of HTS Cavities and Targets	Wu	101.9	100	Phase 2: 12/91
Ceracon, Inc	Bulk HTS Consolidation	Foltyn	237.5	300	Phase 1: 6/91
Nuclear Metals/ SNL/AT&T	HTS Co-extrusion	Wallace Bingert	239.2 239.2	760.5 285 NM 190 ATT	Ph 1: 8/90-8/93 Ph. 2: 10/93-10/96
The Boeing Company	Superconducting Electromagnetic Devices	Peterson	240	240	4/97 - 4/98
Power Superconduct-ing Devices, Inc	Development of HTS Fault Current Limiter	Peterson	250	250	7/96-7/98
American Superconductor Corporation	Bi-2223 Conductors HTS Composite Conductors	Peterson Peterson Willis Willis Willis Holesinger	170.5 587.1 1500 2300 1800	179 350 950 1100 1800	Ph 1: 6/89- Ph 2: 11/91- Ph 3: 2/94- Ph 4: 3/96- Ph.5: 7/98-3/01

6b. CRADA Agreements - Completed

Organization	Topic	PI	Funding,$K DOE	Funding,$K Partner	Dates
Lockheed Martin	Coil Development	Peterson	330	210	7/93 - 7/96
Plastronic, Inc.	Liquid Cryogen Free HTS Magnet System	Daugherty	100 +33k funds in	67	6/95 - 5/96
The BOC Group, Inc.	Superconducting Coated Materials	Peterson	70	70	2/23/96-11/22/96
EURUS Technologies, Inc.	Development of HTS Current Leads & Solders	Peterson	80	140	2/6/96-2/5/97
Eriez Magnetics	HTS Magnetic Separation	Daugherty	70	52	4/2/96-4/1/97
Lockheed Martin	HTS Current Limiter	Peterson	400	400	11/95-10/97
Lockheed Martin	Bridge-Type Fault Current Limiter	Boenig	700	1400	11/95-9/98
General Atomics (assumed LM activity)	Bridge-Type Fault Current Limiter	Peterson	Remainder of 700 from above	Remainder of 1400 from above	9/98-5/99, 5/99-11/99
Astronautics Corp. of America	Active HTS Magnetic Refrigerator	Peterson	200	200	4/98-7/00

ABB Power T&D Co., Inc.	HTS Transformer	Maley	95	70	7/99-7/00
3M Corporation	Coated Conductors	Peterson	960 720 400	1375 720 150	3/97-3/99 3/99-5/00 5/00-1/02

6c. Funds In / Funds Out Agreements - Completed

Organization	Topic	PI	Type	Value $K	Dates
Superconductor Technologies, Inc.	Rutherford Backscattering	Maggiore	Funds In	1.0	5/88 - 5/89
Public Service Co. of New Mexico	HTS Theory	Parkin	Funds In	357.1	6/88 - 6/90
EPRI	Assessments for Utilities	Newkirk	Funds In	99.8	6/88 - 6/89
AMP, Inc.	RF Characterization of Tl-Based HTS Films	Wallace	Funds In	102.9	1/89 - 5/89
EPRI	Heat Pipe Switch	Merrigan	Funds In	150	1/89 - 1/90
Univ. Missouri, Rolla	HTSC Fibers	Maestas	Funds Out	111	1/89 - 1/90
Bechtel	SMES Systems/ Hot-to-Cold Transitions	Maestas	Funds Out	10	2/89 - 2/90
Rocketdyne Corp., Rockwell, Intl.	Synthesis of Tl HTS	Peterson	Funds Out	95.3	5/89 - 5/90
EPRI	New Families of HTS	Smith	Funds In	120	2/90 - 2/92
Underground Systems	Transmission Systems	Stewart	Funds In	48	5/91 - 5/92
W.J. Schafer Assoc.	SMES Assessment	Peterson	Funds Out	89.9	5/92 - 5/93
Univ. Calif.-San Diego	Hydrocode Models	Peterson	Funds Out	63 57	12/92 -12/93 6/94 - 5/95
Intermagnetics General Corporation	Tl-Based HTS Coils	Peterson	Funds Out	400	10/92 - 10/96
MIT	Bitter Magnets	Peterson	Funds In	50	5/93 - 4/96
Midwest Super- conductivity, Inc.	IBAD-Coated Flexible Substrates	Peterson	SBI Tech Consulting Agreement	5	3/95 - 3/96
EPRI	Ac Loss	Maley	Funds In	150	9/5/95-

	Measurements in HTS Cables				9/4/96
EPRI	Thick Films on Flexible Substrates	Wu	Funds In	25 200	7/95-9/95 10/95-10/96
Pirelli Cable & Systems	Ac Losses on HTS Cables	Peterson Willis	Funds In	55 63	11/97 – 6/98 1/99 – 9/99
Columbia Univ.	HTS Susceptometer	Peterson	Funds In	237	7/02 - 4/03

6d. Other Collaborations - Completed

Organization	Topic	PI	Dates
Tektronix, Inc.	Cryogenic Materials Characterization	J. Smith	11/89-5/94